

**Spectroscopic and Kinetic Studies of Hydrodenitrogenation
and Hydrodesulfurization over Supported Nickel Phosphide
(Ni₂P)**

Travis Matthew Gott

Dissertation submitted to the faculty of Virginia Polytechnic Institute and State
University in partial fulfillment of the requirement for the degree of

Doctor of Philosophy
In
Chemical Engineering

S. Ted Oyama, Chariman

Luke Achenie

David F. Cox

Brian E. Hanson

November 4, 2008

Blacksburg, Virginia

Keywords: Nickel phosphide, HDN, HDS, pyridine, thiophene, FTIR, XAFS

Copyright 2008, Travis Matthew Gott

Spectroscopic and Kinetic Studies of Hydrodenitrogenation and Hydrodesulfurization over Supported Nickel Phosphide (Ni_2P)

By

Travis Matthew Gott

Chemical Engineering

Abstract

This dissertation describes preparation and characterization of Ni_2P catalysts and their application in hydrodesulfurization (HDS) and hydrodenitrogenation (HDN). The work carried out includes synthesis of Ni_2P on different siliceous supports, SiO_2 and MCM-41. It also includes characterization of these catalytic materials using X-ray diffraction (XRD), temperature-programmed reduction (TPR), Fourier transform infrared (FTIR) spectroscopy and X-ray absorbance fine structure (XAFS) spectroscopy. In situ FTIR was employed to study the acidity of $\text{Ni}_2\text{P}/\text{SiO}_2$ and probe the catalytic sites involved in the HDN of pyridine. Transient and steady-state kinetics of a surface intermediate that is formed upon pyridine adsorption and reaction was studied to elucidate the mechanism of HDN over $\text{Ni}_2\text{P}/\text{SiO}_2$. Additionally, in situ FTIR and X-ray absorption near edge structure (XANES) spectroscopy was utilized to probe the bonding, mechanism and kinetics of thiophene HDS over a novel MCM-41-supported Ni_2P catalyst. The use of these techniques allowed for better understanding of the surface intermediates, mechanisms and the nature of the active sites involved in HDN and HDS.

*To my parents for their
constant love and support*

Acknowledgments

“Therefore since we also have such a large cloud of witnesses surrounding us, let us lay aside every weight and the sin that so easily ensnares us, and run with endurance the race that lies before us, keeping our eyes on Jesus, the source and perfecter of our faith, who for the joy that lay before Him endured a cross and despised the shame, and has sat down at the right hand of God’s throne” Hebrews 12:1-2 [HCSB]

I would first like to give praise to my Lord Jesus Christ for His power, grace and mercy, without which I would be lost.

I am extremely grateful to my advisor and mentor Dr. S. Ted Oyama for his guidance and continued words of encouragement. Thank you for teaching me to work hard, overcome frustrations and for preparing me to think independently. I also greatly appreciate the advice and support of Dr. David Cox over the past five years. In addition, special thanks for the help of my other committee members Dr. Brian Hanson and Dr. Luke Achenie.

I greatly appreciate the friendships, both personally and professionally, of present and past group members. Thank you for providing advice and helping me to grow in this unique research environment: Haiyan Zhao, Jason Gaudet, Dmitri Iarikov, Dr. Yong-Kul Lee, Dr. Pelin Hacarlioglu, Dr. Hankwon Lim, Dr. Yunfeng Gu and Dr. Corey Reed. I would also like to thank the Chemical Engineering Department staff, Riley Chan, Chris Moore, Diane Cannaday, Mike Vaught and Tina Kirk for their continuous support and help.

I am extremely grateful to my brothers and sisters in Christ at Northstar Church in Blacksburg. Thank you for giving me the opportunity to find my ministry for God’s kingdom. Special thanks to my church family at Sullivan Baptist Church in Kingsport for their love, prayers and words of encouragement.

I can’t express enough my sincere love and gratitude to my parents for their love, prayers, guidance, encouragement and sacrifices during my studies. Thank you for always being Christ-centered examples to me. I would also like to thank my other family members for their love, prayers and encouragement.

Finally, special thanks to my lifelong friends that are like brothers from the University of Tennessee: Tom Peterson and Chris Welder. Thanks for always being there to talk, for your words of encouragement and to discuss the state of affairs that is UT Football. Go Vols!!! Special thanks to new friends from Virginia Tech: Will James and Jose Herrera. Thanks for being there to laugh, talk, play golf and argue about sports. I am confident that we unequivocally concluded that soccer is indeed boring.

Table of Contents

Chapter 1

Introduction

1.1.	Importance of Deep Hydrodesulfurization and Hydrodenitrogenation	1
1.2.	Hydrodesulfurization Challenges and Advances	2
1.3.	Novel Catalytic Materials and Alternative Sulfur Removal Processes	8
1.4.	Goals	12
1.5.	Dissertation Overview	13

Chapter 2

Transition Metal Phosphides

2.1.	General Properties	32
2.2.	Catalytic Properties in Hydrotreating	36
2.3.	Kinetic Pathways in HDS and Mechanism in HDN	45
2.4.	Bimetallic Systems	53
2.5.	Conclusions	57

Chapter 3

Kinetic Method for Studying Reactive Surface Intermediates: The Hydrodenitrogenation of Pyridine over Ni₂P/SiO₂

3.1.	Introduction	66
3.2.	Experimental	73
3.2.1.	Materials	73
3.2.2.	Catalyst Samples	73
3.2.3.	Characterization	74
3.2.4.	Spectroscopic and Kinetic Measurements	75
3.3.	Results and Discussion	84
3.3.1.	Characterization Results	84
3.3.2.	FTIR Spectral Interpretation	85
3.3.3.	FTIR Spectroscopy Measurements	90
3.3.4.	Steady-State Rate Measurements	102
3.4.	Conclusions	107

Chapter 4

In Situ FTIR and XANES Studies of Thiophene Hydrodesulfurization on Ni₂P/MCM-41

4.1.	Introduction	112
4.2.	Experimental	117
4.2.1.	Synthesis and Characterization	117
4.2.2.	In situ FTIR Measurements	119
4.2.3.	In situ XAS Measurements	121
4.2.4.	Activity Tests for Thiophene HDS	122
4.3.	Results and Discussion	124
4.3.1.	Catalyst Properties	124
4.3.2.	Infrared Measurements	131
4.3.3.	XANES Measurements	143
4.3.4.	Steady-State HDS Activity	149
4.4.	Conclusions	152
	Chapter 5 Conclusions	158

List of Tables

Table 1.1	Summary of recent advances in hydroprocessing with sulfides	6
Table 1.2	Summary of process improvements, new processes and catalyst developments	8
Table 2.1	Physical properties of metal-rich phosphides	33
Table 2.2	Characteristics of 12 wt% Ni ₂ P/SiO ₂ catalysts	37
Table 2.3	Comparison of rate constants for sulfides and phosphides	47
Table 2.4	Correlation between active sites and catalytic performance	56
Table 3.1	Pyridine weight times for gas-phase transient kinetic experiments	79
Table 3.2	Pyridine weight times for steady-state kinetic experiments	83
Table 3.3	Physical properties of Ni ₂ P/SiO ₂ catalysts	84
Table 3.4	Steady-state pyridine reaction results at 423 K	103
Table 4.1	Physical properties of Ni ₂ P/MCM-41	129
Table 4.2	Steady-state thiophene HDS results	150

List of Figures

Figure 2.1	Triangular prism and tetrakaidecahedral structures in phosphides	34
Figure 2.2	Crystal structures of metal rich phosphides	35
Figure 2.3	HDS activity vs. time at 613 K and 3.1 MPa	39
Figure 2.4	EXAFS spectra of fresh samples	40
Figure 2.5	EXAFS spectra of spent samples	42

Figure 2.6	a) In situ EXAFS cell b) EXAFS data at reaction conditions	44
Figure 2.7	Reaction network for 4,6-DMDBT desulfurization	46
Figure 2.8	In situ FTIR spectra of pyridine on Ni ₂ P and NiMo	49
Figure 2.9	Reaction network for 2-methylpiperidine HDN	51
Figure 2.10	Relative concentrations and selectivity in the HDN of 2-methylpiperidine	51
Figure 2.11	Scheme for the HDN of 2-methylpiperidine	52
Figure 2.12	Structure of Ni ₂ P showing P (left) and Ni(right) coordination	54
Figure 3.1	In situ FTIR reactor system	76
Figure 3.2	Three-phase trickle bed reactor system	82
Figure 3.3	Powder XRD pattern of Ni ₂ P/SiO ₂ catalyst sample	85
Figure 3.4	FTIR spectrum of 0.85 mol% pyridine in He flow adsorbed on Ni ₂ P/SiO ₂ at 423 K	87
Figure 3.5	FTIR spectrum of 0.85 mol% pyridine in H ₂ flow adsorbed on Ni ₂ P/SiO ₂ at 423 K	88
Figure 3.6	FTIR spectrum of 0.85 mol% piperidine in He flow adsorbed on Ni ₂ P/SiO ₂ at 423 K	90
Figure 3.7	FTIR spectra of pyridine adsorbed on SiO ₂ in He flow as a function of temperature	91
Figure 3.8	FTIR spectra of pyridine adsorbed on Ni ₂ P/SiO ₂ in He flow as a function of temperature	92
Figure 3.9	FTIR spectra of pyridine adsorbed on Ni ₂ P/SiO ₂ in H ₂ flow as a function of temperature	93
Figure 3.10	Time-resolved FTIR spectra of 0.85 mol% pyridine adsorbed on Ni ₂ P/SiO ₂	95
Figure 3.11	Example of transient kinetic analysis for pyridine adsorption on Ni ₂ P/SiO ₂	97
Figure 3.12	Transient additions of pyridine at several concentrations over	99

Ni₂P/SiO₂

Figure 3.13	Transient kinetic results for pyridine reaction on Ni ₂ P/SiO ₂ at 423 K	101
Figure 3.14	Steady-state kinetic results for pyridine reaction over Ni ₂ P/SiO ₂ at 423 K and atmospheric pressure	103
Figure 4.1	In situ FTIR reactor system	124
Figure 4.2	M/Z = 18 signal for TPR of the samples at $\beta = 2 \text{ K min}^{-1}$ ($.0333 \text{ K s}^{-1}$)	126
Figure 4.3	Changes in the Ni K-edge XANES region in the reduction of Ni ₂ P/MCM-41	127
Figure 4.4	Reduction of Ni ₂ P/MCM-41 followed by XANES	128
Figure 4.5	XRD patterns of supported Ni ₂ P catalysts	130
Figure 4.6	Low-angle XRD patterns of MCM-41 and Ni ₂ P/MCM-41	131
Figure 4.7	FTIR spectra of thiophene adsorbed on MCM-41 in thiophene/He Flow as a function of temperature	132
Figure 4.8	FTIR spectra of thiophene adsorbed on Ni ₂ P/MCM-41 in thiophene/He flow as a function of temperature (high wavenumber region)	133
Figure 4.9	FTIR spectra of thiophene adsorbed on Ni ₂ P/MCM-41 in thiophene/He flow as a function of temperature (low wavenumber region)	135
Figure 4.10	FTIR spectra of thiophene adsorbed on Ni ₂ P/MCM-41 after 300 s degassing in He flow as a function of temperature	136
Figure 4.11	FTIR spectra of thiophene adsorbed on Ni ₂ P/MCM-41 in thiophene/H ₂ flow as a function of temperature (high wavenumber region)	138
Figure 4.12	FTIR spectra of thiophene adsorbed on Ni ₂ P/MCM-41 in thiophene/H ₂ flow as a function of temperature (low wavenumber region)	139
Figure 4.13	FTIR spectra of thiophene adsorbed on Ni ₂ P/MCM-41 after 300 s degassing in H ₂ flow as a function of temperature	140

Figure 4.14	XANES measurements of the Ni ₂ P/MCM-41 sample exposed to thiophene/H ₂ (0.13 mol%)	144
Figure 4.15	Decline in absorbance at 8330.9 eV for thiophene adsorption	145
Figure 4.16	XANES measurements of adsorbed thiophene undergoing TPR in H ₂	148
Figure 4.17	Arrhenius plot for thiophene HDS over Ni ₂ P/MCM-41	151

List of Schemes

Scheme 1.1	Simplified reaction network for 4,6-DMDBT HDS	4
Scheme 1.2	Simplified sulfur-specific BDS of DBT	10
Scheme 1.3	Simplified network for ODS of DBT	11
Scheme 3.1	Simplified reaction pathway for pyridine HDN	68
Scheme 4.1	Simplified thiophene HDS reaction network	115
Scheme 4.2	Proposed thiophene bonding modes	116
Scheme 4.3	Simplified surface HDS mechanism showing adsorbed tetrahydrothiophene and deposited sulfur	142

List of Abbreviations

- BDS – biodesulfurization
- BET – Brunauer-Emmett-Teller
- BPy – Pyridine on Brønsted acid sites
- BT – benzothiophene
- CVD – chemical vapor deposition

- 2,3-DHT – 2,3-dihydrothiophene
- 2,5-DHT – 2,5-dihydrothiophene
- 3,3'-DMBP – 3,3'-dimethylbiphenyl
- 3,3'-DMBCH (DMBCH) – 3,3'-dimethylbicyclohexane
- 3,3'-DMCHB (MCHT) – 3,3-dimethylcyclohexylbenzene
(methylcyclohexyltoluene)
- 4,6-DMDBT – 4,6-dimethyldibenzothiophene
- 4H-DMDBT – 4,6-dimethyl-tetrahydrodibenzothiophene
- 6H-DMDBT – 4,6-dimethyl-hexahydrodibenzothiophene
- 12H-DMDBT – 4,6-dimethyl-dodecahydrodibenzothiophene
- DBT – dibenzothiophene
- DDS – direct desulfurization pathway
- E2 – bimolecular elimination
- EXAFS – extended X-ray absorption fine structure
- FTIR – Fourier transform infrared
- GC – gas chromatography
- HDN – hydrodenitrogenation
- HDS – hydrodesulfurization
- HPy – hydrogen-bonded pyridine
- HYD – hydrogenation pathway
- LPy – pyridine coordinated to Lewis acid sites
- MCM-41 – mesoporous catalytic material 41
- NTP – normal temperature and pressure

- ODS – oxidative desulfurization
- Pip - piperidine
- PPy – physisorbed pyridine
- Py – pyridine
- S_N2 – nucleophilic bimolecular substitution
- T – thiophene
- TOF – turnover frequency
- TPR – temperature-programmed reduction
- TKD – tetrakaidecahedral
- UAOD – ultrasound-assisted oxidative desulfurization
- UHP – ultrahigh purity
- UPC – ultrapure carrier
- USY – ultrastable Y-zeolite
- XANES – X-ray absorption near edge structure
- XRD – X-ray diffraction

Chapter 1

Introduction

1.1. Importance of Deep Hydrodesulfurization and Hydrodenitrogenation

Recently enacted regulations limiting the emissions of pollutants and the continuing decline in the quality of petroleum feedstocks have made sulfur and nitrogen removal one of the paramount problems in the refining industry. Concerning regulations, in 2006 the US sulfur contents in fuels were mandated to be 30 ppm (with an 80 ppm cap) in gasoline and 15 ppm in diesel [1], and similar levels were legislated in Europe and Japan [2,3,4]. In 2008, the standards effectively require diesel to reach 10 ppm S content and every blend of gasoline sold in the United States to meet the 30 ppm level [5]. Such levels correspond to the removal of +99.95 % of sulfur from a typical crude containing 1.5 % sulfur, and the removal process has been termed deep or ultra-deep hydrodesulfurization (HDS). These new requirements are exacerbated by the decreasing quality of petroleum crudes. There is a slow continuous trend for crudes becoming heavier (more dense) and containing higher amounts of sulfur. In addition, the removal of nitrogen compounds by hydrodenitrogenation (HDN) is key to deep HDS, as nitrogen-containing species adsorb strongly on sites that carry out HDS, and inhibit the reaction. It has been recognized that current hydrotreating catalysts are not adequate to meet the regulated levels, and this has given rise to widespread research efforts to develop a new generation of replacement materials. A reduction of sulfur from 500 ppm to 15 ppm

necessitates catalysts that are ~ 7 times more active than existing catalysts [1]. For these reasons a new generation of hydrotreating catalysts are needed. Several studies have shown that a new class of materials, transition metal phosphides, are highly active under conditions of deep HDS in the presence of nitrogen compounds and have the potential of being the next generation of hydrotreating catalysts [6].

1.2. Hydrodesulfurization Challenges and Advances

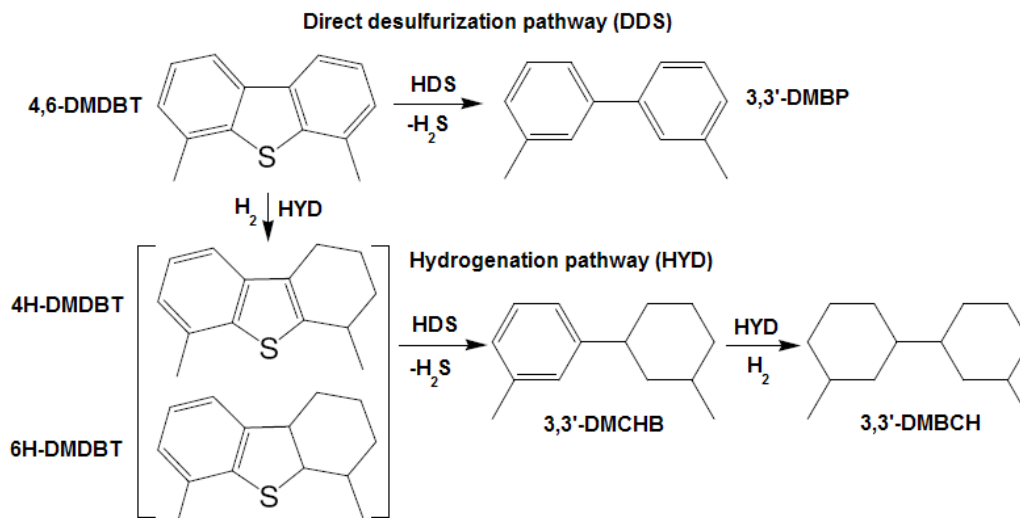
Commercial catalysts for HDS are sulfides based on Mo or W and promoted with Ni or Co. The subject has been covered in several treatises [7,8-24], and deep HDS in other reviews [25-28]. More recent coverage of deep desulfurization has been made in reviews by Song [1], Ho [29] and Babich and Moulijn [30] and has been a principal topic in recent conferences [31,32,33] and the subject of dedicated journal volumes [34-39].

The review by Song [1] comprehensively covers various process options for removal of sulfur including standard hydroprocessing, but also alternative and emerging processes such as catalytic distillation, reactive adsorption, polar molecule adsorption, selective adsorption, selective extraction, selective alkylation, membrane separation, and caustic extraction. In addition to these there is also biodesulfurization, oxidative desulfurization and ultrasound-assisted oxidative desulfurization [40]. These methods will be covered briefly.

Gas oil fractions are typically composed of several types of sulfur compounds encompassing thiols, sulfides, disulfides, thiophenes (T), benzothiophenes (BT), dibenzothiophenes (DBT) and their alkylated derivatives. Small sulfur compounds,

including thiols, sulfides and disulfides, exhibit higher HDS activities than that of thiophene by an order of magnitude because of higher electron densities on the sulfur atoms and weaker C-S bonds. The reactivities of the 1- to 3-ring sulfur compounds decrease in the order $T > BT > DBT$ [1]. Refractory sulfur compounds are alkylated DBTs with side chains in close proximity to the sulfur atom. The principal findings by Song [1] and Ho [29] are that HDS research has moved to the most refractory sulfur compounds. Earlier studies had already shown that for diesel these were the sterically hindered dibenzothiophenes, i.e., DBT's with alkyl substituents in the 4- and/or 6-positions [7,41-43] of which the 4,6-dimethyldibenzothiophene (4,6-DMDBT) molecule is archetypal.

As shown in Scheme 1.1, the HDS of 4,6-DMDBT proceeds through two reaction pathways. The first pathway is the direct desulfurization route (DDS) by direct hydrogenolysis of the C-S bonds without prior hydrogenation of either benzenic ring to yield 3,3'-dimethylbiphenyl (3,3'-DMBP). The second pathway is the hydrogenation route (HYD) in which 4,6-DMDBT is first hydrogenated to the intermediates 4,6-dimethyl-tetrahydro-DBT (4H-DMDBT) or 4,6-dimethyl-hexahydro-DBT (6H-DMDBT). The hydrogenated intermediate 6H-DMDBT is subsequently desulfurized to 3,3'-dimethylcyclohexylbenzene (3,3'-DMCHB) and 3,3'-dimethylbicyclohexane (3,3'-DMBCH) by further hydrogenation [18,24].



Scheme 1.1. Simplified reaction network for 4,6-DMDBT HDS

The compound 4,6-DMDBT has been found to be at least ten times less reactive than DBT itself [44,45]. These compounds are difficult to desulfurize because of the steric hindrance caused by the alkyl groups which block access to the sulfur atoms [41,43,45]. At conditions of deep HDS, sulfur removal from these substituted DBTs is necessary to achieve the low sulfur specifications of gas oil of 10 ppm, which because of their low reactivity pose the greatest difficulty. Previous studies have shown that HDS of unsubstituted DBT proceeds mainly through the DDS pathway whereas alkyl substituted DBTs are converted mainly via the HYD route. The introduction of alkyl substituents in the 4 and/or 6 positions leads to a diminution in the rate of the DDS pathway while that of the HYD pathway is relatively unaffected [24,46-48]. As a result, the HYD pathway for the HDS of sterically hindered sulfur compounds is dominant, and catalysts with good hydrogenation activity are the most promising.

The problem of sulfur removal is closely related to nitrogen removal because nitrogen compounds are strong inhibitors of HDS, especially at the high levels of

conversion required for deep HDS. The removal of nitrogen compounds from petroleum crudes occurs simultaneously with other catalytic hydrotreating processes. The nitrogen compounds present in petroleum are generally one of two types: heterocycles and nonheterocycles. The latter compounds are comprised of anilines, nitriles and aliphatic amines that denitrogenate rapidly [49,50]. Nitrogen heterocycles are composed of single- or multi-ring compounds containing a six-membered pyridinic ring (basic nitrogen compounds) or a five-membered pyrrolic ring (nonbasic). The nitrogen content in petroleum crudes is generally 5 to 20 times lower than the sulfur content. However, compared to sulfur heterocycles, nitrogen heterocycles are more difficult to hydroprocess and generally require higher temperatures, higher hydrogen pressures and lower space velocities [51]. However, if not removed, basic nitrogen compounds greatly inhibit HDS because of competitive adsorption on catalytic sites [52]. Thus, the ability to carry out efficient HDN is key to deep HDS as the reaction rate of sulfur removal is markedly affected by small amounts of basic nitrogen compounds in the range 0 – 50 ppm [53-55]. Several studies of the inhibiting effects of nitrogen compounds on the HDS of refractory sulfur compounds have shown that basic nitrogen heterocycles in particular inhibit the rate of HDS. The inhibition is most pronounced for the HYD pathway because of strong adsorption on hydrogenation sites [48,56]. Under conditions of deep HDS the amount of nitrogen compounds becomes dominant or comparable to refractory sulfur compounds and strongly competes in the heteroatom removal process. As a result, minimizing the inhibiting effect by efficient removal of nitrogen is vital to achieve low levels of sulfur.

Considerable research in the past three years has concentrated on finding more active sulfide catalysts to overcome present limitations. As summarized below, the

approaches taken have consisted in optimizing sulfide compositions, using new supports, exploring novel compounds, and improving processes (Table 1.1).

Table 1.1. Summary of recent advances in hydroprocessing with sulfides

Improvement of existing sulfides		
Review: Improving dispersion and morphology	+	Chiannelli et al. [57]
Sonochemical and CVD methods for high dispersion	+	Moon [58,59], Okamoto [60,61], Ramos [62]
Ultrasonic spray pyrolysis for high dispersion	+	Suslick [63]
Microwave method for high dispersion	+	Liu et al. [64,65,66]
Dispersing agents	+	Yoshimura [67], Okamoto [68], Escobar [69], Costa [70], Lélías [71], Rana [72,73]
Activation agents	+	Perot [74], Frizi [75]
Use of non-traditional elements	+	Fierro [76,77], Hubaut [78], Vít [79], Escalona [80], De Los Reyes [81], Giraldo [82], Centeno [83]
New precursors with Mo-S bonds	+	Ishihara [84], Ho [85], Bensch [86,87], Cruz-Reyes [88]
Urea-matrix combustion method	+	Green [89,90,91,92]
Use of unsupported trimetallic compositions	+	Fuentes [93], Alonso [94], Huirache-Acuña [95,96], Nava [97]
Alternative or improved supports for sulfides		
Improvement of Al ₂ O ₃ with Ti, and Ga	+	Segawa [98,99], Ramirez [100,101], Vrinat [102,103], Zhao [104]
Improvement of Al ₂ O ₃ with B	+	Okamoto [105,106,107], Shimada [108], Centeno [109]
Improvement of Al ₂ O ₃ with B and P	+	Ferdous [110]
F ⁻ or PO ₄ ³⁻ bind to Al ³⁺ ions and reduce interactions	-	Prins [111], Maity [112], Ding [113], Moon [114]
Basic additives (K, Li) are beneficial	+	Diehl [115], Fan [116], Mizutani [117]
Composite supports (SiO ₂ -Al ₂ O ₃)	+	van der Meer [118], Mochida [119], Kunisada [120], Ancheyta [121]
Composite supports (TiO ₂ -SiO ₂ , ZrO ₂ -Al ₂ O ₃)	+	Zhou, Zhang [122], Li [123]
Pure TiO ₂ supports for FeMo catalysts	+	Krалеva [124]
Hydroxyapatite modified by Zr and/or Al	+	Travert [125,126,127]
Carbon nanotubes, mesoporous clays	o	Chen [128], Chuan [129], Dalai

		[130], Shang [131], Song [132,133]
Mesoporous supports (MCM-41, SBA-15, Ti-HMS)	+	[134], [135], [136], [137], [138], [139], [140], [141], [142], [143], [144], [145], [146], [147], [148]
Theoretical studies		
Thiophene HDS mechanism	o	Ma [149], Yao [150], Paul [151], Topsøe [152,153], Nørskov [154],
Coordinatively unsaturated sites	o	Dumeignil [155], Paul [151], Aray [156], Wu [157]
General correlations of activity and electronic properties	o	Oviedo-Roa [158], Orita [159], Raybaud [160,161], Borges Jr. [162]
Support and surface structure, organonitrogen, H ₂ adsorption	o	Nelson [163-170]

+ Positive effect - Negative effect o Neutral or not applicable

A recent perspective on the improvement of sulfides has been given by Leliveld and Eijssbouts [171]. The commentary enumerates the economic, technical and environmental motivations for hydroprocessing catalyst development. Improvements of conventional metal sulfide catalysts and the discovery of novel materials and supports are needed to meet the increasing demand for energy. Enhancement of catalyst activity and stability is required to increase refinery throughput and to upgrade low value feedstocks to high value fuels. In addition, broad applicability of hydrotreating catalysts is desired to treat a wide range of feedstocks, as crudes are becoming more viscous and higher in sulfur, nitrogen and heavy metals contents. These improvements must result in a refinery end-product that meets the mandates of environmental legislation and the shift in the automotive industry to high efficiency, low emission engines requiring fuels with low levels of sulfur and aromatics. Achievement of these demands will require catalysts with higher volumetric activity for HDS, HDN and aromatics saturation with minimal hydrogen consumption. In order to treat a wide range of petroleum crudes, various

combinations of the staging of HDS and HDN catalysts must be developed to tailor the hydrotreating process to the characteristics of the feed. In addition, the ability to upgrade unconventional crudes extracted from tarsands and shale will require the development of stable, effective guard and demetallization catalysts for processing of heavier crudes.

1.3. Novel Catalytic Materials and Alternative Sulfur Removal Processes

Table 1.2. Summary of process improvements, new processes and catalyst developments

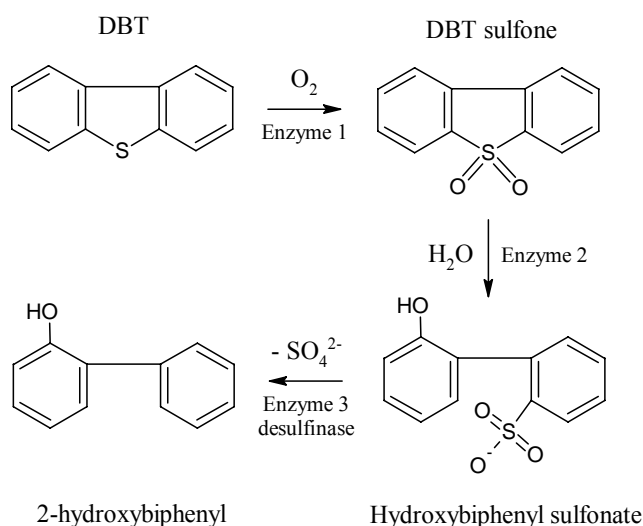
Industrial process and catalyst improvements		
Review: Recent developments in industry	o	Babich and Moulijn [30]
Inhibition of deep HDS by H ₂ S and NH ₃	-	[172],[173],[174], Vrinat [175], Farag [176], Nørskov [177], Rana [178,179], Perot [180], Song [181], Zeuthen [182], Ho [183]
Removal of H ₂ S and NH ₃ from intermediate stages	+	Adjaye [184], Nava [185], Mochida [186,187]
Biodesulfurization (BDS)	+	Liu [188], Towfighi [189], Kong [190], Xu [191], Huizhou [192], Mohebalı [193], Bassi [194], Li [195,196]
Oxidative desulfurization (ODS)	+	Wang [197], Song [198], Sampanthar [199], Corma [200], Lu [201], Green [202], Collins [203], García-Gutiérrez [204,205]
Ultrasound-assisted oxidative desulfurization (UAOD)	+	Doraiswamy [206], Yen [207,208,209], Zhao [210],
Nontraditional catalytic materials (carbides and nitrides)		
Carbides, nitrides	o	Rodriguez[211,212], Bussell [213], Djéga-Mariadassou [214,215], Al-Megren [216], Zhang [217]
Carbides, nitrides	o	Djega-Mariadassou [218], Nelson[219], Nagai [220,221], Dalai [222]
Review: Carbides and nitrides for hydroprocessing	o	Furimsky [223]

+ Positive effect - Negative effect o Neutral or not applicable

Several alternative processes for the removal of sulfur from petroleum crudes have been developed or are being developed. An insightful review of novel sulfur removal processes was recently given by Ito and van Veen [224]. For refractory molecules, the oxidative removal of sulfur from diesel by biodesulfurization, oxidative desulfurization and ultrasound-assisted oxidative desulfurization has been covered extensively in the literature (Table 1.2). Instead of reducing sulfur compounds to form H₂S, these methods oxidize the sulfur species to their corresponding sulfoxides (1-oxides) and sulfones (1,1-dioxides). Refractory sulfur compounds such as DBT and 4,6-DMDBT are only slightly more polar than hydrocarbons of similar structure. However, sulfoxides and sulfones are substantially more polar, thus permitting their selective removal by following the selective oxidation step with solvent extraction or solid adsorption. The development of oxidation methods for sulfur removal is aimed at providing efficient, cost effective, environmentally benign processes alternative to conventional hydroprocessing.

One option for the removal of sulfur is biocatalytic desulfurization, or biodesulfurization (BDS). Microorganisms require sulfur for growth and several bacteria can utilize the sulfur in thiophenic compounds and thus reduce the sulfur content in petroleum. BDS generally operates under ambient conditions of temperature and pressure and proceeds mainly through two biological pathways. These pathways include partial or complete degradation of the molecule with C-C bond cleavages or a sulfur-specific cleavage of only C-S bonds. The more selective sulfur-specific pathway is preferable to retain the value of fuels. Scheme 1.2 illustrates the simplified sulfur-specific enzymatic pathway for the BDS of DBT in the presence of oxygen and water to yield 2-hydroxybiphenyl as non-degradable end-product. Although many bacteria can

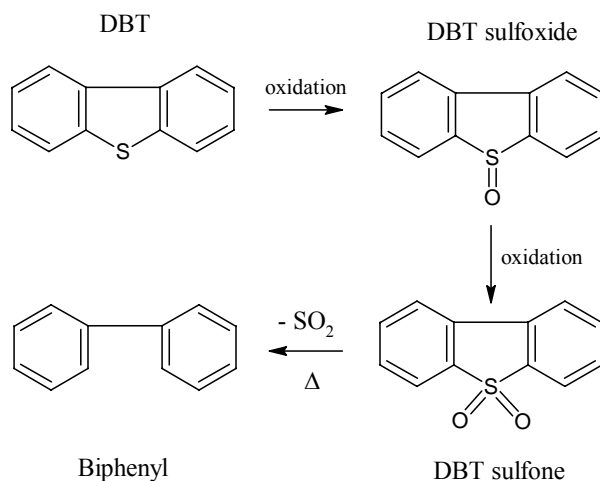
utilize sulfur through the sulfur-specific pathway, the stability and life-time of the biocatalysts are two major concerns. In addition, cooling of the petroleum feedstock to ambient temperature and subsequent removal of the biocatalyst from the treated feed is costly. Implementation of BDS as an industrial process would require microorganisms with higher sulfur removal activity, hydrocarbon phase tolerance, removal ability at high temperatures and longer stability [194].



Scheme 1.2. Simplified sulfur-specific BDS of DBT

The most promising alternative method for achieving deep HDS is sulfur removal via oxidative desulfurization (ODS). Analogous to BDS, the divalent sulfur atoms of thiophenic molecules are oxidized by the electrophilic addition of oxygen atoms to yield sulfones. The sulfones are subsequently removed in a second step by solid adsorption, selective extraction or distillation. Various studies on ODS have employed K_2FeO_4 [197], molecular oxygen [198], air [199], organic hydroperoxides [200], aqueous H_2O_2 [201-205] and many other reagents as oxidizers. However, oxidation of sulfur

compounds in the absence of catalysts is slow and several studies have utilized phase-transfer catalysts [197], metal salts [198,202], supported metal catalysts [199,204,205], metal-containing molecular sieves [200], activated carbon [201], metal-ligand activators [203], etc. to accelerate or facilitate the oxidation. Scheme 1.3 shows the simplified ODS scheme for DBT to DBT sulfone through the intermediate DBT sulfoxide. The ODS method offers several advantages over conventional hydroprocessing. The oxidation reactions can be carried out under mild conditions of temperature and pressure and do not require the expenditure of valuable hydrogen. However, the ODS process requires large amounts of oxidizing agent, separation and recovery of the catalysts, and low selectivity and activity towards the sulfur compounds. Both BDS and ODS require long reaction times and the second separation step in the processes leads to expensive waste management issues and oil yield losses of 10-20 % [225].



Scheme 1.3. Simplified network for ODS of DBT

Future employment of ODS processes will be dependent on the sulfur removal efficiency and capital investment required for implementation. The use of aqueous H_2O_2 – solid catalyst ODS is a low cost and environmentally benign option. However, such processes are typically impractical, requiring long reaction times and generally result in poor sulfur removal efficiency and excessive decomposition of the oxidant. In such biphasic oil-water systems, introduction of phase-transfer catalysts and ultrasonication in conjunction with ODS can be used to greatly increase the overall sulfur removal efficiency [206]. Ultrasound has a mechanical effect on the reaction system by promoting rapid mixing, accelerating dissolution and renewing the surface of the solid catalyst. Several studies have shown improvement in the ODS process upon ultrasound irradiation including + 99 % sulfur removal efficiency in shorter reaction times [207,209], complete recovery of solid catalysts [208] and minimal decomposition of H_2O_2 [207]. Although oxidative desulfurization processes are viable alternatives they require capital investment for new unit operations. As a result, discovery of novel catalysts and implementation into existing hydrotreating reactors is the most promising option for achieving deep HDS.

1.4. Goals

The primary goals of this research are to characterize highly active Ni_2P catalysts, evaluate their activities in HDS and HDN reactions and elucidate the mechanisms of HDS and HDN on their surfaces. In order to achieve these goals the following tasks have been carried out:

- Synthesis of Ni_2P on siliceous supports with different surface area

- Characterization of supported Ni₂P catalysts with CO chemisorption, BET surface area measurements and temperature-programmed reduction
- X-ray diffraction measurements to identify the structure of Ni₂P catalysts
- FTIR measurements to investigate the acidic properties of Ni₂P catalysts with pyridine as a probe molecule
- Transient kinetic measurements of pyridine HDN with in situ FTIR to determine the kinetic role of adsorbed surface intermediates
- Steady state kinetic measurements of pyridine HDN
- In situ FTIR measurements with thiophene as a probe molecule for supported Ni₂P to elucidate the bonding mode of thiophene on active centers
- In situ XANES measurements of thiophene adsorption and reaction on supported Ni₂P
- Transient kinetic measurements of thiophene HDS with in situ XANES to determine the kinetic role of adsorbed sulfur species

1.5. Dissertation Overview

Chapter 1 describes the importance and challenges of HDS and HDN, hydroprocessing background, objectives and dissertation overview.

Chapter 2 provides a review of the physical and catalytic properties of transition metal phosphides in hydrotreating reactions, the kinetic and mechanistic pathways in HDS and HDN and further motivation and background for this research.

Chapter 3 presents a novel kinetic method for elucidating the kinetic role of adsorbed surface intermediates in HDN. Combined transient and steady-state kinetic measurements are used to probe a pyridinium intermediate in the HDN of pyridine. In situ FTIR is used to monitor the transient behavior of the intermediate and measure the rate of reaction under non-steady-state conditions. Steady-state rate measurements are then used to compare the rates measurements.

Chapter 4 presents a study on thiophene HDS over Ni_2P supported on a high surface area siliceous support, MCM-41. The adsorption and reaction of thiophene is characterized by in situ FTIR and XANES analysis to determine the mode of adsorption. The catalytic activity of thiophene HDS over the supported Ni_2P catalyst is also investigated and a reaction scheme is proposed.

Chapter 5 presents the conclusion of this research.

References

- [1] C. Song, *Catal. Today*, 86 (2003) 211.
- [2] P. Greening, *Top. Catal.*, 16/17 (2001) 5.
- [3] Y. Yoshimura, M. Toba, H. Farag, K. Sakanishi, *Catal. Surv. Asia*, 8 (2004) 47.
- [4] T. Fujikawa, H. Kimura, K. Kiriya, K. Hagiwara, *Catal. Today*, 111 (2006) 188.
- [5] A. Zhou, X. Ma, C. Song, *J. Phys. Chem. B.*, 110 (2006) 4699.
- [6] S.T. Oyama, *J. Catal.* 216 (2003) 343.
- [7] M.L. Vrinat, *Appl. Catal.*, 6 (1983) 137.
- [8] H. Topsøe, B. S. Clausen and F. E. Massoth, *Hydrotreating Catalysis-Science and Technology*, Springer, Berlin, 1996.
- [9] A.N. Startsev, *Catal. Rev.-Sci. Eng.*, 37 (1995) 353.
- [10] Th. Weber, R. Prins, R. A. van Santen, Eds., *Transition Metal Sulfides, Chemistry and Catalysis*, Kluwer, Dordrecht, 1998.
- [11] S. Eijsbouts, *Appl. Catal. A: Gen.*, 158 (1997) 53.
- [12] *Stud. Surf. Sci. Catal.*, Vol. 127, *Hydrotreatment and Hydrocracking of Oil Fractions*, November 1999, pp. 1-458, Edited by B. Delmon, G.F. Froment and P. Grange.
- [13] M. Breyse, E. Furimsky, *Catal. Rev.-Sci. Eng.*, 44 (2002) 651.
- [14] D.Zuo, D. Li, H. Nie, Y. Shi, M. Lacroix, M. Vrinat, *J. Mol. Catal. A: Chem.*, 211 (2004) 179.
- [15] Y. Zhao, P. Kukula, R. Prins, *J. Catal.*, 221 (2004) 441.

-
- [16] A. Borgna, E.J.M. Hensen, J.A.R. van Veen, *J. Catal.*, 221 (2004) 541.
- [17] C. Dujardin, M.A. Lélías, J. van Gestel, A. Travert, J.C. Duchet, F. Maugé, *Appl. Catal. A: Gen.*, 322 (2007) 46.
- [18] R. Prins, M. Egorova, A. Röthlisberger, Y. Zhao, N. Sivasankar, *Catal. Today*, 111 (2006) 84.
- [19] E.J.M. Hensen, V.H.J. de Beer, J.A.R. van Veen, R.A. van Santen, *J. Catal.*, 215 (2003) 353.
- [20] L. Vradman, M.V. Landau, M. Herskowitz, *Fuel*, 82 (2003) 633.
- [21] Y.S. Al-Zeghayer, P. Sunderland, W. Al-Masry, F. Al-Mubaddel, A.A. Ibrahim, B.K. Bhartiya, B.Y. Jibril, *Appl. Catal. A: Gen.*, 282 (2005) 163.
- [22] H.R. Reinhoudt, R. Troost, A.D. van Langeveld, J.A.R. van Veen, S.T. Sie, J.A. Moulijn, *J. Catal.*, 203 (2001) 509.
- [23] D. Zuo, M. Vrinat, H. Nie, F. Maugé, Y. Shi, M. Lacroix, D. Li, *Catal. Today*, 93-95 (2004) 751.
- [24] M. Egorova, R. Prins, *J. Catal.*, 225 (2004) 417.
- [25] P.T. Vasudevan, J.L.G. Fierro, *Catal. Rev.-Sci. Eng.*, 38 (1996) 161.
- [26] T.G. Kaufmann, A. Kaldor, G.F. Stuntz, M.C. Kerby, L.L. Ansell, *Catal. Today*, 62 (2000) 77.
- [27] R. Shafi, G.J. Hutchings, *Catal. Today*, 59 (2000) 423.
- [28] M. Breyse, G. Djega-Mariadassou, S. Pessayre, C. Geantet, M. Vrinat, G. Pérot, M. Lemaire, *Catal. Today*, 84 (2003) 129.
- [29] T. C. Ho, *Catal. Today*, 98 (2004) 3.

-
- [30] I.V. Babich, J.A. Moulijn, *Fuel*, 82 (2003) 607.
- [31] Third International Symposium on Molecular Aspects of Catalysis by Sulfides, Monte Verità, Switzerland, May 23-27, 2004.
- [32] XIX Ibero American Catalysis Symposium, Merida, Mexico, September 6-9, 2004.
- [33] Fourth International Symposium on Molecular Aspects of Catalysis by Sulfides, Doorn, The Netherlands, May 13-17, 2007.
- [34] *Angewandte Chemie, International Edition*, Vol. 40, 2001, Hydrodesulfurization and Hydrodenitrogenation. Edited by Toshiaki Kabe, Atsushi Ishihara and Weihua Qian.
- [35] *Catal. Today*, Vol. 107-108, October 2005, pp. 1-956, Edited by José Manuel Domínguez and Jorge Ramírez.
- [36] *Catal. Today*, Vol. 109, Hydroprocessing of Heavy Oil Fractions, November 30, 2005, pp. 1-218, Edited by Jorge Ancheyta, Mohan S. Rana and Edward Furimsky.
- [37] *Catal. Today*, Vol. 104, Catalysis in Ultra-clean Fuels Production, June 15, 2005, pp. 1-100, Edited by Noritatsu Tsubaki, Uday T. Turaga and Chunshan Song.
- [38] *Catal. Today*, Vol. 98, International Symposium on Advances in Hydroprocessing of Oil Fractions (ISAHOF 2004), November 24, 2004, pp. 1-342, Edited by Jorge Ancheyta.

-
- [39] Catal. Today, Vol. 86, Effects of Support in Hydrotreating Catalysis for Ultra-clean Fuels, November 1, 2003, pp. 1-288, Edited by Yasuaki Okamoto, Michele Breyse, Gudimella Murali Dhar and Chunshan Song.
- [40] Update article, Desulfurization, the new-fashioned way, Chem. Eng. Prog., April 2006, pp. 12-13.
- [41] B.C. Gates, H. Topsøe, Polyhedron, 16 (1997) 3213.
- [42] D.R. Kilanowski, T. Teeuwen, V.H.J. de Beer, B.C. Gates, G.C.A. Schuit, H. Kwart, J. Catal., 55 (1978) 129.
- [43] X. Ma, K. Sakanishi, I. Mochida, Ind. Eng. Chem. Res., 33 (1994) 218.
- [44] M. Houalla, D.H. Broderick, A.V. Sapre, N.K. Nag, V.H.J. de Beer, B.C. Gates, H. Kwart, J. Catal., 21 (1980) 5237.
- [45] X. Ma, K. Sakanishi, I. Mochida, Ind. Eng. Chem. Res., 33 (1994) 218.
- [46] M. Macaud, A. Milenkovic, E. Schulz, M. Lemaire, M. Vrinat, J. Catal. 193 (2000) 255.
- [47] M. Egorova, R. Prins, J. Catal. 221 (2004) 11.
- [48] M. Egorova, R. Prins, J. Catal. 224 (2004) 278.
- [49] M. Machida, Y. Sakao, S. Ono, Appl. Catal., A 201 (2000) 115.
- [50] J. van Gestel, C. Dujardin, F. Maugé, J.C. Duchet, J. Catal. 202 (2001) 78.
- [51] J.R. Katzer, R. Sivasubramanian, Catal. Rev. – Sci. Eng. 20:2 (1979) 155.
- [52] P. Grange, Catal. Rev. – Sci. Eng. 21:1 (1980) 135.
- [53] F. van Looij, P. van der Laan, W.H.J. Stork, D.J. DiCamillo, J. Swain, Appl. Catal., A 170 (1998)

-
- [54] S. Shin, H. Yang, K. Sakanishi, I. Mochida, D.A. Grudoski, J.H. Shinn, *Appl. Catal., A* 205 (2001) 101.
- [55] G.C. Laredo, E. Altamirano, J.A. De los Reyes, *Appl. Catal., A* 243 (2003) 207.
- [56] M. Egorova, R. Prins, *J. Catal.* 241 (2006) 162.
- [57] R.R. Chiannelli, M.H. Siadati, M.P. de la Rosa, *Catal. Rev.-Sci. Eng.*, 48 (2006) 1.
- [58] J.J. Lee, H. Kim, J.H. Koh, A. Jo, S.H. Moon, *Appl. Catal. B: Env.*, 61 (2005) 274.
- [59] H. Kim, J.J. Lee, J.H. Koh, S.H. Moon, *Appl. Catal. B: Env.*, 54 (2004) 33.
- [60] Usman, T. Yamamoto, T. Kubota, Y. Okamoto, *Appl. Catal. A: Gen.*, 328 (2007) 219.
- [61] Y. Okamoto, *Catal. Today*, 132 (2008) 9.
- [62] R.R. Ramos, C. Bolivar, J. Castillo, J. Hung, C.E. Scott, *Catal. Today*, 133-135 (2008) 277.
- [63] S. E. Skrabalak, K. S. Suslick, *J. Am. Chem. Soc.*, 127 (2005) 9990.
- [64] X. Liu, L. Zhang, Y. Shi, H. Nie, X. Long, *Cuihua Xuebao*, 25 (2004) 748.
- [65] B. Liu, X. Xha, S. Sheng, W. Yang, G. Xiong, *Cuihua Xuebao*, 25 (2004) 770.
- [66] B. Liu, X. Zha, Q. Meng, H. Hou, S. Gao, J. Zhang, S. Sheng, W. Yang, *Cuihua Xuebao*, 26 (2005) 458.
- [67] M. Toba, Y. Miki, Y. Kanda, T. Matsui, M. Harada, Y. Yoshimura, *Catal. Today*, 104 (2005) 64.

-
- [68] T. Fujikawa, M. Kato, T. Ebihara, K. Hagiwara, T. Kubota, Y. Okamoto, J. Japan Petrol. Inst., 48 (2005) 114.
- [69] J. Escobar, M.C. Barrera, J.A. de los Reyes, J.A. Toledo, V. Santes, J.A. Colín, J. Mol. Catal. A: Chem., 287 (2008) 33.
- [70] V. Costa, K. Marchand, M. Digne, C. Geantet, Catal. Today, 130 (2008) 69.
- [71] M.A. Lérias, J. van Gestel, F. Maugé, J.A.R. van Veen, Catal. Today, 130 (2008) 109.
- [72] M.S. Rana, J. Ramírez, A. Gutiérrez-Alejandre, J. Ancheyta, L. Cedeño, S.K. Maity, J. Catal., 246 (2007) 100.
- [73] M.S. Rana, E.M.R. Capitaine, C. Leyva, J. Ancheyta, Fuel, 86 (2007) 1254.
- [74] S. Texier, G. Berhault, G. Pérot, F. Diehl, Appl. Catal. A: Gen., 293 (2005) 105.
- [75] N. Frizi, P. Blanchard, E. Payen, P. Baranek, C. Lancelot, M. Rebeilleau, C. Dupuy, J.P. Dath, Catal. Today, 130 (2008) 32.
- [76] N. Escalona, J. Ojeda, P. Baeza, R. Garcia, J.M. Palacios, J.L.G. Fierro, A. Agudo Lopez, F.J. Gil-Llambías, Appl. Catal. A: Gen., 287 (2005) 47.
- [77] J. Ojeda, N. Escalona, J.L.G. Fierro, A. Agudo Lopez, F.J. Gil-Llambías, Appl. Catal. A: Gen., 281 (2005) 25.
- [78] R. Hubaut, Appl. Catal. A: Gen., 322 (2007) 121.
- [79] Z. Vít, Appl. Catal. A: Gen., 322 (2007) 142.
- [80] N. Escalona, M. Vrinat, D. Laurenti, F.J. Gil-Llambías, Appl. Catal. A: Gen., 322 (2007) 113.
- [81] J.A. De Los Reyes, Appl. Catal. A: Gen., 322 (2007) 106.

-
- [82] S.A. Giraldo, M.H. Pinzón, A. Centeno, *Catal. Today*, 133-135 (2008) 239.
- [83] V.G. Baldovino-Medrano, S.A. Giraldo, A. Centeno, *Fuel*, 87 (2008) 1917.
- [84] A. Ishihara, H. Mochizuki, J. Lee, E.W. Qian, T. Kabe, Y. Tatsumi, K. Umehara, *J. Japan Petrol. Inst.*, 48 (2005) 137.
- [85] T.C. Ho, *Catal. Today*, 130 (2008) 206.
- [86] M. Poisot, W. Bensch, S. Fuentes, G. Alonso, *Thermochim. Acta*, 444 (2006) 35.
- [87] M. Poisot, W. Bensch, *Thermochim. Acta*, 453 (2007) 42.
- [88] R. Romero-Rivera, M. Del Valle, G. Alonso, E. Flores, F. Castellón, S. Fuentes, J. Cruz-Reyes, *Catal. Today*, 130 (2008) 354.
- [89] S.L. González-Cortés, T.-C. Xiao, T.-W. Lin, M.L.H. Green, *Appl. Catal. A: Gen.*, 302 (2006) 264.
- [90] S.L. González-Cortés, T.-C. Xiao, P.M.F.J. Costa, B. Fontal, M.L.H. Green, *Appl. Catal. A: Gen.*, 270 (2004) 209.
- [91] S.L. González-Cortés, T.-C. Xiao, S.M.A. Rodulfo-Baechler, M.L.H. Green, *J. Mol. Catal. A: Chem.*, 240 (2005) 214.
- [92] S.L. González-Cortés, S.M.A. Rodulfo-Baechler, T. Xiao, M.L.H. Green, *Catal. Lett.*, 111 (2006) 57.
- [93] A. Olivas, R. Verduzco, G. Alonso, S. Fuentes, *Preprints, ACS Div. Petr. Chem.*, 50 (2005) 372.
- [94] H. Nava, F. Pedraza, G. Alonso, *Catal. Lett.*, 99 (2005) 65.

-
- [95] R. Huirache-Acuña, M.A. Albiter, J. Espino, C. Ornelas, G. Alonso-Nuñez, F. Paraguay-Delgado, J.L. Rico, R. Martínez-Sánchez, *Appl. Catal. A: Gen.*, 304 (2006) 124.
- [96] R. Huirache-Acuña, M.A. Albiter, C. Ornelas, F. Paraguay-Delgado, R. Martínez-Sánchez, G. Alonso-Nuñez, *Appl. Catal. A: Gen.*, 308 (2006) 134.
- [97] H. Nava, J. Espino, G. Berhault, G. Alonso-Nuñez, *Appl. Catal. A: Gen.*, 302 (2006) 177.
- [98] Y. Saih, M. Nagata, T. Funamoto, Y. Masuyama, K. Segawa, *Appl. Catal. A: Gen.*, 295 (2005) 11.
- [99] K. Segawa, T. Funamoto, M. Watanabe, *Preprints, ACS Div. Petr. Chem.*, 50 (2005) 454.
- [100] P. Rayo, J. Ancheyta, J. Ramirez, *Catal. Today*, 98 (2004) 171.
- [101] J. Ramirez, G. Macias, L. Cedeno, A. Gutierrez-Alejandre, R. Cuevas, P. Castillo, *Catal. Today*, 98 (2004) 19.
- [102] E. Altamirano, J.A. de los Reyes, F. Murrieta, M. Vrinat, *J. Catal.*, 235 (2005) 403.
- [103] E. Altamirano, J.A. de los Reyes, F. Murrieta, M. Vrinat, *Catal. Today*, 133-135 (2008) 292.
- [104] W. Huang, A. Duan, Z. Zhao, G. Wan, G. Jiang, T. Dou, K.H. Chung, J. Liu, *Catal. Today*, 131 (2008) 314.
- [105] U. Usman, M. Takaki, T. Kubota, Y. Okamoto, *Appl. Catal. A: Gen.*, 286 (2005) 148.

-
- [106] U. Usman, T. Kubota, Y. Araki, K. Ishida, Y. Okamoto, *J. Catal.*, 227 (2004) 523.
- [107] Usman, T. Kubota, I. Hiromitsu, Y. Okamoto, *J. Catal.*, 247 (2007) 78.
- [108] F. Dumeignil, K. Sato, M. Imamura, N. Matsubayashi, E. Payen, H. Shimada, *Appl. Catal. A: Gen.*, 315 (2006) 18.
- [109] S.A. Giraldo, A. Centeno, *Catal. Today*, 133-135 (2008) 255.
- [110] D. Ferdous, A. K. Dalai, J. Adjaye, L. Kotlyar, *Appl. Catal. A: Gen.*, 294 (2005) 80.
- [111] M. Sun, D. Nicosia, R. Prins, *Catal. Today*, 86 (2003) 173.
- [112] S.K. Maity, G.A. Flores, J. Ancheyta, M.S. Rana, *Catal. Today*, 130 (2008) 374.
- [113] L. Ding, Z. Zhang, Y. Zheng, Z. Ring, J. Chen, *Appl. Catal. A: Gen.*, 301 (2006) 241.
- [114] H. Kim, J.J. Lee, S.H. Moon, *Appl. Catal. B: Env.*, 44 (2003) 287.
- [115] D. Mey, S. Brunet, C. Canaff, F. Mauge, C. Bouchy, F. Diehl, *J. Catal.*, 227 (2004) 436.
- [116] Y. Fan, J. Lu, G. Shi, H. Liu, X. Bao, *Catal. Today*, 125 (2007) 220.
- [117] H. Mizutani, H. Godo, T. Ohsaki, Y. Kato, T. Fujikawa, Y. Saih, T. Funamoto, K. Segawa, *Appl. Catal. A: Gen.*, 295 (2005) 193.
- [118] Y. van der Meer, E.J.M. Hensen, J.A.R. van Veen, A.M. van der Kraan, *J. Catal.*, 228 (2004) 433.
- [119] N. Kunisada, K.-H. Choi, Y. Korai, I. Mochida, K. Nakano, *Appl. Catal. A: Gen.*, 279 (2005) 235.

-
- [120] N. Kunisada, K.-H. Choi, Y. Korai, I. Mochida, K. Nakano, *Appl. Catal. A: Gen.*, 273 (2004) 287.
- [121] C. Leyva, M.S. Rana, J. Ancheyta, *Catal. Today*, 130 (2008) 345.
- [122] Y. Zhou, Z. Zhang, *Preprints, ACS Div. Petr. Chem.*, 50 (2005) 449.
- [123] G. Li, W. Li, M. Zhang, K. Tao, *Appl. Catal. A: Gen.*, 273 (2004) 233.
- [124] E. Kraveva, D. Paneva, A. Spojakina, I. Mitov, L. Petrov, *Reac. Kin. Catal. Lett.*, 85 (2005) 283.
- [125] M. A. Chaoui, A. El Ouassouli, A. Ezzamarty, M. Lakhdar, C. Moreau, J. Leglise and A. Travert, *J. Physique: Proc.*, 123 (2005) 319, (REMCES IX, Proceedings of the 9th International Seminar on the Physical Chemistry of Solid State Materials, 2002).
- [126] N. El Azarifi, A. El Ouassouli, M. Lakhdar, A. Ezzamarty, C. Moreau, A. Travert and J. Leglise, *J. Physique: Proc.*, 123 (2005) 203, (REMCES IX, Proceedings of the 9th International Seminar on the Physical Chemistry of Solid State Materials, 2002).
- [127] N. Elazarifi, M.A. Chaoui, A. El Ouassouli, A. Ezzamarty, A. Travert, J. Leglise, L.-C. de Ménorval, C. Moreau, *Catal. Today*, 98 (2004) 161.
- [128] H. Chen, X. Zhou, H. Shang, C. Liu, J. Qiu, F. Wei, *J. Nat. Gas Chem.*, 13 (2004) 209.
- [129] L. Chuan, S. Bin, C. Min, S. Hong-yan, Q. Guo-he, *J. Fuel Chem. Technol.*, 35 (2007) 407.

-
- [130] I. Eswaramoorthi, V. Sundaramurthy, N. Das, A.K. Dalai, J. Adjaye, *Appl. Catal. A: Gen.*, 339 (2008) 187.
- [131] H. Shang, C. Liu, Y. Xu, J. Qiu, F. Wei, *Fuel Process. Technol.*, 88 (2007) 117.
- [132] K.A. Carrado, C. Song, J.H. Kim, N. Castagnola, R. Fernandez-Saavedra, C.L. Marshall, M.M. Schwartz, *Prepr. ACS Div. Fuel Chem.*, 50 (2005) 344.
- [133] K.A. Carrado, J.H. Kim, C.S. Song, N. Castagnola, C.L. Marshall, M.M. Schwartz, *Catal. Today*, 116 (2006) 478.
- [134] J.M. Herrera, J. Reyes, P. Roquero, T. Klimova, *Micropor. Mesopor. Mat.*, 83 (2005) 283.
- [135] R. Silva-Rodrigo, C. Calderon-Salas, J.A. Melo-Banda, J.M. Dominguez, A. Vazquez-Rodriguez, *Catal. Today*, 98 (2004) 123.
- [136] X. Li, A. Wang, S. Zhang, Y. Chen, Y. Hu, *Appl. Catal. A: Gen.*, 316 (2007) 134.
- [137] E. Rodríguez-Castellón, A. Jiménez-López, D. Eliche-Quesada, *Fuel*, 87 (2008) 1195.
- [138] G.M. Dhar, G.M. Kumaran, M. Kumar, K.S. Rawat, L.D. Sharma, R.D. Raju, K.S.R. Rao, *Catal. Today*, 99 (2005) 309.
- [139] R. Nava, R.A. Ortega, G. Alonso, C. Ornelas, B. Pawelec, J.L.G. Fierro, *Catal. Today*, 127 (2007) 70.
- [140] S. Garg, K. Soni, G.M. Kumaran, M. Kumar, J.K. Gupta, L.D. Sharma, G.M. Dhar, *Catal. Today*, 130 (2008) 302.
- [141] O.Y. Gutiérrez, D. Valencia, G.A. Fuentes, T. Klimova, *J. Catal.*, 249 (2007) 140.

-
- [142] T. Klimova, J. Reyes, O. Gutiérrez, L. Lizama, *Appl. Catal. A: Gen.*, 335 (2008) 159.
- [143] T.A. Zepeda, J.L.G. Fierro, B. Pawelec, R. Nava, T. Klimova, G.A. Fuentes, T. Halachev, *Chem. Mater.*, 17 (2005) 4062.
- [144] S. Zeng, J. Blanchard, M. Breysse, Y. Shi, X. Su, H. Nie, D. Li, *Appl. Catal. A: Gen.*, 298 (2006) 88.
- [145] T.A. Zepeda, B. Pawelec, J.L.G. Fierro, A. Olivas, S. Fuentes, T. Halachev, *Microporous Mesoporous Mater.*, 111 (2008) 157.
- [146] A. Montesinos-Castellanos, T.A. Zepeda, *Microporous Mesoporous Mater.*, 113 (2008) 146.
- [147] B. Pawelec, J.L.G. Fierro, A. Montesinos, T.A. Zepeda, *Appl. Catal. B: Env.*, 80 (2007) 1.
- [148] T.A. Zepeda, B. Pawelec, J.L.G. Fierro, T. Halachev, *Appl. Catal. B: Env.*, 71 (2007) 223.
- [149] X. Ma, H.H. Schobert, *J. Mol. Catal. A: Chem.*, 160 (2000) 409.
- [150] X.-Q. Yao, Y.-W. Li, H. Jiao, *Theochem.*, 726 (2005) 81.
- [151] J.-F. Paul, S. Cristol, E. Payen, *Catal. Today*, 130 (2008) 139.
- [152] H. Topsøe, B. Hinnemann, J.K. Nørskov, J.V. Lauritsen, F. Besenbacher, P.L. Hansen, G. Hytoft, R.G. Egeberg, K.G. Knudsen, *Catal. Today*, 107-108 (2005) 12.

-
- [153] F. Besenbacher, M. Brorson, B.S. Clausen, S. Helveg, B. Hinnemann, J. Kibsgaard, J.V. Lauritsen, P.G. Moses, J.K. Nørskov, H. Topsøe, *Catal. Today*, 130 (2008) 86.
- [154] P.G. Moses, B. Hinnemann, H. Topsøe, J.K. Nørskov, *J. Catal.*, 248 (2007) 188.
- [155] F. Dumeignil, J.-F. Paul, E. Veilly, E. W. Qian, A. Ishihara, E. Payen, T. Kabe, *Appl. Catal. A: Gen.*, 289 (2005) 51.
- [156] Y. Aray, J. Rodríguez, A.B. Vidal, S. Coll, *J. Mol. Catal. A: Chem.*, 271 (2007) 105.
- [157] G. Wu, K. Fan, B. Delmon, Y.-W. Li, *J. Mol. Catal. A: Chem.*, 247 (2006) 189.
- [158] R. Oviedo-Roa, J.M. Martínez-Magadan, F. Illas, *J. Phys. Chem. B*, 110 (2006) 7951.
- [159] H. Orita, K. Uchida, N. Itoh, *Appl. Catal. A: Gen.*, 258 (2004) 115.
- [160] A.D. Gandubert, E. Krebs, C. Legens, D. Costa, D. Guillaume, P. Raybaud, *Catal. Today*, 130 (2008) 149.
- [161] P. Raybaud, *Appl. Catal. A: Gen.*, 322 (2007) 76.
- [162] I. Borges Jr., A.M. Silva, A.P. Aguiar, L.E.P. Borges, J.C.A. Santos, M.H.C. Dias, *J. Mol. Struct.: THEOCHEM*, 822 (2007) 80.
- [163] M. Sun, A.E. Nelson, J. Adjaye, *J. Phys. Chem. B*, 110 (2006) 2310.
- [164] M. Sun, A.E. Nelson, J. Adjaye, *Catal. Today*, 109 (2005) 59.
- [165] M. Sun, A.E. Nelson, J. Adjaye, *Catal. Today*, 105 (2005) 36.
- [166] M. Sun, A.E. Nelson, J. Adjaye, *J. Catal.*, 233 (2005) 411.
- [167] M. Sun, A.E. Nelson, J. Adjaye, *J. Catal.*, 231 (2005) 223.

-
- [168] M. Sun, A.E. Nelson, J. Adjaye, *J. Molec. Catal. A: Chem.*, 222 (2004) 243.
- [169] M. Sun, A.E. Nelson, J. Adjaye, *J. Catal.*, 226 (2004) 41.
- [170] M. Sun, A.E. Nelson, J. Adjaye, *J. Catal.*, 226 (2004) 32.
- [171] R.J. Leliveld, S.E. Eijsbouts, *Catal. Today*, 130 (2008) 183.
- [172] H. Nakamura, M. Amemiya, K. Ishida, *J. Japan Petr. Inst.*, 48 (2005) 281.
- [173] Q. Wang, H. Nie, X. Long, *Cuihua Xuebao*, 26 (2005) 399.
- [174] J. Chen, Z. Ring, *Fuel*, 83 (2004) 305.
- [175] N. Guernalec, T. Cseri, P. Raybaud, C. Geantet, M. Vrinat, *Catal. Today*, 98 (2004) 61.
- [176] H. Farag, *Appl. Catal. A: Gen.*, 331 (2007) 51.
- [177] A. Logadóttir, P.G. Moses, B. Hinnemann, N.-Y. Topsøe, K.G. Knudsen, H. Topsøe, J.K. Nørskov, *Catal. Today*, 111 (2006) 44.
- [178] M.S. Rana, R. Navarro, J. Leglise, *Catal. Today*, 98 (2004) 67.
- [179] M.S. Rana, J. Ancheyta, P. Rayo, S.K. Maity, *Fuel*, 86 (2007) 1263.
- [180] V. Rabarihoela-Rakotovao, S. Brunet, G. Perot, F. Diehl, *Appl. Catal. A: Gen.*, 306 (2006) 34.
- [181] U.T. Turaga, X. Ma, C. Song, *Catal. Today*, 86 (2003) 265.
- [182] P. Zeuthen, K.G. Knudsen, D.D. Whitehurst, *Catal. Today*, 65 (2001) 307.
- [183] T.C. Ho, *J. Catal.*, 219 (2003) 442.
- [184] A. Owusu-Boakye, A.K. Dalai, D. Ferdous, J. Adjaye, *Energy Fuels*, 19 (2005) 1763.
- [185] J. A. Nava, K.R. Ojeda, *Chem. Eng. Res. Des.*, 82 (2004) 208.

-
- [186] K.-H. Choi, N. Kunisada, Y. Korai, I. Mochida, K. Nakano, *Catal. Today*, 86 (2003) 277.
- [187] S.D.S. Murti, H. Yang, K.-H. Choi, Y. Korai, I. Mochida, *Appl. Catal. A: Gen.*, 252 (2003) 331.
- [188] G. Shan, H. Zhang, J. Xing, G. Chen, W. Li, H. Liu, *Biochem. Eng. J.*, 27 (2006) 305.
- [189] M. Rashtchi, G.H. Mohebal, M.M. Akbarnejad, J. Towfighi, B. Rasekh, A. Keytash, *Biochem. Eng. J.*, 29 (2006) 169.
- [190] Y. Hou, Y. Kong, J. Yang, J. Zhang, D. Shi, W. Xin, *Fuel*, 84 (2005) 1975.
- [191] F. Li, Z. Zhang, J. Feng, X. Cai, P. Xu, *J. Biotechnol.*, 127 (2007) 222.
- [192] S. Guobin, Z. Huaiying, X. Jianmin, C. Guo, L. Wangliang, L. Huizhou, *Biochem. Eng. J.*, 27 (2006) 305.
- [193] G. Mohebal, A.S. Ball, B. Rasekh, A. Kaytash, *Enzyme Microb. Technol.*, 40 (2007) 578.
- [194] M. Soleimani, A. Bassi, A. Margaritis, *Biotech. Adv.*, 25 (2007) 570.
- [195] H. Chen, W.-J. Zhang, J.-M. Chen, Y.-B. Cai, W. Li, *Bioresour. Technol.*, 99 (2008) 3630.
- [196] H. Chen, W.-J. Zhang, Y.-B. Cai, Y. Zhang, W. Li, *Bioresour. Technol.*, 99 (2008) 6928.
- [197] S. Liu, B. Wang, B. Cui, L. Sun, *Fuel*, 87 (2008) 422.
- [198] X. Ma, A. Zhou, C. Song, *Catal. Today*, 123 (2007) 276.

-
- [199] J.T. Sampanthar, H. Xiao, J. Dou, T.Y. Nah, X. Rong, W.P. Kwan, *Appl. Catal. B: Env.*, 63 (2006) 85.
- [200] A. Chica, A. Corma, M.E. Dómine, *J. Catal.*, 242 (2006) 299.
- [201] G. Yu, S. Lu, H. Chen, Z. Zhu, *Carbon*, 43 (2005) 2285.
- [202] F. Al-Shahrani, T. Xiao, S.A. Llewellyn, S. Barri, Z. Jiang, H. Shi, G. Martinie, M.L.H. Green, *Appl. Catal. B: Env.*, 73 (2007) 311.
- [203] S. Mondal, Y. Hangun-Balkir, L. Alexandrova, D. Link, B. Howard, P. Zandhuis, A. Cugini, C.P. Horwitz, T.J. Collins, *Catal. Today*, 116 (2006) 554.
- [204] J.L. García-Gutiérrez, G.A. Fuentes, M.E. Hernández-Terán, F. Murrieta, J. Navarrete, F. Jiménez-Cruz, *Appl. Catal. A: Gen.*, 305 (2006) 15.
- [205] J.L. García-Gutiérrez, G.A. Fuentes, M.E. Hernández-Terán, P. García, F. Murrieta-Guevara, F. Jiménez-Cruz, *Appl. Catal. A: Gen.*, 334 (2008) 366.
- [206] L.H. Thompson, L.K. Doraiswamy, *Ind. Eng. Chem. Res.*, 38 (1999) 1215.
- [207] H. Mei, B.W. Mei, T.-F. Yen, *Fuel*, 82 (2003) 405.
- [208] M.-W. Wan, T.-F. Yen, *Appl. Catal. A: Gen.*, 319 (2007) 237.
- [209] O. Etemadi, T.-F. Yen, *Energy Fuels*, 21 (2007) 2250.
- [210] D. Zhao, H. Ren, J. Wang, Y. Yang, Y. Zhao, *Energy Fuels*, 21 (2007) 2543.
- [211] P. Liu, J.A. Rodriguez, J.T. Muckerman, *J. Molec. Catal. A: Chem.*, 239 (2005) 116.
- [212] P. Liu, J.A. Rodriguez, J.T. Muckerman, *J. Phys. Chem.*, 108 (2004) 18796.
- [213] B. Diaz, S.J. Sawhill, D.H. Bale, R. Main, D.C. Phillips, S. Korlann, R. Self, M.E. Bussell, *Catal. Today*, 86 (2003) 191.

-
- [214] A. Szymańska-Kolasa, M. Lewandowski, C. Sayag, D. Brodzki, G. Djéga-Mariadassou, *Catal. Today*, 119 (2007) 35.
- [215] A. Szymańska-Kolasa, M. Lewandowski, C. Sayag, G. Djéga-Mariadassou, *Catal. Today*, 119 (2007) 7.
- [216] H.A. Al-Megren, S.L. González-Cortés, T. Xiao, M.L.H. Green, *Appl. Catal. A: Gen.*, 329 (2007) 36.
- [217] X.-H. Wang, M.-H. Zhang, W. Li, K.-Y. Tao, *Catal. Today*, 131 (2008) 111.
- [218] S. Suppan, J. Trawczynski, J. Kaczmarczyk, G. Djéga-Mariadassou, A. Hynaux, C. Sayag, *Appl. Catal. A: Gen.*, 280 (2005) 209.
- [219] W.A. Abdallah, A.E. Nelson, *Surf. Sci.*, 585 (2005) 113.
- [220] M. Nagai, *Appl. Catal. A: Gen.*, 322 (2007) 178.
- [221] H. Tominaga, T. Arahata, M. Nagai, *Chem. Eng. Sci.*, (2008) In Press.
- [222] V. Sundaramurthy, A.K. Dalai, J. Adjaye, *Appl. Catal. A: Gen.*, 335 (2008) 204.
- [223] E. Furimsky, *Appl. Catal. A: Gen.*, 240 (2003) 1.
- [224] E. Ito, J.A.R. van Veen, *Catal. Today*, 116 (2006) 446.
- [225] L.F. Ramírez-Verduzco, E. Torres-García, R. Gómez-Quintana, V. González-Peña, F. Murrieta-Guevara, *Catal. Today*, 98 (2004) 289.

Chapter 2

Transition Metal Phosphides

2.1. General Properties

Phosphorus reacts with most elements of the periodic table to form a diverse class of compounds known as phosphides. The bonding in these materials ranges from ionic for the alkali and alkaline earth metals, metallic or covalent for the transition elements, and covalent for the main group elements. The focus of this review concerns the metal-rich compounds, MP or M_2P , of the transition metals, which have metallic properties. The phosphorus-rich compositions are semiconducting and are considerably less stable than the metal-rich compounds.

The nature, structure and synthesis of phosphides have been described in a number of reviews [1,2,3]. Basically, the metal-rich phosphides have physical properties similar to those of ordinary metallic compounds like the carbides, nitrides, borides and silicides. They combine the properties of metals and ceramics, and thus are good conductors of heat and electricity, are hard and strong, and have high thermal and chemical stability (Table 2.1) [4].

Table 2.1. Physical properties of metal-rich phosphides

Ceramic Properties		Metallic Properties	
Melting point K	1100 – 1800	Electrical resistivity $\mu\Omega$ cm	900 – 25,000
Microhardness kg/mm^{-2}	600 – 1100	Magnetic susceptibility 10^6 emu/mol	110 – 620
-Heat of formation kJ mol^{-1}	30 – 180	Heat capacity J/mol K	20 – 50

Although the physical and chemical properties of phosphides resemble those of carbides and nitrides, they differ substantially in their crystal structure. In the carbides and nitrides, the carbon and nitrogen atoms reside in the interstitial spaces between metal host atoms to form relatively simple lattices. For the phosphides, however, the atomic radius of phosphorus (0.109 nm) is substantially larger than that of carbon (0.071 nm) or nitrogen (0.065 nm) and P does not fit into the ordinary octahedral holes formed by closed-packed metal atoms. For this reason in phosphides (also borides, sulfides, and silicides) the metal atoms form triangular prisms (Figure 2.1) where the metal atoms (dark atoms) surround the nonmetal atom (light atoms) [1]. For metal-rich compositions the number of nearest-neighbors increases to form a 9-fold tetrakaidecahedral (TKD) coordination with additional metal atoms placed near the centers of the vertical faces of the prism (Figure 2.1).

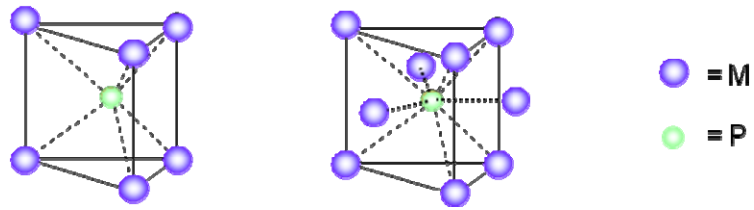


Figure 2.1. Triangular prism and tetrakaidecahedral structures in phosphides

Different arrangements of these building blocks give rise to different structures. A summary is given in Figure 2.2 [5].

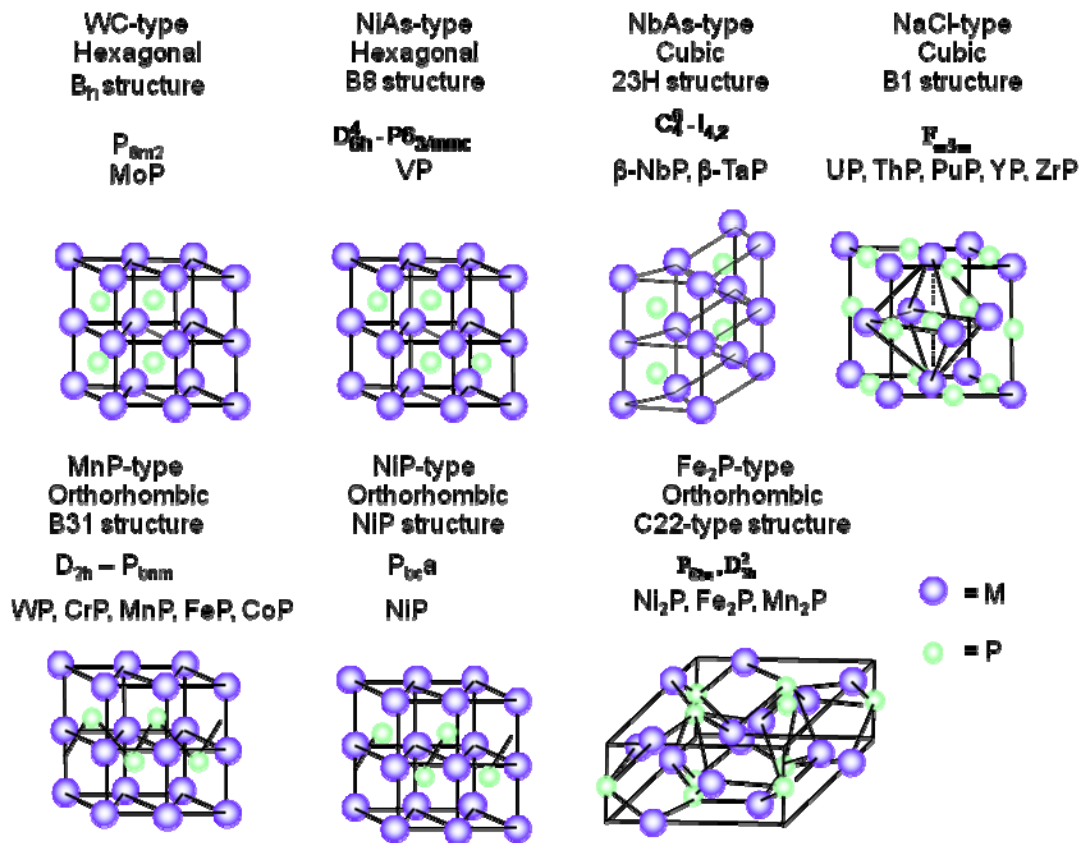


Figure 2.2. Crystal structures of metal rich phosphides

The monophosphide MoP is isostructural with WC, with the nonmetal-containing prisms stacked on top of each other. The monophosphide VP has the Ni-As structure with the P-prisms displaced laterally one-half a lattice spacing. The monophosphides NbP and TaP adopt the closely related NbAs structure, which just differs from VP in the way the prisms are stacked. The monophosphides of groups 6-10 adopt the MnP and NiP structures which have distorted NiAs structures where the phosphorus atoms form chains (MnP) or pairs (NiP). Importantly, the phosphides, unlike the sulfides, do not form layered structures, and so potentially permit greater access to active corner and edge sites on the crystallite surfaces. The globular morphology of

MoP [6] and Ni₂P [7] has been nicely demonstrated by electron microscopy by the group of Bussell. Phosphides are different from phosphorus-promoted sulfide catalysts, as reviewed by Iwamoto and Grimblot [8].

2.2 Catalytic Properties in Hydrotreating

The first catalytic studies of phosphides were by the group of Nozaki [9,10] in the 70's and 80's which examined their hydrogenation properties. This was followed 15 years later by a report on HDN by Robinson, et al. [11], but the supported materials in that study are likely to have been sulfides. Transition metal phosphides have also been applied to hydrodehalogenation reactions by Chen, et al. [12,13,14]. A first study on simultaneous HDS and HDN showed that MoP could be easily synthesized by temperature-programmed reduction (TPR) of a metal phosphate precursor [15], and this has been confirmed for other transition metal phosphides by the groups of Prins [16,17], Bussell [6,7,18,19,20], and Li [21,22,23]. The synthesis method is simple, and requires only moderate temperatures (773-873 K) and uses inexpensive precursors, compared to direct phosphidation with PH₃ [24,25]. Several recent studies have investigated novel synthesis methods for unsupported and supported transition metal phosphides. These include metal thiophosphates [26] and amorphous alloys [27] as precursors, citric acid modified precursors [28,29], polymer surfactant assisted synthesis [30], solvothermal synthesis methods [31,32], solution-phase arrested precipitation [33] and novel reducing agents [34]. These methods were aimed at producing monodispersed, high surface area unsupported phosphides and improving the dispersion of supported phosphides.

In previous work it has been shown that MoP, and WP have moderate activity and Ni₂P has excellent activity in hydroprocessing [35,36,37]. The overall activity was found to be in the order: Fe₂P < CoP < MoP < WP < Ni₂P in the simultaneous HDS of dibenzothiophene (3000 ppm S) and HDN of quinoline (2000 ppm N) at 643 K and 3.1 MPa, with the comparison based on equal sites (240 μmol CO/O₂ for phosphides/sulfides) loaded in the reactor [35,38]. Subsequent studies employed advanced techniques such as extended X-ray absorption fine structure (EXAFS) [39], x-ray absorption near-edge spectroscopy (XANES) [40] and nuclear magnetic resonance (NMR) [41] to characterize the catalysts. Tests were also carried out with a real feed that confirmed their high activity [42].

Early work on supported Ni₂P catalysts had utilized a low surface area silica (90 m²g⁻¹). The use of high surface area silicas provided an opportunity to investigate the effect of particle size, and interesting results were obtained [43]. Samples of low, medium, and high surface area were denoted as L, M, and H, and x-ray diffraction (XRD) line-broadening and chemisorption analysis duly showed that crystallite size (D_c) decreased with support area (Table 2.2).

Table 2.2. Characteristics of 12 wt% Ni₂P/SiO₂ catalysts

Sample	Ni ₂ P/SiO ₂ -L	Ni ₂ P/SiO ₂ -M	Ni ₂ P/SiO ₂ -H
Support area / m ² g ⁻¹	102	201	333
CO uptake ^a / μmol g ⁻¹	59	99	125
CO uptake ^b / μmol g ⁻¹	40	72	103
D _c / nm	10.1	7.8	6.5

^a Before reaction ^b After reaction

Hydrotreating activities of the samples were obtained in a three-phase, packed-bed reactor operated at realistic conditions of 3.1 MPa and 573-643 K with a model feed liquid.

Figure 2.3 illustrates the time course of HDS activities for the various Ni₂P/SiO₂ catalysts. The initial 4,6-DMDBT conversions were uniformly high for all the samples but they declined greatly for the Ni₂P/SiO₂-L, slightly for the Ni₂P/SiO₂-M, and actually grew for the Ni₂P/SiO₂-H. The H catalyst gave a high conversion (99+%) even after 100 h of reaction, the M catalyst gave an intermediate conversion (94%), and the L catalyst gave the lowest conversion (76%). The feed had 500 ppm S as 4,6-DMDBT, 3000 ppm S as dimethyl disulfide, 200 ppm N as quinoline, 1 wt% tetralin, 0.5 wt% n-octane (internal standard), and n-tridecane (solvent). The high activity of the high surface area Ni₂P catalysts at these conditions indicates that they are effective even in the presence of nitrogen compounds and aromatics, which are usually inhibiting of HDS in sulfides.

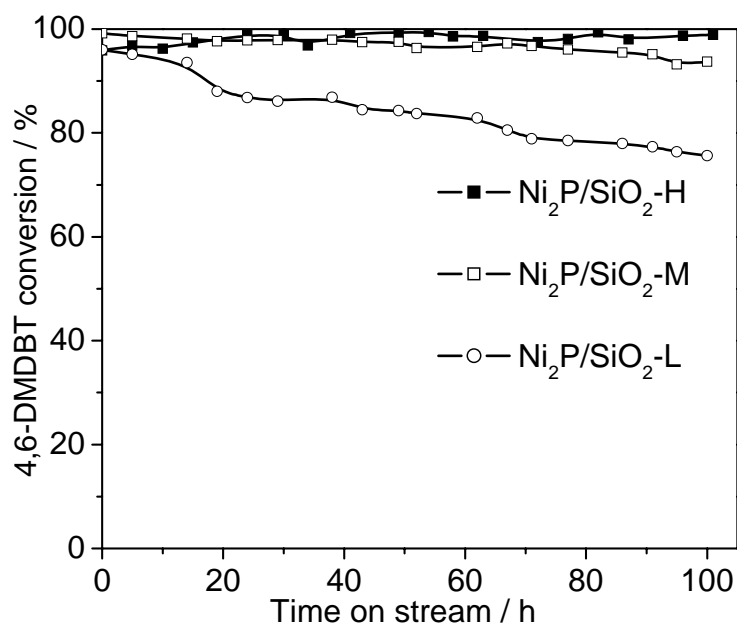
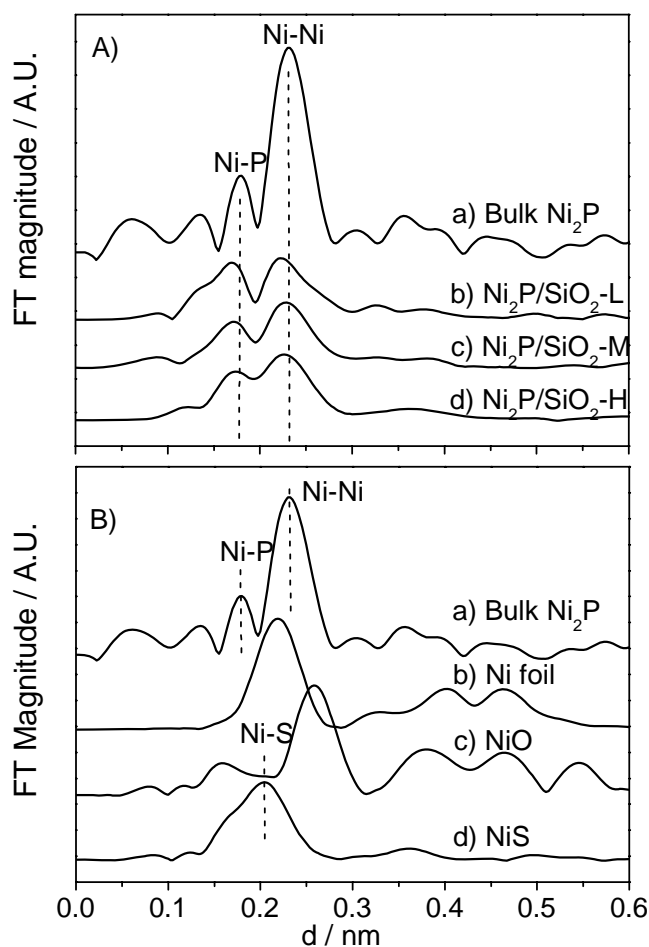


Figure 2.3. HDS activity vs. time at 613 K and 3.1 MPa

(Based on 240 μ mol of CO sites loaded in reactor)

The samples were characterized by extended x-ray absorption fine structure spectroscopy (EXAFS). Figure 2.4 A shows the Fourier-transformed Ni K-edge EXAFS spectra of the fresh silica-supported phosphide samples and Figure 2.4 B shows the spectra of reference standards. The bulk Ni₂P sample has two main peaks at 0.18 nm and 0.23 nm which correspond to Ni-P and Ni-Ni distances (Figure 2.4 B a)). The catalysts all display two distinct peaks at distances close to those of the Ni₂P standard, indicating that the predominant phase in these catalysts is Ni₂P, confirming XRD results. There is no indication of the presence of Ni metal (Fig. 2.4 B b)), Ni oxide (Fig. 2.4 B c)) or Ni sulfide (Fig. 2.4 B d)).



**Figure 2.4. EXAFS spectra of fresh samples
(Room temp., controlled atmosphere cells)**

Elemental analysis shows that the high surface catalyst (H) retains more phosphorus than the medium (M) or low area (L) catalysts (Ni/P ratio = 1/0.81 vs 1/0.62 and 1/0.48). This is confirmed by line-shape analysis which show Ni-P coordination (average number of bonds) to be in the order $H > M > L$. The smaller crystallites appear to have stronger Ni-P bonding allowing them to retain more phosphorus, and this accounts for their stability and activity. This is also seen in the lower loss of chemisorption sites during the course of hydrotreating (Table 2.2).

The finding that smaller Ni₂P crystallites have higher activity and stability than larger crystallites is significant, as it suggests using low loadings for making better catalysts. These results were confirmed by Montesinos-Castellanos, et al. in the HDS of DBT at 553 K and 3.4 MPa over MoP/Al₂O₃ prepared with different Mo loadings. Phosphides prepared with lower metal loading exhibited higher HDS activity whereas higher loadings resulted in sintering of MoP particles during reduction and lower activities [44]. Lower loadings are beneficial for practical cost reasons. The EXAFS results indicate that the origin of the reactivity difference resides in the electronic structure, as is found in many metallic systems [45,46,47]. This is reflected in the different Ni-P bond strengths and also the different selectivity for products obtained from 4,6-DMDBT (hydrogenation versus direct desulfurization).

Considerable work has been done to understand the state of the working Ni₂P-H catalyst. This was done by extensive analysis of the catalyst after reaction [48,49,50] and during reaction [51,52]. The results of EXAFS analysis of spent Ni₂P/SiO₂ samples of different loading [48] are shown in Figure 2.5.

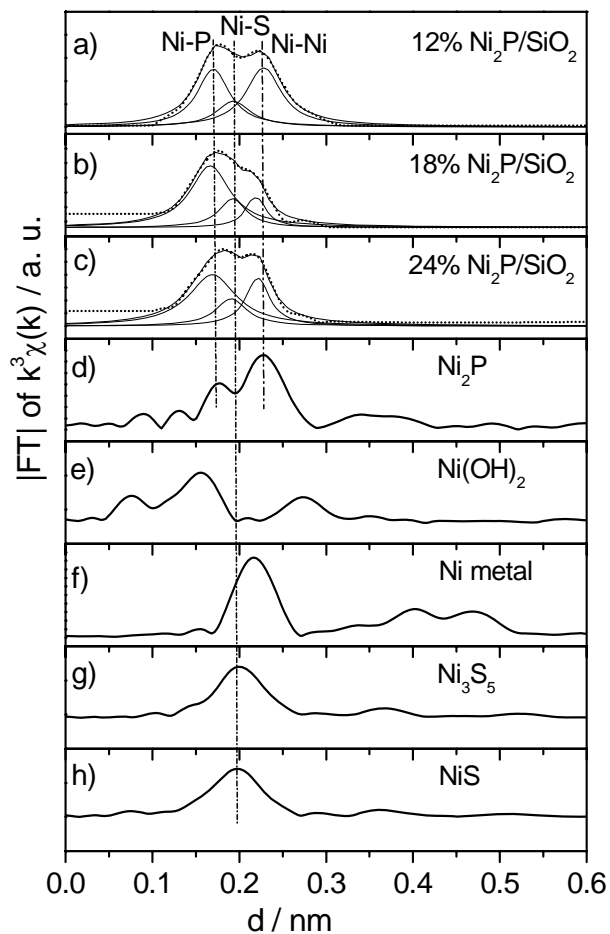


**Figure 2.5. EXAFS spectra of spent samples
(Room temp., controlled atmosphere cells)**

The Fourier transforms of the spent samples (Figure 2.5 a-c) show roughly the two peak pattern of the fresh samples except that the peaks are broadened and the Ni-Ni distances are less intense, indicating the presence of a new phase. The results were compared with some reference compounds (Figure 2.5 d-h) to identify the phase. The decrease in the intensity of the Ni-Ni peak was accompanied by a shift to lower distance, while the Ni-P peak itself remained strong.

The spectral changes were due to development of intensity in the Ni-S distance region. Even though no distinct Ni-S peak is seen, a feature in that region would give rise to the broad signal actually observed. Figure 2.5 a-c) shows a fit to three Lorentzian line shapes. The middle peak of each triad fits the position of the Ni-S distance in the sulfide reference compounds (Figure 2.5 g,h). The spectra of phosphorus deficient compounds like Ni_{12}P_5 do not fit the observed pattern [48].

Thus, the EXAFS data strongly suggest that in the catalysts some Ni-Ni bonds are disrupted to form Ni-S linkages. However, the surface is not a pure sulfide, as the reactivity of nickel sulfide is known to be poor [53]. It was deduced that the active phase was a phosphosulfide in the outer region of a Ni_2P crystallite core. This work was the first to suggest the nature of the active phosphide catalyst. Recent calculations by the group of Nelson [54] confirm the stability of the phosphosulfide overlayer.

Although the post-reaction analysis of the samples gave valuable information about the catalyst, in situ studies were undertaken by Asakura and coworkers to investigate its working state [51,52]. EXAFS has been applied to the investigation of hydrotreating catalysts, but little work has been previously done on structural analysis in the liquid-phase, especially at elevated temperature and pressure [55]. This is because of the strong absorption of x-rays by liquids, and because of the severe stresses on the window material at realistic reaction conditions. Yet, the use of liquid-phase conditions for HDS is important, as it is well known that gas-phase conditions do not reproduce the results that are obtained with liquids [56,57].

A key development for the work was the construction of a low-volume cell with flat windows transparent to x-rays that were chemically, structurally, and thermally stable (Figure 2.6) [51,52]. Previous cells could not handle both high temperatures (> 600 K) and pressures ($>$

20 bar) for liquids [58,59,60]. The window was made of cubic boron nitride, an x-ray transparent material superior to beryllium or diamond, because it does not oxidize at high temperatures, and does not give x-ray diffraction peaks.

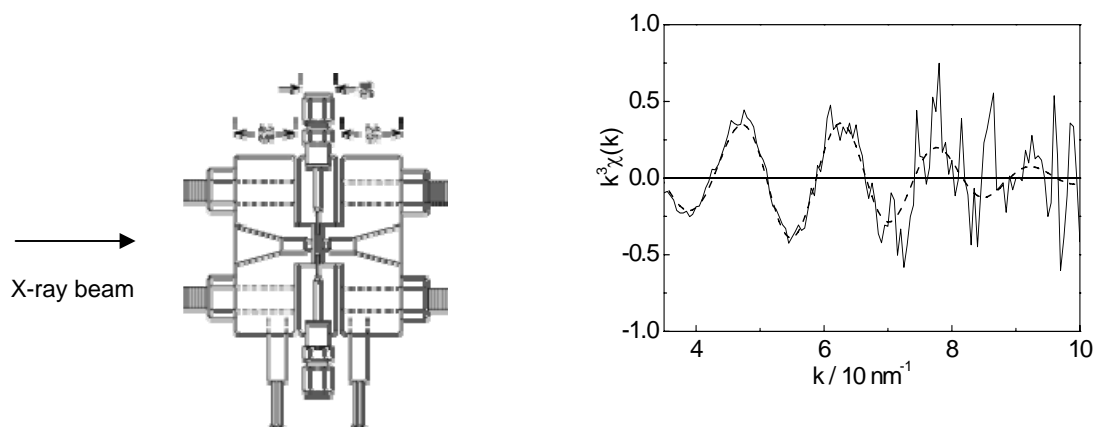


Figure 2.6. a) In situ EXAFS cell (lengths in mm) b) EXAFS data at reaction conditions (613 K, 3 MPa, 3% DBT in tetradecane)

A measurement at reaction conditions of 12 wt% $\text{Ni}_2\text{P}/\text{SiO}_2\text{-H}$ was carried out, and after subtraction of the Ni_2P contribution a single oscillation was isolated (Figure 2.6 b, dotted line). Curve fitting simulations assuming different bonds such as Ni-P, Ni-S, Ni-C, and Ni-Ni were carried out, and the calculated curve for a Ni-S bond gave a good fit as shown by the dotted curve. The calculated distance of 0.228 ± 0.004 nm is longer than the Ni-P bond of 0.221-224 nm found in phosphides like Ni_2P , NiP, Ni_8P_3 , NiP_2 [61,62], but is in the range of 0.225-0.240 nm found in Ni-S bonds in sulfides like NiS [63], NiS_2 [64], and Ni_3S_2 [65]. Therefore, the newly found bond corresponds to a Ni-S bond, which is formed during the reaction, and is consistent with the earlier suggested surface phosphosulfide.

Aside from the silica supported catalysts, various other supports were tested for the phosphides, including carbon [66,67], alumina [50,68], MCM-41 [69,70,71], SBA-15 [72,73], and USY zeolites [74]. It was found that carbon, MCM-41, SBA-15 and USY zeolites were particularly effective supports.

2.3. Kinetic Pathways in HDS and Mechanism in HDN

For deep HDS, new catalysts with higher hydrogenation activity are required, and to evaluate these and to design new deep HDS processes, kinetic data for each reaction pathway of 4,6-dimethyldibenzothiophene (4,6-DMDBT) HDS are important. Considerable work was carried out to understand the reaction steps involved in the HDS of this compound by Song and coworkers [75]. The reaction network for dibenzothiophene (DBT) has been studied extensively on sulfides, and an identical network has been suggested for 4,6-DMDBT (Figure 2.7) [76,77]. Two main pathways are suggested to dominate: a) a direct desulfurization route (DDS) and b) a hydrogenation route (HYD) (Figure 2.3.1). Evidence for these pathways is discussed in several comprehensive articles [78-83]. There is also an isomerization route where the methyl rings migrate, but this is likely to operate only with acidic supports [84,85].

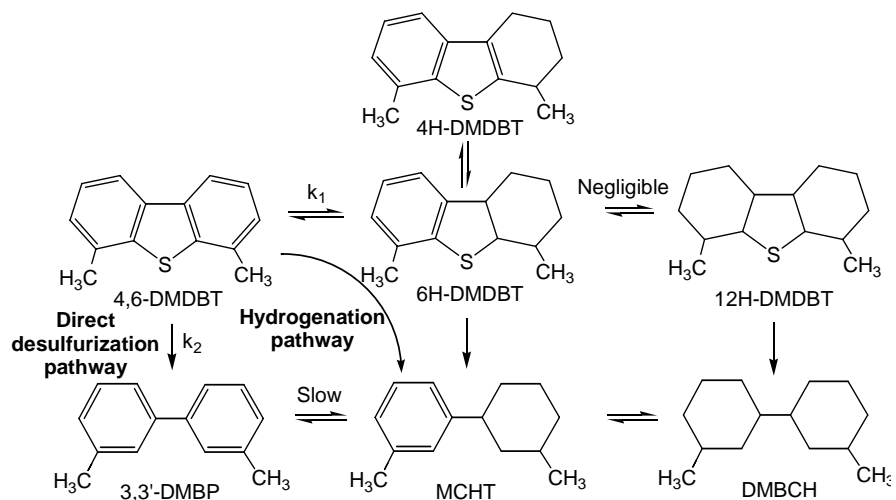


Figure 2.7. Reaction network for 4,6-DMDBT desulfurization

The HYD route proceeds through hexahydrodimethyldibenzothiophene (6-H-DMDBT) and forms methylcyclohexyltoluene (MCHT). The DDS route produces 3,3'-dimethylbiphenyl. Interconversion between these products is believed to be slow, and many studies have taken the ratio of these products to be the ratio k_1/k_2 of rate constants for the HYD and DDS routes. Further hydrogenation of MCHT leads to the ultimate product dimethylbicyclohexane (DM BCH), while the fully hydrogenated 12-hydro-dimethyldibenzothiophene is generally not observed. An accurate determination of the rate constants for the HYD and DDS routes, k_1 and k_2 , was obtained by Song and coworkers using batch reactors at low conversions. The concentration data for 4,6-DMDBT fit first-order kinetics and allowed the calculation of $k_1 + k_2$ by equation (1).

$$\ln(C_{DMDBT} / C_{DMDBT0}) = -(k_1 + k_2) \cdot t \quad (1)$$

The ratio of rate constants k_1/k_2 was obtained by extrapolating the selectivity as defined by equation (2) to zero conversion. The combination of measurements allowed calculation of the individual rate constants.

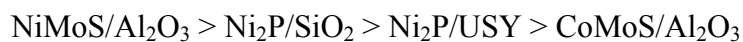
$$\frac{k_1}{k_2} = \frac{[\text{Initial Selectivity of HDMDBTs}]}{[\text{Initial Selectivity of DMBP}]} \quad (2)$$

Comparison was made to two commercial catalysts, CoMoS/Al₂O₃ (Cr344) and NiMoS/Al₂O₃ (Cr424), obtained from the Criterion Catalyst Co. The rate constants are reported in Table 2.3 on a weight and (active site) basis.

Table 2.3. Comparison of rate constants for sulfides and phosphides (573 K and 20.4 atm)

Rate Constant 10 ⁻⁵ s ⁻¹ g·cat ⁻¹ or (s ⁻¹ active site ⁻¹)	CoMo sulfide	NiMo sulfide	Ni ₂ P/USY	Ni ₂ P/SiO ₂
k_1+k_2	34.1 (4.0)	83.2 (8.8)	51.5 (15.2)	66.4 (23.7)
k_1/k_2	1.2	3.2	5.2	10.1
k_1	18.8 (2.2)	63.3 (6.7)	43.2 (12.7)	60.4 (21.6)
k_2	15.3 (1.8)	19.9 (2.1)	8.3 (2.5)	6.0 (2.1)

On a weight basis the overall activity, given by $k_1 + k_2$, followed the order



However, on the basis of active sites the order was



The number of active sites was estimated by the chemisorption of CO for the phosphides and the low-temperature chemisorption of O₂ for the sulfides. The CO method is reasonable for counting the number of surface metal atoms in phosphides [40,68]. The O₂ method is similarly reasonable for estimating the sites on sulfides [53,86], as it is applied at dry ice/acetone temperatures in a pulse manner, so that corrosive chemisorption is minimized [87]. The result that Ni₂P has higher activity than the sulfides on a site basis is significant, as in the initial stages of catalyst discovery the objective is to find materials with high intrinsic rates. In addition, Ni₂P/SiO₂ gave a very high k_1/k_2 ratio, with a value of 10.1, which is much higher than the value of 1.2 for CoMo sulfide and 3.2 for NiMo sulfide. The indications are that Ni₂P is very effective in the HYD pathway, which is usually slow in the sulfides. Studies on acetonitrile hydrogenation over MoP by Li, et al. [88,89] confirmed the high hydrogenation activity of phosphides. In addition, Montesinos-Castellanos, et al. reported a direct relationship between hydrogen adsorption capabilities of Al₂O₃-supported MoP and their corresponding HDS activities [90].

A study by the Rodriguez and collaborators of the electronic properties of SiO₂ supported Ni₂P, MoP, and MoS₂ catalysts using density functional calculations [91] has shown that the electron density around the metal followed the order, MoS₂/SiO₂ < MoP/SiO₂ < Ni₂P/SiO₂, which correlated well with the thiophene HDS activities of the catalysts. It was suggested that the higher electron density on the metal cation could enhance HDS activity by facilitating the dissociation of H₂ and the adsorption of thiophene [91,92]. The presence of P in Ni₂P prevents the compound from being bulk sulfided and allows it to retain metallic properties for hydrogenation.

Extensive work has also been done [93-96] to study the mechanism of hydrodenitrogenation (HDN). HDN is more difficult than HDS, and generally, for heterocyclic compounds is preceded by the hydrogenation of aromatic nitrogen heterorings, before the hydrogenolysis of C-N bonds [97]. Thus the high hydrogenation activity of phosphides is beneficial, and actually a key to deep HDS, as nitrogen compounds are inhibitors.

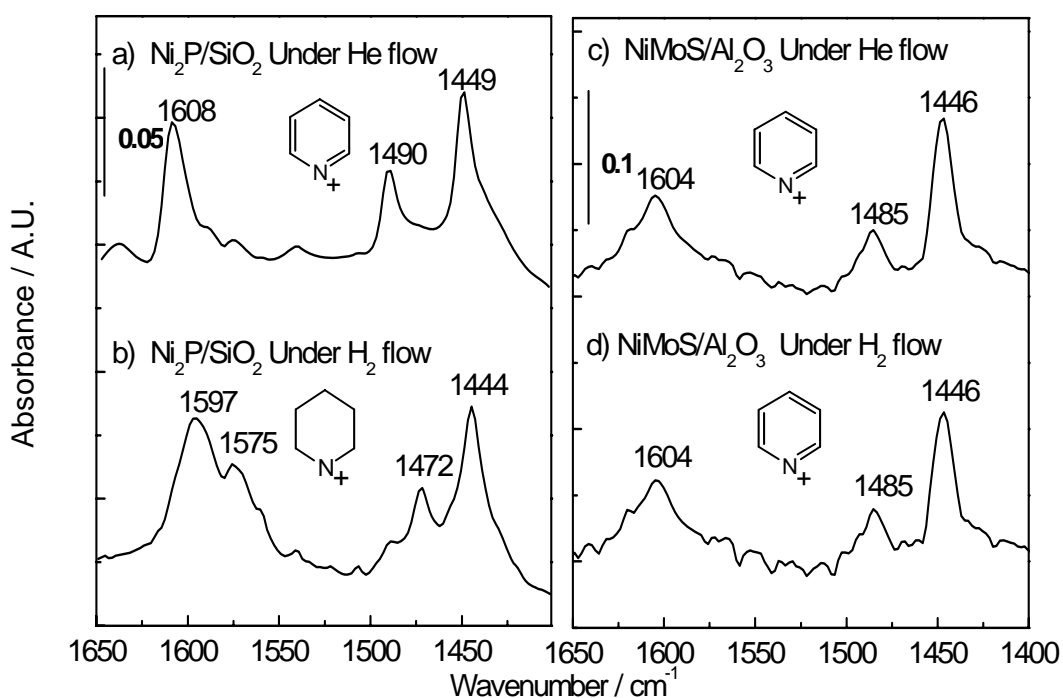


Figure 2.8. In situ FTIR spectra of pyridine on Ni₂P and NiMo

The HDN work was carried out using quinoline, pyridine and 2-methylpiperidine as probe reactants. Infrared measurements at reaction conditions showed that pyridine was readily hydrogenated on Ni₂P/SiO₂ but not on NiMoS/Al₂O₃ [96]. The FTIR spectra in He of pyridine adsorbed on the Ni₂P/SiO₂ (Figure 2.8 a)) and NiMoS/Al₂O₃ (Figure 2.8 c)) show the same

features due to a pyridinium species with bands at 1604-1608 cm^{-1} assigned to ν_{8a} (CC(N)), 1485-1490 cm^{-1} and 1446-1449 cm^{-1} due to ν_{19b} (CC(N)).

When the flow is switched to H_2 the pyridinium signal for the $\text{Ni}_2\text{P}/\text{SiO}_2$ (Figure 2.8 b)) is converted to piperidinium (1597, 1575, 1472 cm^{-1}) while that on $\text{NiMoS}/\text{Al}_2\text{O}_3$ remains unchanged (Fig. 2.8 d)). This confirms the high hydrogenation activity of Ni_2P .

Adsorption of CO was also used to characterize the samples. The sulfided $\text{NiMoS}/\text{Al}_2\text{O}_3$ showed very weak IR peaks (at 2173 cm^{-1} and 2117 cm^{-1}) due to physisorbed CO species on cationic sites, as found in previous studies [98,99,100]. Only at a very low temperature (140 K) did IR bands appear at 2125 cm^{-1} with low intensity [100], indicating a low electron density on the adsorbing metal sites. In contrast to these samples, the $\text{Ni}_2\text{P}/\text{SiO}_2$ gave a distinctive and stable IR band at 2083 cm^{-1} . After sulfidation the peak reappeared at slightly higher frequency of 2086 cm^{-1} with the intensity being slightly diminished. This was previously observed in studies in Bussell's group on $\text{Ni}_2\text{P}/\text{SiO}_2$ [18,19] and was attributed to weakening of the Ni-CO bond by electron withdrawal by sulfur. This frequency fell in the region between that of Ni^+-CO and Ni^0-CO , indicating the presence of π back-bonding in a metal-like state. Also, the IR band for bridging CO species was not observed, which is understandable as the bond distance given by EXAFS between Ni-Ni in Ni_2P is not close enough to form bridging CO groups compared to that in Ni metal. Similar results are found for noble metals in a low oxidation state such as Pt and Pd which are well known as hydrogenation catalysts, and display stable IR bands at low frequency ($\sim 2010 \text{ cm}^{-1}$) at room temperature [101,102]. The noble metals are, however, severely deactivated in a sulfur environment with a loss of active sites [102].

An in-depth study was made of the HDN mechanism of 2-methylpiperidine. As shown by the group of Prins [103], this is an ideal probe molecule for distinguishing between

elimination and substitution pathways. Piperidine can react by either of two pathways (Figure 2.9). The E2 elimination pathway (top) results in the formation of a 6-amino-2-hexene, which is hydrogenated to 1-aminohexane. The S_N2 nucleophilic substitution pathway (bottom) forms 5-amino-1-hexene, which is hydrogenated to 2-amino-hexane.

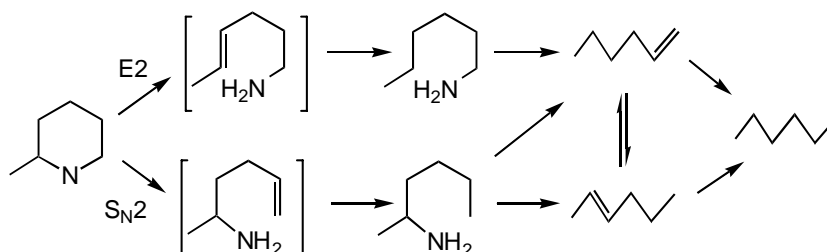


Figure 2.9. Reaction network for 2-methylpiperidine HDN

Results of a flow reactor study at 3.1 MPa and 450-600 K were carried out using a Ni₂P/SiO₂ catalyst [104] (Figure 2.10). For realistic conditions sulfur (3000 ppm) was included in the feed.

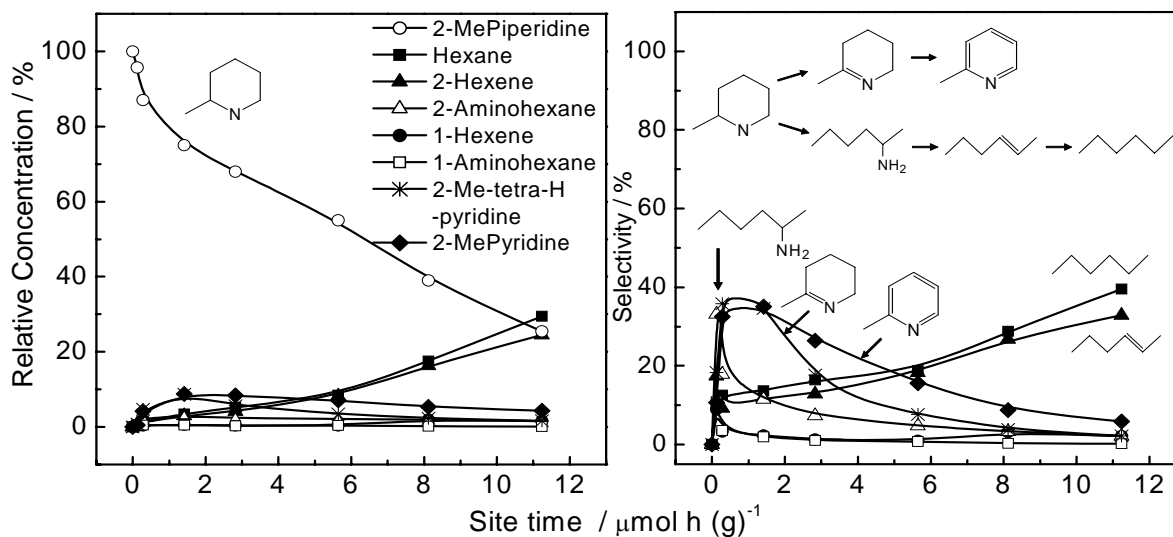


Figure 2.10. Relative concentrations and selectivity in the HDN of 2-methylpiperidine

Analysis of the product distribution as a function of contact time showed that the initial product was 2-aminohexane, indicating that the reaction proceeded predominantly by an S_N2 substitution mechanism, as was found on sulfides [103]. FTIR spectroscopy at reaction conditions of the 2-methylpiperidine indicated that a piperidinium ion intermediate was formed [105]. The intermediate was formed on P-OH groups, which showed a clear band at 3668 cm^{-1} . The assignment of the P-OH group on the $\text{Ni}_2\text{P}/\text{SiO}_2$ had already been addressed in a previous study [94], which showed that the P-OH intensity fell or rose as the piperidine was adsorbed or desorbed. The following reaction sequence (Figure 2.11) accounts for the major observations on the reaction, i.e. the occurrence of an S_N2 step and the involvement of a piperidinium ion intermediate.

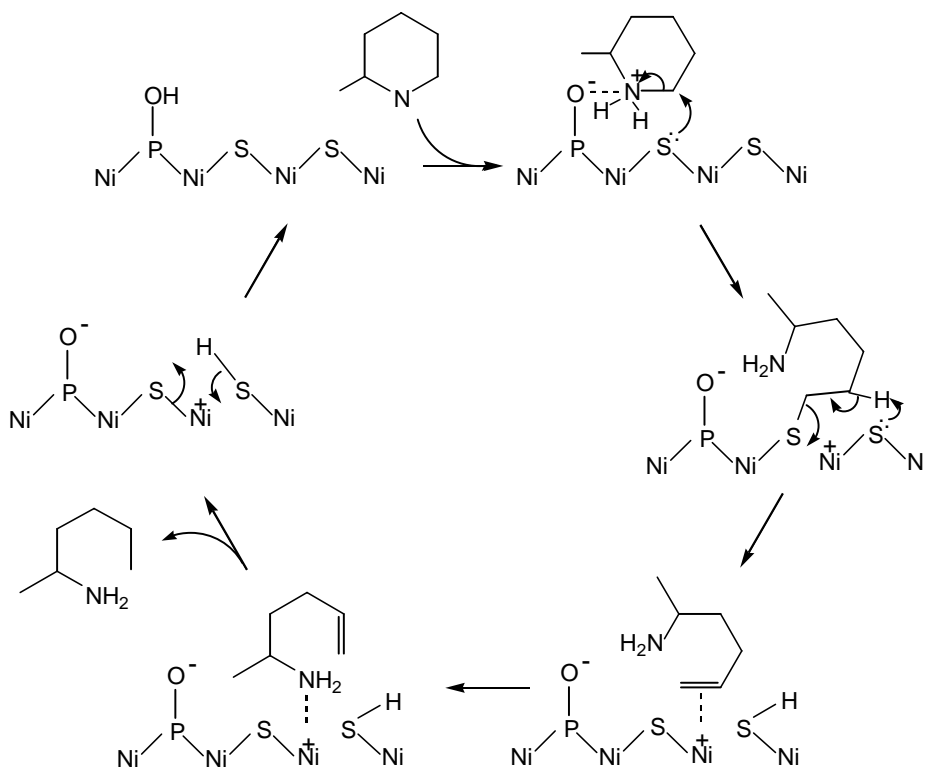


Figure 2.11. Scheme for the HDN of 2-methylpiperidine

At the top left is a depiction of the Ni₂P surface. It shows hydroxyl groups associated with phosphorus as shown by FTIR [94], and the coverage of part of the nickel sites with sulfur as shown by EXAFS [48-52] and calculations [54]. A 2-methylpiperidine molecule interacts with this surface to form an adsorbed piperidinium ion, also observed by FTIR. The lone pairs on a suitably positioned sulfur atom carry out a nucleophilic attack on the open side of the ring. This is in agreement with the finding that HDN proceeds by a substitution mechanism. Subsequent steps involve facile C-S bond breaking reactions.

Kinetics indicate that the nucleophilic attack is the likely rate-determining step, and is supported by the observation of the piperidinium ion, as its high concentration is consistent with its participation in a slow reaction. The C-S bond in the resulting amine intermediate is weak and the species can react rapidly in a variety of ways, including elimination, as shown.

2.4 Bimetallic Systems

As was mentioned earlier, Ni₂P has been found to be the most active among the mono-metallic phosphides. Because of the well known synergism of Co and Ni with Mo in sulfide catalysts, some researchers have investigated mixed metal phosphides like NiMoP and CoMoP [22,106-110]. The surprising finding is that these compositions are poorly active. However, little explanation has been offered, aside from suggestions of alteration of the chemical nature, or interactions with the support. Insight into this unexpected result can be obtained from examining the structure of Ni₂P itself (Figure 2.12), as NiMoP has the same structure.

The structure of Ni₂P is hexagonal [111] with space group: $P_{\bar{6}2m}, D_{3h}^2$, strukturbericht notation: revised C22, and lattice parameters, $a = b = 0.5859$ nm, $c = 0.3382$ nm. The unit cell has two types of Ni and P sites (denoted as Ni(1), Ni(2) and P(1), P(2)), which form two different trigonal prisms.

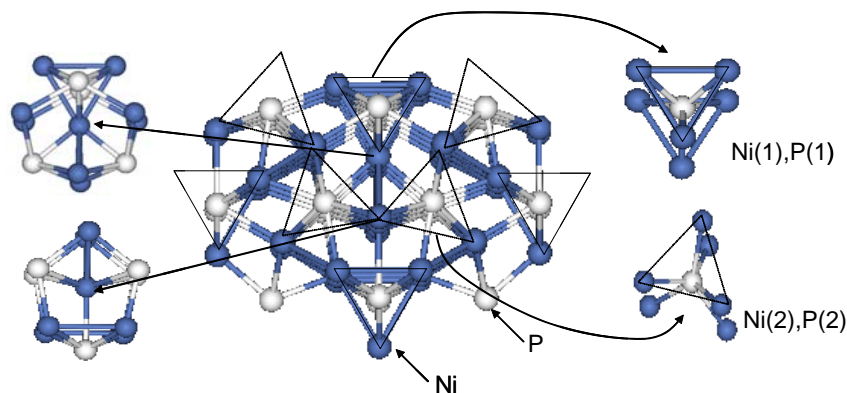


Figure 2.12. Structure of Ni₂P showing P (left) and Ni (right) coordination

Although there are equal numbers of Ni(1) and Ni(2) atoms in the unit cell, they have different surroundings. The Ni(1) site has 4 nearest-neighbor P atoms in a near-tetrahedral geometry (2 at 0.2209 nm, 2 at 0.2266 nm) and 8 more distant Ni neighbors (2 at 0.2613 nm, 2 at 0.2605 nm, and 4 at 0.26783 nm). The Ni(2) site has 5 nearest-neighbor P atoms in a square pyramidal arrangement (1 at 0.2369 nm, 4 at 0.2457 nm) and 6 more distant Ni neighbors (2 at 0.2605 nm, 4 at 0.2678 nm).

An EXAFS study indicates that these two Ni sites can be distinguished by line-shape analysis [112]. Expanding on the previous work on Ni₂P/SiO₂-L and Ni₂P/SiO₂-H [43] as discussed earlier, a Ni₂P sample supported on a silicious MCM-41 support was characterized and its activity was compared to that of the previous samples. The coordination numbers for the first type of Ni (1) are approximately constant, while for the second type of Ni (2) increase as the

surface area of the support increases. This shows that Ni(2) is more prevalent in the smaller crystallites.

The feed employed was more severe than that used earlier (Figure 2.3) and contained 500 ppm (0.05%) S as 4,6-DMDBT, 6000 ppm (0.6%) S as DMDS, 500 ppm (0.05%) N as quinoline, 1% tetralin, and balance tridecane. The conversion at steady-state at 340 °C was 95% for Ni₂P/MCM-41, 82% for Ni₂P/SiO₂-H, and 62% for Ni₂P/SiO₂-L (Table 2.4). The catalytic activity of the supported samples was largest for the highest surface area samples:



This order follows the number of Ni(2) sites, as deduced from the increasing coordination of Ni-P(2) sites (Table 2.4). Overall, the changes in coordination numbers suggest that the number of Ni(2) sites is increasing as the crystallite size goes down. This is because coordination numbers are a measure of the number of bonds. The higher coordination numbers for the Ni-P(2) bonds present a picture of crystallites that have more of these groups as they become smaller, but as the crystallite maintains the bulk Ni₂P structure, this could only arise if the Ni-P(2) bonds are at the surface. Thus, the bulk is terminated with the square pyramidal sites in small crystallites. The square pyramidal sites by definition (five fold coordination vs. tetrahedral) have more P, so the P/Ni ratio increases as crystallite size goes down. The conclusion is that the square pyramidal Ni(2) sites are responsible for the high HDS activity, and constitute the active site.

Table 2.4. Correlation between active sites and catalytic performance

Samples	Surface area $\text{m}^2 \text{g}^{-1}$	D_c nm	Ni-P (1)	Ni-P (2)	Conv. at 613 K	Sel. HYD	Sel. DDS
Ni_2P (bulk)	-	-	2.0	1.75	-	-	-
$\text{Ni}_2\text{P}/\text{SiO}_2\text{-L}$	102	10.1	1.99	2.57	62	34	66
$\text{Ni}_2\text{P}/\text{SiO}_2\text{-H}$	333	6.5	1.98	3.19	82	50	50
$\text{Ni}_2\text{P}/\text{MCM-41}$	487	3.8	1.99	3.48	95	65	35

Returning to the poor activity of NiMoP, it happens that in NiMoP the Mo sites substitute in the Ni(2) sites [113], and this readily accounts for the reduction of activity in this compound. The structure of CoMoP is different [114], but since both CoP and MoP have relatively poor activity, the lack of exceptional activity in CoMoP can be rationalized. That particular sites will have enhanced activity is not surprising. Rodriguez and coworkers have examined the role of P sites in single crystal Ni₂P(001) surfaces and found that they enhance the activity of Ni through a ligand effect [115], and the group of Nelson has identified a stable Ni₃PS site [54].

2.5. Conclusions

The synopsis presented above described the properties of transition metal phosphides and presented detailed studies of the most active of the catalysts, Ni₂P. The coverage included structural analysis of the active phase during reaction, and mechanistic studies which provide a detailed picture of the properties of nickel phosphide catalysts. It was shown that highly dispersed Ni₂P is particularly active for HDS and resistant to S and N-compounds. It was suggested that a stronger interaction between Ni and P in small particles could enhance the sulfur resistance. Also, the activation of N-compounds is probably related to the acidic properties of the Ni₂P, which provides sites for the formation of the protonated N-compounds as intermediate species in HDN. These results therefore imply that the remarkable activity of the supported Ni₂P catalyst has its origin in the proximity of the Ni and P species which is responsible for the creation of proximal sites of high activity in hydrogenation and the activation of N-and S-compounds.

References

- [1] B. Aronsson, T. Lundström and S. Rundqvist, *Borides, Silicides and Phosphides*, Methuen, London and Wiley, New York, 1965.
- [2] D.E.C. Corbridge, *Studies in Inorganic Chemistry*, Vol. 10, 4th Ed., Elsevier, Amsterdam, 1990.
- [3] M. Baudler, *Angew. Chem., Int. Ed. Engl.*, 26 (1987) 419.
- [4] S.T. Oyama, *Transition Metal Carbides, Nitrides, and Phosphides*, in *Handbook of Catalysis*, G. Ertl, H. Knözinger, J. Weitkamp, Eds., Springer-Verlag, Weinheim, 2008.
- [5] S. Rundqvist, *Colloq. Int. Cent. Nat. Rech. Sci.*, 157 (1967) 85.
- [6] D.C. Phillips, S.J. Sawhill, R. Self, M.E. Bussell, *J. Catal.*, 207 (2002) 266.
- [7] S.J. Sawhill, D.C. Phillips, M.E. Bussell, *J. Catal.*, 215 (2003) 208.
- [8] R. Iwamoto, J. Grimblot, *Adv. Catal.*, 44 (1999) 417.
- [9] F. Nozaki, M. Tokumi, *J. Catal.*, 79 (1983) 207.
- [10] F. Nozaki, T. Kitoh, T. Sodesawa, *J. Catal.*, 62 (1980) 286.
- [11] W.R.A.M. Robinson, J.N.M. van Gastel, T.I. Korányi, S. Eijsbouts, J.A.R. van Veen, V.H.J. de Beer, *J. Catal.*, 161 (1996) 539.
- [12] X. Liu, J. Chen, J. Zhang, *Catal. Commun.*, 8 (2007) 1905.
- [13] S. Zhou, J. Chen, X. Liu, J. Zhang, *Chin. J. Catal.*, 28 (2007) 498.
- [14] J. Chen, S. Zhou, X. Liu, J. Zhang, *Catal. Lett.*, 122 (2008) 167.
- [15] W. Li, B. Dhandapani, S.T. Oyama, *Chem. Lett.*, 27 (1998) 207.
- [16] C. Stinner, Z. Tang, M. Haouas, Th. Weber, *J. Catal.*, 208 (2002) 456.

-
- [17] V. Zuzaniuk, R. Prins, *J. Catal.*, 219 (2003) 85.
- [18] K.A. Layman, M.E. Bussell, *J. Phys. Chem. B*, 108 (2004) 10930.
- [19] S.J. Sawhill, K.A. Layman, D.R. Van Wyk, M.H. Engelhard, C. Wang, M.E. Bussell, *J. Catal.*, 231 (2005) 300.
- [20] A.W. Burns, K.A. Layman, D.H. Bale, M.E. Bussell, *Appl. Catal. A: Gen.*, 343 (2008) 68.
- [21] Z. Wu, F. Sun, W. Wu, Z. Feng, C. Liang, Z. Wei, C. Li, *J. Catal.*, 222 (2004) 41.
- [22] F. Sun, W. Wu, Z. Wu, J. Guo, Z. Wei, Y. Yang, Z. Jiang, F. Tian, C. Li, *J. Catal.*, 228 (2004) 298.
- [23] F. Sun, Z. Wei, P. Ying, X. Sun, Z. Jiang, F. Tian, Y. Yang, C. Li, *Cuihua Xuebao*, 25 (2004) 685.
- [24] S. Yang, C. Liang, R. Prins, *J. Catal.*, 237 (2006) 118.
- [25] S. Yang, C. Liang, R. Prins, *Stud. Surf. Sci. Catal.*, 162 (2006) 307.
- [26] H. Loboué, C. Guillot-Deudon, A.F. Popa, A. Lafond, B. Rebours, C. Pichon, T. Cseri, G. Berhault, C. Geantet, *Catal. Today*, 130 (2008) 63.
- [27] L. Song, W. Li, G. Wang, M. Zhang, K. Tao, *Catal. Today*, 125 (2007) 137.
- [28] R. Cheng, Y. Shu, L. Li, J. Sun, X. Wang, T. Zhang, *Thermochim. Acta*, 450 (2006) 42.
- [29] R. Cheng, Y. Shu, L. Li, M. Zheng, X. Wang, A. Wang, T. Zhang, *Appl. Catal. A: Gen.*, 316 (2007) 160.
- [30] S. Yang, C. Liang, R. Prins, *J. Catal.*, 241 (2006) 465.
- [31] S. Liu, Y. Qian, X. Ma, *Mater. Lett.*, 62 (2008) 11.

-
- [32] S. Liu, X. Liu, L. Xu, Y. Qian, X. Ma, *J. Cryst. Growth*, 304 (2007) 430.
- [33] K. Senevirathne, A.W. Burns, M.E. Bussell, S.L. Brock, *Adv. Funct. Mater.*, 17 (2007) 3933.
- [34] S. Burns, J.S.J. Hargreaves, S.M. Hunter, *Catal. Commun.*, 8 (2007) 931.
- [35] P. Clark, X. Wang, S.T. Oyama, *J. Catal.*, 207 (2002) 256.
- [36] G. Sun, C. Li, F. Li, Z. Zhou, *Shiyou Xuebao, Shiyou Jiagong*, 21 (2005) 54.
- [37] S.J. Sawhill, K.A. Layman, D.R. Van Wyk, M.H. Engelhard, C. Wang, M.E. Bussell, *J. Catal.*, 231 (2005) 300.
- [38] X. Wang, P. Clark, S.T. Oyama, *J. Catal.*, 208 (2002) 321.
- [39] S.T. Oyama, P. Clark, V.L.S. Teixeira da Silva, E.J. Ledesma, F.G. Requejo, *J. Phys. Chem. B*, 105 (2001) 4961.
- [40] X. Wang, Y. Lee, W.J. Chun, S.T. Oyama, F. Requejo, *J. Catal.*, 210 (2002) 207.
- [41] S.T. Oyama, P. Clark, X. Wang, T. Shido, Y. Iwasawa, S. Hayashi, *J. Phys. Chem. B*, 106 (2002) 1913.
- [42] S.T. Oyama, X. Wang, F. Requejo, T. Sato, Y. Yoshimura, *J. Catal.*, 209 (2002) 1, Priority Communication.
- [43] Y. Shu, Y.-K. Lee, S.T. Oyama, *J. Catal.*, 236 (2005) 112.
- [44] A. Montesinos-Castellanos, T.A. Zepeda, B. Pawelec, E. Lima, J.L.G. Fierro, A. Olivas, J.A. de los Reyes H., *Appl. Catal. A: Gen.*, 334 (2008) 330.
- [45] E.P.W. Ward, I. Arslan, A. Bleloch, J.M. Thomas, P.A. Midgley, P. Alisivatos, *J. Phys.: Conf. Ser.*, 26 (2005) 207.

-
- [46] R. Esparza, J.A. Ascencio, G. Rosas, J.F. Ramirez Sanchez, U. Pal, R. Perez, J. Nanosci. Nanotech., 5 (2005) 641.
- [47] M.S. Chen, D.W. Goodman, Science, 306 (2004) 252.
- [48] S.T. Oyama, X. Wang, Y.-K. Lee, W.-J. Chun, J. Catal., 221 (2004) 263.
- [49] Y.-K. Lee, S.T. Oyama, ACS Fuel Chem. Div. Prep., 50 (2005) 807.
- [50] Y.-K. Lee, S.T. Oyama, Proc. 4th ASIA-PACIFIC Chemical Reaction Engineering Symposium, (2005). Stud. Surf. Sci. Catal., (2006) 159.
- [51] T. Kawai, S. Sato, W.J. Chun, K. Asakura, K.K. Bando, T. Matsui, Y. Yoshimura, T. Kubota, Y. Okamoto, Y.-K. Lee, S.T. Oyama, Physica Scripta, T115 (2004) 822.
- [52] T. Kawai, K.K. Bando, Y.-K. Lee, S.T. Oyama, W.-J. Chun, K. Asakura, J. Catal., 241 (2006) 20, Priority Communication.
- [53] S.J. Tauster, T.A. Pecoraro, R.R. Chianelli, J. Catal., 63 (1980) 515.
- [54] A.E. Nelson, M. Sun, A.S.M. Junaid, J. Catal., 241 (2006) 180.
- [55] M. Boudart, R.A. Dalla Betta, K. Foger, D.G. Loffler, M.G. Samant, Science, 228 (1985) 717.
- [56] J.P. van den Berg, J.P. Lucien, G. Germaine, G.L.B. Thielemans, Fuel Process. Technol., 35 (1993) 119.
- [57] F.E. Massoth, S.C. Kim, Catal. Lett., 57 (1999) 129.
- [58] J.-D. Grunwaldt, M. Ramin, M. Rohr, A. Michailovski, G.R. Patzke, A. Baiker, Rev. Sci. Instrum., 76 (2005) 054104.

-
- [59] N. Weiher, E. Bus, B. Gorzolnik, M. Möller, R. Prins, J.A. van Bokhoven, J. Synchrotron Rad., 12 (2005) 675.
- [60] J.F. Odzak, A.M. Argo, F.S. Lai, B.C. Gates, K. Pandya, L. Feraria, Rev. Sci. Instr., 72 (2001) 3943.
- [61] E. Larsson, Arkiv. Kemi., 23 (1965) 335.
- [62] O.N. Il'nitskaya, L.G. Aksel'rud, S.L. Mikhalenko, Yu B. Kuz'ma, Kristallografiya, 32 (1987) 50.
- [63] J. Trahan, R.G. Goodrich, S. F. Watkins, Phys. Rev. B 2, [3]2 (1970) 2859.
- [64] T. Fujii, K. Tanaka, F. Marumo, Y. Noda, Mineral J., 13 (1987) 448.
- [65] J.B. Parise, Acta Cryst. B, 36 (1980) 1179.
- [66] Y. Shu, Y.-K. Lee, S.T. Oyama, Chem. Commun., (2005) 1143.
- [67] Y. Shu, S.T. Oyama, Carbon, 43 (2005) 1517.
- [68] P.A. Clark, S.T. Oyama, J. Catal., 218 (2003) 78.
- [69] A. Wang, L. Ruan, Y. Teng, X. Li, M. Lu, J. Ren, Y. Wang, Y. Hu, J. Catal., 229 (2005) 314.
- [70] I.I. Abu, K.J. Smith, Appl. Catal. A: Gen., 328 (2007) 58.
- [71] M. Lu, A. Wang, X. Li, X. Duan, Y. Teng, Y. Wang, C. Song, Y. Hu, Energy Fuels, 21 (2007) 554.
- [72] T.I. Korányi, Z. Vít, D.G. Poduval, R. Ryoo, H.S. Kim, E.J.M. Hensen, J. Catal., 253 (2008) 119.
- [73] T.I. Korányi, Z. Vít, J.B. Nagy, Catal. Today, 130 (2008) 80.
- [74] Y.-K. Lee, Y. Shu, S.T. Oyama, Appl. Catal. A: Gen., 322 (2006) 191.

-
- [75] J.H. Kim, X. Ma, C. Song, Y.-K. Lee, S.T. Oyama, *Energy Fuels*, 19 (2005) 353.
- [76] V. Vanrysselberghe, G.F. Froment, *Ind. Eng. Chem. Res.*, 35 (1996) 3311.
- [77] V. Vanrysselberghe, R.L. Gall, G.F. Froment, *Ind. Eng. Chem. Res.*, 37 (1998) 1235.
- [78] G.H. Singhal, R.L. Espino, J.E. Sobel, G.A. Huff, Jr., *J. Catal.*, 67 (1981) 457.
- [79] D.D. Whitehurst, T. Isoda, I. Mochida, *Adv. Catal.*, 42 (1998) 345.
- [80] H. Farag, D.D. Whitehurst, K. Sakanishi, I. Mochida, *Catal. Today*, 50 (1999) 49.
- [81] V. Meille, E. Schulz, M. Lemaire, M. Vrinat, *J. Catal.*, 170 (1997) 29.
- [82] F. Bataille, J.L. Lemberon, P. Michaud, G. Pérot, M. Vrinat, M. Lemaire, E. Schulz, M. Breysse, S. Kasztelan, *J. Catal.*, 191 (2000) 409.
- [83] P. Steiner, E.A. Blekkan, *Fuel Proc. Tech.*, 79 (2002) 1.
- [84] C. Kwak, J.J. Lee, J.S. Bae, K. Choi, S.H. Moon, *Appl. Catal. A: Gen.*, 200 (2000) 233.
- [85] C.J. Song, C. Kwak, S.H. Moon, *Catal. Today*, 74 (2002) 193.
- [86] W. Zmierczak, G. MuraliDhar, F.E. Massoth, *J. Catal.*, 77 (1982) 432.
- [87] T.A. Bodrero, C.H. Bartholomew, K.C. Pratt, *J. Catal.*, 78 (1982) 253.
- [88] P. Yang, Z. Jiang, P. Ying, C. Li, *Chin. J. Catal.*, 28 (2007) 670.
- [89] P. Yang, Z. Jiang, P. Ying, C. Li, *J. Catal.*, 253 (2008) 66.
- [90] A. Montesinos-Castellanos, T.A. Zepeda, B. Pawelec, J.L.G. Fierro, J.A. de los Reyes, *Chem. Mater.*, 19 (2007) 5627.
- [91] J.A. José A. Rodriguez, J.-Y. Kim, J.C. Hanson, S.J. Sawhill, M.E. Bussell, *J. Phys. Chem. B*, 107 (2003) 6276.

-
- [92] J.A. Rodriguez, *J. Phys. Chem. B*, 101 (1997) 7524.
- [93] J.H. Kim, X. Ma, C. Song, Y.K. Lee, S.T. Oyama, *ACS Fuel Chem. Div. Prep.*, 49 (2004) 44.
- [94] S.T. Oyama, Y.-K. Lee, *J. Phys. Chem. B*, 109 (2005) 2109.
- [95] Y.-K. Lee, S.T. Oyama, *ACS Petr. Chem. Div. Prep.*, 50 (2005) 445.
- [96] Y.-K. Lee, S.T. Oyama, *J. Catal.*, 239 (2006) 376.
- [97] G. Perot, *Catal. Today*, 10 (1991) 447.
- [98] B. Müller, A.D. van Langeveld, J.A. Moulijn, H. Knözinger, *J. Phys. Chem.*, 97 (1993) 9028.
- [99] M. Angulo, F. Maugé, J.C. Duchet, J.C. Lavalley, *Bull. Soc. Chim. Belg.*, 96 (1987) 925.
- [100] B.M. Vogelaar, P. Steiner, A.D. van Langeveld, S. Eijsbouts, J.A. Moulijn, *Appl. Catal. A: Gen.*, 251 (2003) 85.
- [101] L. Hu, G. Xia, L. Qu, M. Li, C. Li, Q. Xin, D. Li, *J. Catal.*, 202 (2001) 220.
- [102] B.H. Cooper, B.B.L. Donnis, *Appl. Catal. A: Gen.*, 137 (1996) 203.
- [103] M. Egorova, Y. Zhao, P. Kukulka, R. Prins, *J. Catal.*, 206 (2002) 263.
- [104] S.T. Oyama, Y.-K. Lee, *J. Phys. Chem. B*, 109 (2005) 2109.
- [105] Y.-K. Lee, S.T. Oyama, *J. Catal.*, 239 (2006) 376.
- [106] C. Stinner, R. Prins, Th. Weber, *J. Catal.*, 202 (2001) 187.
- [107] J.A. Rodriguez, J.-Y. Kim, J.C. Hanson, S.J. Sawhill, M.E. Bussell, *J. Phys. Chem. B*, 2003, 6276.

-
- [108] D. Ma, T. Xiao, S. Xie, W. Zhou, S.L. Gonzalez-Cortes, M.L.H. Green, *Chem. Mater.*, 16 (2004) 2697.
- [109] I.I. Abu, K.J. Smith, *J. Catal.*, 241 (2006) 356.
- [110] I.I. Abu, K.J. Smith, *Catal. Today*, 125 (2007) 248.
- [111] S. Rundqvist, *Acta Chem. Scand.*, 16 (1962) 992.
- [112] S.T. Oyama, Y.-K. Lee, *J. Catal.*, (2008) In press.
- [113] P.R. Guérin, M. Sergent, *Acta Cryst. B*, 33 (1977) 2820.
- [114] P.R. Guérin, M. Sergent, *Acta Cryst. B*, 34 (1978) 3312.
- [115] P. Liu, J.A. Rodriguez, T. Asakura, J. Gomes, K. Nakamura, *J. Phys. Chem. B*, 109 (2005) 4575.

Chapter 3

Kinetic Method for Studying Reactive Surface Intermediates:

The Hydrodenitrogenation of Pyridine over Ni₂P/SiO₂

3.1. Introduction

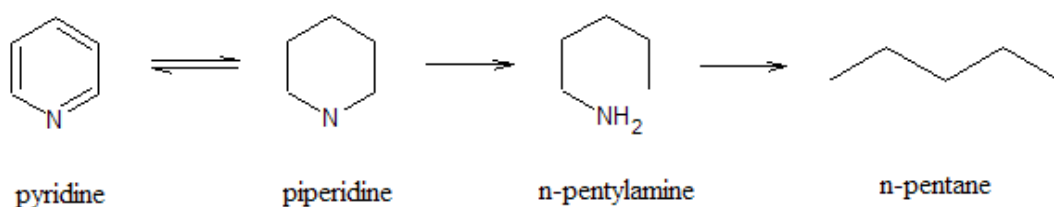
Increasing requirements for environmentally benign fuels have prompted considerable research in the area of hydrotreating of petroleum feedstocks. Combustion of fossil fuels lead to emission of particulate matter, SO_x, NO_x, olefins and aromatics that poison exhaust control devices and contribute to the production of acid rain, smog and atmospheric ozone [1,2]. Recently enacted environmental regulations have made removal of sulfur and nitrogen a focal concern for the refining industry. By 2010, the maximum permitted amount of sulfur in gasoline and diesel fuel will be 10 ppm in the United States, the European Union and Japan. Similar specifications are also targeted in other countries and will probably be a worldwide standard in the next decade [3]. Such levels correspond to removal of +99.95 % of sulfur from a typical gas oil containing 2 wt. % sulfur, and the removal process has been named deep hydrodesulfurization (HDS).

The removal of nitrogen compounds from petroleum crudes by hydrodenitrogenation (HDN) occurs simultaneously with other catalytic hydrotreating processes. The nitrogen content in petroleum crudes is generally 5 to 20 times lower than the sulfur content. However, compared to sulfur heterocycles, nitrogen compounds are

more difficult to hydroprocess and generally require higher temperatures, higher hydrogen pressures and lower space velocities [4]. If not removed, basic nitrogen compounds greatly inhibit HDS because of their preferential adsorption on catalytic sites [5]. Thus, the ability to carry out efficient HDN is key to deep HDS as the reaction rate of sulfur removal is markedly affected by small amounts of basic nitrogen compounds in the range 0 – 50 ppm [6-8]. Several studies of the inhibiting effects of nitrogen compounds on the HDS of refractory sulfur compounds have shown that basic nitrogen heterocycles in particular inhibit the rate of HDS. The inhibition is most pronounced for hydrogenation sites because of strong adsorption on these centers [9-11]. Under conditions of deep HDS the amount of nitrogen compounds becomes dominant or comparable to refractory sulfur compounds and strongly competes in the heteroatom removal process. Minimizing the inhibiting effect by efficient removal of nitrogen is vital to achieve low levels of sulfur. As a result, detailed study of HDN mechanisms and surface kinetics of adsorbed nitrogen compounds is important for improving catalytic activity for HDN.

Nitrogen heterocycles are composed of single or multi-ring compounds containing a six-membered pyridinic ring (basic nitrogen compounds) or a five-membered pyrrolic ring (nonbasic). Pyridine, a six-membered nitrogen heterocycle, is a classic probe molecule and is the simplest basic nitrogen compound for studying HDN. A considerable number of studies have been conducted on the mechanism of pyridine HDN. In general, the denitrogenation of heterocyclic nitrogen compounds is preceded by hydrogenation of the aromatic heterocyclic ring in order to convert strong aromatic C—N bonds into weaker aliphatic C—N bonds. Subsequent removal of nitrogen proceeds by

cleavage of a C—N bond to form an amine intermediate followed by removal of nitrogen to yield hydrocarbons and NH₃. It has been documented that the pyridine HDN reaction follows an established sequence of steps as shown in Scheme 3.1 – hydrogenation of the heterocyclic aromatic ring to yield piperidine, ring opening by cleavage of one C—N bond and subsequent removal of nitrogen from n-pentylamine as NH₃ [12,13]. However, Ledoux et al. showed that ring opening is possible prior to complete saturation of the heterocyclic aromatic ring [14]. More complex reaction networks have been proposed which included disproportionation reactions of saturated products to form N-pentylpiperidine, though condensation products were only observed at high temperatures and pressures [15,16].



Scheme 3.1. Simplified reaction pathway for pyridine HDN

Polycyclic aromatic nitrogen compounds such as quinoline and carbazole are among the most refractory nitrogen compounds. Quinoline has a double ring structure containing a benzene ring fused to pyridine at adjacent carbon atoms. Similarly, carbazole possesses a triple ring structure with two carbocyclic rings bonded to the adjacent carbon atoms of pyrrole. The reactions involved in the HDN of polycyclic nitrogen compounds involve hydrogenation of the nitrogen heteroring, hydrogenation of

the benzenic ring(s) and C—N bond cleavage [13]. Details of the mechanisms of quinoline HDN has been studied extensively by Prins and coworkers [17,18] and carbazole HDN by Abu and Smith [19,20]. The HDN of these molecules proceeds through multiple parallel pathways involving hydrogenation and hydrogenolysis of C—N bonds. However, the HDN of all nitrogen heterocycles entails the common steps of heterocyclic ring hydrogenation, ring opening and the final removal of nitrogen as NH₃. As a result, study of the HDN of pyridine or pyrrole can be used to investigate the essential steps of HDN.

Recently, new insight was provided on the HDN mechanism by Prins and coworkers [21] in a study on 2-methylpyridine and 2-methylpiperidine HDN over sulfided NiMo/ γ -Al₂O₃. The HDN of 2,3,4,5-tetrahydro-6-methylpyridine, which was previously reported as an intermediate in the hydrogenation/dehydrogenation of 2-methylpyridine/2-methylpiperidine, was examined [22]. The study concluded that 2-methylpyridine is hydrogenated to 2-methylpiperidine and that both amines react to form partially hydrogenated intermediates, the imines 2,3,4,5-tetrahydro-2-methylpyridine and 2,3,4,5-tetrahydro-6-methylpyridine. Ring opening of the imines occurs by addition of H₂S, elimination, and hydrogenation to form amino-hexanethiols. Subsequently, the thiols react by hydrogenolysis to hexylamines, and the second C—N bond is cleaved by hexylimine formation, H₂S addition and elimination of NH₃. As a result, the imines were proposed to be intermediates of both hydrogenation and denitrogenation. The proposed reaction sequence is different from those given in previous studies in which a direct reaction of 2-methylpiperidine to ring-opened products was assumed.

The reaction rates of the first two steps, hydrogenation of the aromatic ring and ring-opening, are of similar order of magnitude and slow relative to subsequent steps in the mechanism. Several studies have observed a pyridine-piperidine thermodynamic equilibrium under conventional HDN conditions, suggesting that aromatic ring hydrogenation is fast compared to ring-opening [23-25]. Still yet, many studies have provided evidence of either step being rate-limiting and the slow step depends on the amine and experimental conditions such as catalyst properties, temperature, pressure and H₂S/H₂ ratio [26-31].

Pyridine adsorption is often combined with in situ Fourier transform infrared spectroscopy (FTIR) to probe the surface acidic properties of supports and catalysts. Characteristic bands in the FTIR spectrum are used to determine if pyridine is protonated through the nitrogen atom by surface Brønsted acid sites and/or bonded to coordinative unsaturated metal sites (Lewis acids). Upon interaction with a Brønsted acid site, pyridine is protonated to a pyridinium ion and absorbs at a specific IR wavenumber around 1545 – 1540 cm⁻¹. Interaction of pyridine with a Lewis acid sites leads to a coordinatively bonded pyridinium complex with a well-resolved band centered around 1452 – 1447 cm⁻¹. A band located around 1490 cm⁻¹ is common to both adsorbed species. In addition, the different pyridine – acid site interactions give rise to other specific absorbances as discussed later. Many studies have employed this technique to qualitatively and quantitatively study the acidic properties of catalytic materials and the resulting effect on catalyst properties and activity [32].

Damyanova and coworkers investigated changes in the surface acidity upon impregnation of Mo on mixed ZrO₂-SiO₂ and ZrO₂-Al₂O₃ [33]. Rana and coworkers

examined changes in support acidity upon incorporation of MgO, SiO₂, TiO₂ and ZrO₂ with Al₂O₃ [34]. Sánchez-Minero and coworkers studied pyridine adsorption on Al₂O₃ and Al₂O₃ modified with 10 wt.% SiO₂. On pure Al₂O₃ they found the presence of two Lewis acid sites with different strength – Al³⁺ in octahedral and tetrahedral coordination environments. Incorporation of SiO₂ led to partial covering of some Lewis acid sites with only octahedral Al³⁺ sites remaining on the surface [35]. DeCanio and Weissman used pyridine adsorption to correlate HDN activity with surface acidity of boron-modified NiMo/Al₂O₃ catalysts. They determined that nitrogen removal activity was dependent on Brønsted acidity as measured by the pyridinium band at 1540 cm⁻¹ [36]. Korányi and coworkers investigated the effects of sulfidation on the acidity of conventional hydrotreating catalysts supported on Al₂O₃ and amorphous SiO₂-Al₂O₃. Sulfidation of the catalyst samples was found to decrease the Brønsted and Lewis acidities of all samples [37]. Navarro and coworkers studied the effects of Ru incorporation on the surface acid properties of conventional hydrotreating catalysts. Introduction of Ru was found to enhance both the Brønsted and Lewis acidities of the samples [38]. Park and coworkers employed FTIR measurements of adsorbed pyridine to examine the promoting effects of Ni on Mo/Al₂O₃ and W as a secondary promoter on the acidic properties and HDN activity. Enhancement of HDN activity with addition of Ni was attributed to an improvement of the reducibility of the oxidic Mo/Al₂O₃ sample rather than an increase in Brønsted acidity. Further enhancement of activity with W as a secondary promoter was ascribed to the formation of new Brønsted acid sites [39].

Previous studies in our group have employed in situ Fourier transform infrared spectroscopy (FTIR) to probe the surface acidic properties of conventional and novel

hydrotreating catalysts. The FTIR spectra in He of pyridine adsorbed on Ni₂P/SiO₂ and NiMoS/Al₂O₃ showed similar features that were assigned to the presence of a surface pyridinium species on both catalysts. When the flow was switched to H₂, the pyridinium species on Ni₂P/SiO₂ was hydrogenated and the presence of a piperidinium species was observed. However, on NiMoS/Al₂O₃ little change occurred in the spectrum. These observations were attributed to the high hydrogenation activity of Ni₂P/SiO₂ as compared to the conventional hydrotreating catalyst NiMoS/Al₂O₃ [40]. The question arises as to the kinetic role of the adsorbed pyridinium species under reaction conditions. It is desirable to determine whether the pyridinium surface species is a true reaction intermediate or if it exist on the catalyst surface as a spectator, with no role in the overall HDN kinetics.

Directly monitoring the surface concentration of an adsorbed surface species during adsorption and reaction is a powerful tool for elucidating kinetic and mechanistic information [41]. Such studies involve measuring the rates of adsorption and reaction under transient conditions and comparing the transient rates with the overall reaction rate measured under steady-state conditions. Agreement between the separately measured rates constitutes proof that the observed intermediate is a true reaction intermediate and is kinetically significant in the overall reaction kinetics. The present study will use this method to investigate the role of the adsorbed pyridinium species during the HDN of pyridine over Ni₂P/SiO₂ at 423 K and atmospheric pressure.

3.2. Experimental

3.2.1. Materials

The support used in this study was amorphous fumed silica (Cabosil, EH-5 grade). The catalyst precursors were nickel nitrate hexahydrate, $\text{Ni}(\text{NO}_3)_2 \cdot 6\text{H}_2\text{O}$ (Aesar, 99%), and ammonium hydrogen phosphate, $(\text{NH}_4)_2\text{HPO}_4$ (Aldrich, 99%). The chemicals used in the study of pyridine hydrodenitrogenation were pyridine (Aesar, 99.5+% spectrophotometric grade), piperidine (Aldrich, 99.9%), n-nonane (Aesar, 99%) and n-tridecane (Aesar, 99%). All chemicals were used as received. The gases employed were He (Airgas, UPC grade), H_2 (Airgas, UPC grade), N_2 (Airgas, UPC grade) and CO (Linde Research Grade, 99.97%). The gases were passed through two-stage gas purifiers (Alltech, model 4658) to remove moisture and oxygen. Additionally, 0.5% O_2/He (Airgas, UHP grade), which was used for passivation of reduced samples, was passed through a purifier to remove moisture.

3.2.2. Catalyst Samples

The catalyst used in this study was a nickel phosphide supported on silica, $\text{Ni}_2\text{P}/\text{SiO}_2$. The phosphide was prepared with excess phosphorous ($\text{Ni}/\text{P} = 1/2$) and a loading of 1.15 mmol Ni/g support (12.2 wt % $\text{Ni}_2\text{P}/\text{SiO}_2$). The synthesis of the supported catalyst involved two steps and was reported previously [42-44]. Briefly, in the first step, a supported nickel phosphate was prepared by incipient wetness impregnation of nickel and phosphorous precursors, followed by drying at 393 K for 6 h and calcination at 673 K for 4 h. In the second step, the phosphate was reduced to a

phosphide by temperature-programmed reduction (TPR). After the temperature program, the sample was cooled to room temperature in flowing He and passivated in a flow of 0.5 % O₂/He for 4 h.

3.2.3. Characterization

The Ni₂P/SiO₂ catalyst and blank SiO₂ were characterized by BET surface area measurements, powder X-ray diffractometry (XRD) and CO chemisorption. A Micromeritics ASAP 2010 micropore size analyzer was used to measure the specific surface area of the samples from the linear portion of BET plots ($P/P_0 = 0.02 - 0.10$) at 77 K. Before the measurement, the samples were degassed for 6 h at 413 K. X-Ray diffraction patterns of the passivated catalyst sample and blank support were acquired using a Scintag XDS-2000 powder diffractometer operated at 45 kV and 40 mA with Cu-K_α monochromatized radiation ($\lambda = 0.1542$ nm). Irreversible CO uptake measurements were obtained using a flow technique and were used to titrate the surface metal atoms and provide an estimate of active sites on the catalyst. The CO chemisorption amounts were obtained by pulsing calibrated volumes of CO (19.6 μmol) into a He carrier and measuring the decrease in peak areas caused by adsorption. The measurements were conducted using a standard flow system equipped with a computer-interfaced mass spectrometer (Dycor/Ametek, model MA100). Before the measurement, 0.2 g of passivated catalyst sample was placed in a U-shaped quartz reactor and rereduced in flowing H₂ at 723 K for 2 h. After the pretreatment, the samples were cooled to room temperature under He at a flow rate of 100 cm³/min. Calibrated pulses of CO were then

passed over the samples to measure the total dynamic uptake. The CO uptake amounts were used to calculate turnover frequencies in the steady-state kinetic measurements.

3.2.4. Spectroscopic and Kinetic Measurements

Transmission infrared spectra of pyridine adsorbed on Ni₂P/SiO₂ and blank SiO₂ were collected with a combined in situ reactor–spectrometer system (Figure 3.1). Fourier transform infrared (FTIR) spectra were collected with a Digilab Excalibur Series FTS 3000 spectrometer equipped with a liquid N₂ cooled mercury-cadmium-telluride detector. The low volume in situ reactor was equipped with water cooled KBr windows, connections for inlet and outlet flows, and thermocouples connected to a temperature controller to monitor and control the sample temperature. For all experiments, 25 mg of finely ground Ni₂P/SiO₂ or blank SiO₂ were pressed into self-supporting wafers with a diameter of 13 mm (18.8 mg/cm²). Wafers were mounted vertically in a quartz sample holder to keep the incident IR beam normal to the samples. Rods of CaF₂ (13 mm diameter) were placed on both sides of the sample to minimize interference of gas phase pyridine and to reduce the dead volume of the in situ reactor.

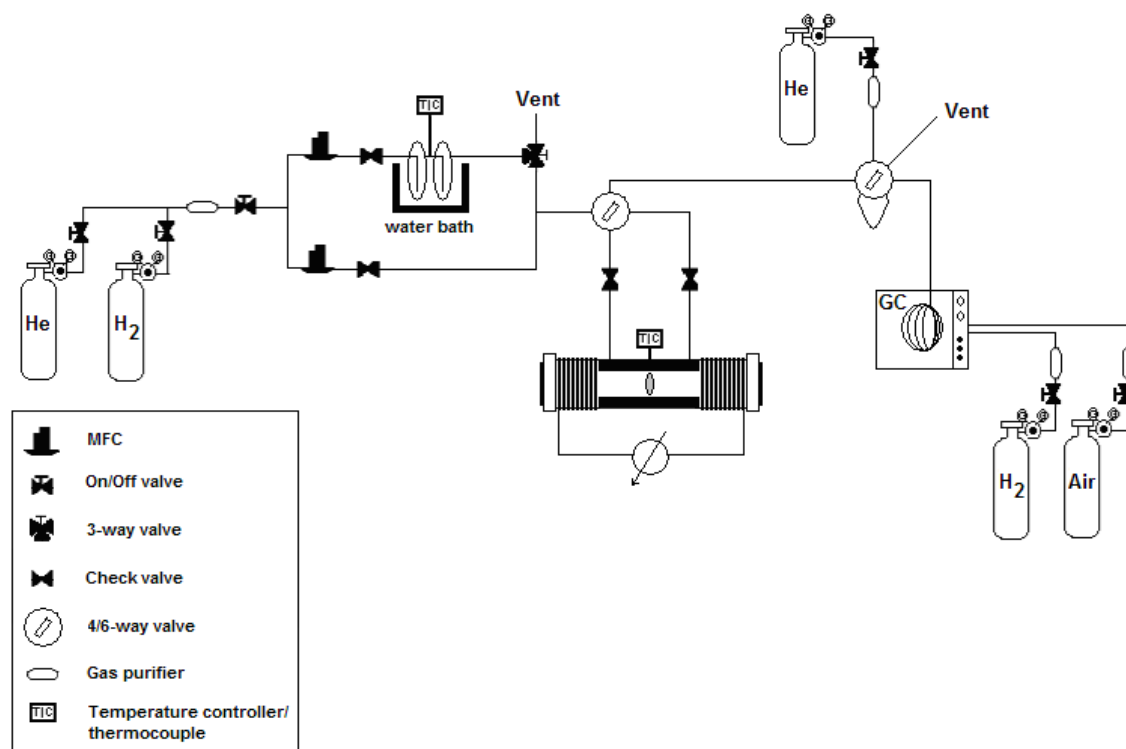


Figure 3.1. In situ FTIR reactor system

A previous FTIR spectroscopy study on Ni₂P/SiO₂ identified high concentration of a pyridinium surface species when pyridine in a He carrier was adsorbed on the sample. Upon shifting to H₂ flow, the adsorbed pyridine was converted to piperidine and a piperidinium species was dominant on the surface [40]. Studies of the effect of temperature were conducted on Ni₂P/SiO₂ and blank SiO₂ to confirm the identity and determine the stability of the adsorbed pyridinium intermediate. For these experiments, absorbance spectra were collected in the range 4000-1000 cm⁻¹ at a resolution of 4 cm⁻¹ with 64 scans/spectrum. Before dosing pyridine, the Ni₂P/SiO₂ and blank SiO₂ samples were pretreated in H₂ for 2 h at 723 K at a flow rate of 82 μmol/s (120 cm³/min). After reduction, the samples were slowly cooled in flowing He or H₂ (200 cm³/min) and

background spectra were collected in the absence of pyridine at 523, 473, 423, and 373 K. The samples were dosed at atmospheric pressure and 373 K with 1.0 mol % pyridine in He or H₂ carrier at a total flow rate of 140 $\mu\text{mol/s}$ (200 cm^3/min) until saturation was achieved. The samples were then purged with carrier gas for 300 s to remove gaseous and weakly adsorbed pyridine. Spectra are shown with subtraction of the background contribution to highlight the pyridine adsorbate peaks. Spectra were acquired at 373, 473, 573 and 673 K with a heating rate of 0.083 K/s (5 K/min). The reactor temperature was held constant at each temperature for 180 s to collect the corresponding spectrum.

Transient FTIR experiments were performed to ascertain the kinetic role of the pyridinium surface species by measuring the rate of reaction of the adsorbed pyridine intermediate. The dependency of the reaction rate on the concentration of pyridinium intermediate was studied by varying the surface coverage of pyridine. FTIR spectroscopy was used to directly monitor the evolution of pyridinium coverage with respect to time at atmospheric pressure and 423 K. For these experiments, absorbance spectra were collected in multi-scan mode in the range 4000 – 1000 cm^{-1} at a resolution of 4 cm^{-1} . Spectra were collected every 6 s with 10 scans/spectrum. Before all measurements, the self-supporting Ni₂P/SiO₂ wafers were pretreated in H₂ for 2 h at 723 K at a flow rate of 82 $\mu\text{mol/s}$ (120 cm^3/min). After the reduction, the samples were cooled in flowing He or H₂ (200 cm^3/min) to 423 K and background spectra were collected in the absence of pyridine. The flow was then quickly switched to pyridine and carrier gas and collection of spectra was initiated. The samples were dosed with pyridine in He or H₂ carrier at a total flow rate of 200 cm^3/min . All measurements were started with a clean sample surface and continued until steady-state coverage of pyridine was

attained. The carrier gas was passed through a pyridine-filled bubbler immersed in a temperature-controlled water bath held at 298 K. The Antoine equation was used to obtain the pyridine vapor pressure (2.81 kPa at 298 K):

$$\log P^{sat} = A - \frac{B}{T + C} \quad (1)$$

where P^{sat} is the vapor pressure in mmHg, T is the bubbler temperature in °C and the coefficients are 7.1874, 1463.63 and 224.598 for A , B and C , respectively [45]. The concentration of pyridine was adjusted by blending the main carrier flow containing pyridine with a dilution gas while keeping the total flow rate constant at 200 cm³/min. Vapor-phase concentrations of pyridine were varied to measure the reaction rates over a range of weight times. The weight time (g*h/mol) is a measure of contact time and was calculated with the following equation:

$$\text{Pyridine Weight time} = \frac{W_{catalyst}}{\dot{N}_{pyridine}} \quad (2)$$

where $W_{catalyst}$ is the mass of catalyst (0.025 g) and $\dot{N}_{pyridine}$ is the molar flow rate of pyridine in mol/h. Table 3.1 summarizes the flow rates and weight times that were used in the transient kinetic experiments.

Table 3.1.
Pyridine weight times for gas-phase transient kinetic experiments

Carrier gas flow rate / cm ³ (NTP) min ⁻¹	Pyridine flow rate · 10 ³ / mol h ⁻¹	Pyridine concentration / mol%	Weight time / g·h mol ⁻¹
15	1.1	0.21	24
30	2.1	0.43	12
45	3.2	0.64	7.9
60	4.2	0.85	6.0
75	5.2	1.1	4.8
90	6.3	1.3	4.0

For each spectrum a peak at 1491 cm⁻¹, corresponding to pyridine ring vibrations on Brønsted and Lewis acid sites (mode ν_{19b}) of Ni₂P/SiO₂, was monitored as a function of time. The areas of the peak were converted to fractional coverage by separate calibration experiments to determine the areas corresponding to full coverage ($\theta = 1$). Briefly, for the calibrations the Ni₂P/SiO₂ catalyst sample was pretreated as mentioned above. After reduction, the sample was cooled to 298 K in He at a flow rate of 140 $\mu\text{mol/s}$ (200 cm³/min) and a background spectrum was collected in the absence of pyridine. A lower sample temperature for the calibration experiments was necessary to obtain saturation coverage on the catalyst surface. The sample was then dosed with successively higher concentrations of pyridine in He carrier until saturation coverage of pyridine was achieved. Complete saturation was considered to be attained when peak areas were invariant with increasing gas-phase pyridine concentrations. The area corresponding to full coverage of Brønsted and Lewis acid sites by pyridine was used to calculate fractional coverage in the transient experiments. In order to account for slight

differences in wafer thickness, all peak areas determined in the transient and calibration experiments were normalized by the areas of the ν_{OH} stretching frequencies of the SiO_2 support. The ν_{OH} frequencies, which were recorded in the background spectra before exposure to pyridine, were found in the $4000 - 3200 \text{ cm}^{-1}$ region of the spectra.

The dependency of the reaction rate on the concentration of the adsorbed pyridine species was determined by adsorbing pyridine on the $\text{Ni}_2\text{P}/\text{SiO}_2$ samples in both He and H_2 carriers. The evolution of the coverage (θ) of pyridine on acidic sites was plotted as a function of time. Rates were determined by extrapolating the slope ($d\theta/dt$) in the transient region of the adsorption isotherms to time zero. The derivative was expressed in units of turnover frequency (TOF, s^{-1}). In He carrier, the corresponding TOF included the net rate of adsorption of pyridine in the absence of any surface reaction:

$$\left(\frac{d\theta}{dt}\right)_{\text{He}} = r_{\text{ads}} - r_{\text{des}} \quad (3)$$

where r_{ads} corresponded to the rate of pyridine adsorption and r_{des} represented the rate of pyridine desorption from the catalyst surface. In H_2 carrier, the rate included both sorption and reaction:

$$\left(\frac{d\theta}{dt}\right)_{\text{H}_2} = r_{\text{ads}} - r_{\text{des}} - r_{\text{rxn}} \quad (4)$$

where r_{rxn} is the rate of surface reaction of pyridine. For each pyridine weight time, the rate of surface reaction was determined by subtraction of the independently determined rates:

$$\left(\frac{d\theta}{dt}\right)_{\text{He}} - \left(\frac{d\theta}{dt}\right)_{\text{H}_2} = r_{\text{rxn}} \quad (5)$$

The reaction rate was used to determine the rate of reaction of the adsorbed pyridinium intermediate at steady-state. The measured rates were compared with the overall turnover frequency of pyridine determined in a separate experiment.

The overall turnover rates of pyridine were measured in a three-phase trickle-bed reactor (Figure 3.2). The reactor has a concentric tubular design with an outer stainless steel body and an inner quartz sleeve which prevents contact of the catalyst with the stainless steel. The tight-fitting quartz sleeve (18 mm o.d., 15 mm i.d.) is sealed at the top of the reactor with compression fittings but is loose at the bottom to allow pressure equalization. The flow of the gas and liquid reactant mixture enters from the top and passes through Pyrex beads for preheating and good flow dispersion. The catalyst is held by quartz wool plugs. An axial thermocouple in a quartz sheath was used to measure the temperature of the catalyst bed. The reactor was heated with a furnace and the temperature of the catalyst bed was controlled with a temperature controller. The liquid feed was metered from burettes with a high-pressure liquid pump (Lab Alliance, Model Series I) and H₂ flow was delivered by mass flow controllers (Brooks, Model 5850E). The gas and liquid passed over the catalyst bed in down-flow mode and into a water-cooled separation/sampling system. The gas-liquid mixture was separated by gravity in a 50 cm³ cylinder which held the effluent liquid for intermittent sampling. Excess liquid was collected in a second 500 cm³ cylinder located below the sampling section of the system. Liquid samples were collected every 2 or 3 h in sealed septum vials and were analyzed off-line with a gas chromatograph (Hewlett-Packard, 5890A) equipped with a 0.32 mm i.d. X 50 m fused silica capillary column (CPSil-5CB, Chrompack, Inc.) and a

flame ionization detector. Reactants and products were identified by matching retention times to standards injected separately.

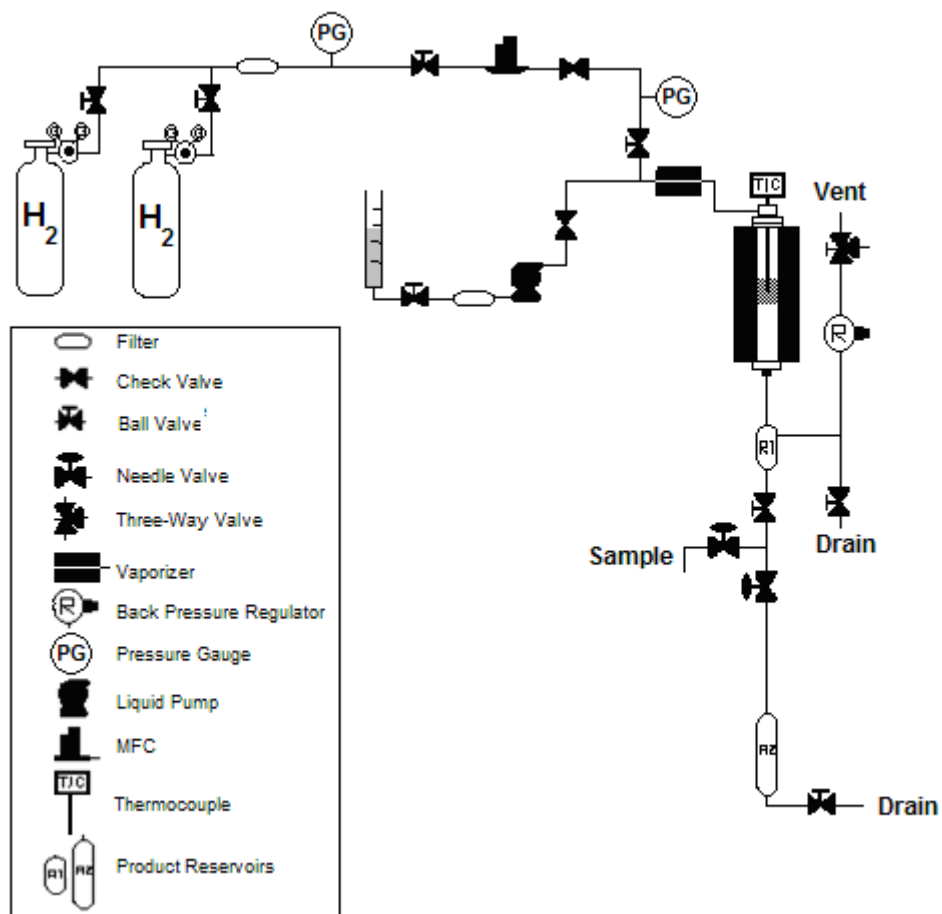


Figure 3.2. Three-phase trickle bed reactor system

For the measurements of the turnover rates of pyridine, the system was operated at 423 K and atmospheric pressure with a liquid feed containing 20000 ppm wt. (2.0 wt%) N as pyridine, 20000 ppm wt. (2.0 wt%) n-nonane as internal standard and balance n-tridecane as solvent. The Ni_2P/SiO_2 catalyst was in pelletized form (16/20 mesh) and was supported between quartz wool plugs. For the liquid-phase reactions, 0.100 g of

sample was charged to the reactor and diluted with SiC to a total bed volume of 8 cm³ to ensure plug flow conditions. The remaining volume of the reactor was filled with 3 mm Pyrex beads. Prior to the kinetic measurements, the sample was pretreated at 723 K for 2 h under 120 cm³/min of flowing H₂ at atmospheric pressure. After reduction, the reactor was cooled to 423 K and the H₂ flow rate was increased to 140 μmol/s (200 cm³/min). Liquid feed was then introduced and the reaction was allowed to stabilize for 25 h before sampling. Additionally, the system was allowed to run for 25 h after every change in flow rate. Flow rates of the liquid feed were varied to match the weight times used in the transient FTIR experiments. The overall turnover frequency was obtained from the following formula:

$$\text{TOF} = \frac{\text{pyridine flow rate } (\mu\text{mol/s}) \cdot \text{steady-state conversion}}{\text{catalyst weight (g)} \cdot \text{chemisorption uptake } (\mu\text{mol/g})} \quad (6)$$

where the catalyst weight was 0.100 g for all experiments. The results from several samples were averaged to determine the steady-state conversion at each weight time. Table 3.2 summarizes the pyridine flow rates employed in the kinetic measurements.

Table 3.2.
Pyridine weight times for steady-state kinetic experiments

Pyridine flow rate · 10 ³ / mol h ⁻¹	Weight time / g·h mol ⁻¹
7.3	14
9.3	11
15	6.6
20	5.0

3.3. Results and Discussion

3.3.1. Characterization

The BET specific surface area and CO chemisorption uptake of the supported Ni₂P sample are listed in Table 3.3. As stated earlier, the CO uptake value was used to calculate turnover frequencies in the steady-state kinetic experiments. The BET surface area was much lower than that of the blank support. This could be due to sintering of the active phase at the elevated temperatures used in the synthesis. Figure 3.3 shows the powder XRD pattern of the reduced Ni₂P/SiO₂ catalyst after passivation. The pattern exhibits a broad peak at $2\theta \sim 22^\circ$ due to the amorphous SiO₂ support. At higher angles the XRD pattern for Ni₂P/SiO₂ confirms the formation of the Ni₂P phase with peaks at $2\theta \sim 41^\circ, 45^\circ, 48^\circ$ and 55° . The phase corresponds to hexagonal Ni₂P which adopts the Fe₂P structure with space group P_{62m} [46]. The pattern of a reference Ni₂P from the powder diffraction file (PDF 3-953) is also presented [47].

Table 3.3.
Physical properties of Ni₂P/SiO₂ catalyst

	BET surface area / m ² g ⁻¹	CO uptake / μmol g ⁻¹	Metal dispersion / %	Particle size / nm
Ni ₂ P/SiO ₂	148 (333) ^a	90	8	11

^a BET surface area of the blank SiO₂ support

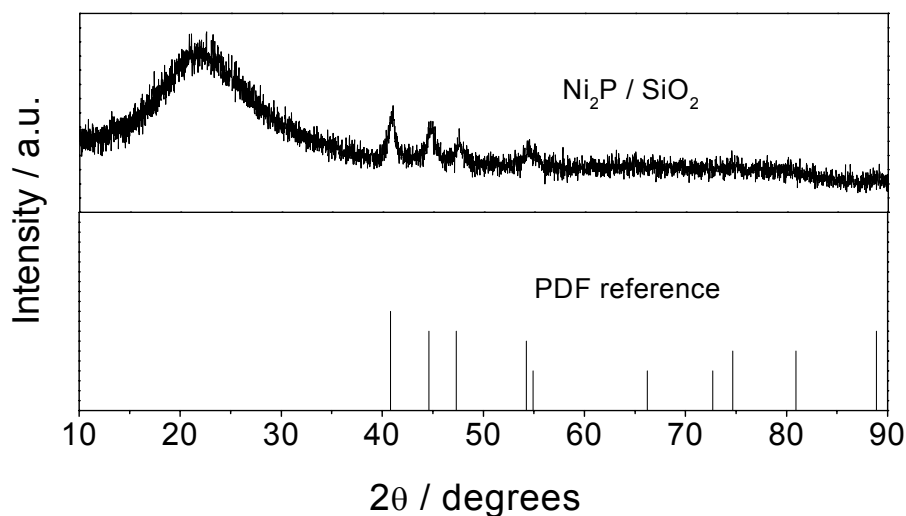


Figure 3.3. Powder XRD pattern of Ni₂P/SiO₂ catalyst sample

3.3.2. FTIR Spectral Interpretation

Figure 3.4 shows the FTIR spectrum of 0.85 mol% pyridine in He carrier adsorbed on Ni₂P/SiO₂ at 423 K. The left panel shows the high wavenumber region of the spectrum and the right panel highlights the low wavenumber region. Included in the figures are peak positions and band assignments where BPY, LPY, HPY and PPY signify pyridine interacting with Brønsted acid sites, Lewis acid sites, hydrogen-bonded pyridine and physisorbed pyridine, respectively. In the high wavenumber region, the main spectral features include two negative peaks at 3745 and 3669 cm⁻¹ and three positive features centered at 3143, 3079 and 3046 cm⁻¹. In this figure, as well as in others in this study, background spectra were subtracted as explained in the experimental section. The negative bands at 3745 and 3669 cm⁻¹ are assigned to hydroxyl vibrations of the SiO₂ support and P-OH of the active phase, respectively [30,48]. The three features located at 3143, 3079 and 3046 cm⁻¹ correspond to aromatic ν_{CH} modes of pyridine [49]. In the low

wavenumber region the main spectral features are located at 1638, 1607, 1595, 1576, 1547, 1491 and 1447 cm^{-1} . Additionally, a shoulder at $\sim 1433 \text{ cm}^{-1}$ is apparent on the low wavenumber side of the peak located at 1447 cm^{-1} . The peaks at 1547, 1491 and 1447 cm^{-1} correspond to pyridinium ring breathing modes 19b ($\nu_{\text{CC}(\text{N})}$) on Brønsted acid sites, 19a ($\nu_{\text{CC}(\text{N})}$) on Brønsted and Lewis acid sites, and 19b ($\nu_{\text{CC}(\text{N})}$) for pyridine coordinated to Lewis acid sites, respectively [49]. The feature at 1447 cm^{-1} also contains a contribution from pyridine hydrogen-bonded (mode 19b, $\nu_{\text{CC}(\text{N})}$) to the SiO_2 support. This mode arises at slightly lower wavenumbers at 1445 cm^{-1} . The weak shoulder at $\sim 1433 \text{ cm}^{-1}$ on the band at 1447 cm^{-1} is assigned to physisorbed pyridine on the SiO_2 support. The broad feature at 1638 cm^{-1} corresponds to mode 8a ($\nu_{\text{CC}(\text{N})}$) on Brønsted acid sites. The peak at 1607 cm^{-1} is tentatively assigned to mode 8a ($\nu_{\text{CC}(\text{N})}$) of pyridine coordinated to Lewis acid sites [50]. As shown later, this band is retained up to 523 K and is thus strongly held on the Ni_2P surface. The features at 1595 and 1576 cm^{-1} likely correspond to 8a modes ($\nu_{\text{CC}(\text{N})}$) of pyridine hydrogen-bonded to the SiO_2 support.

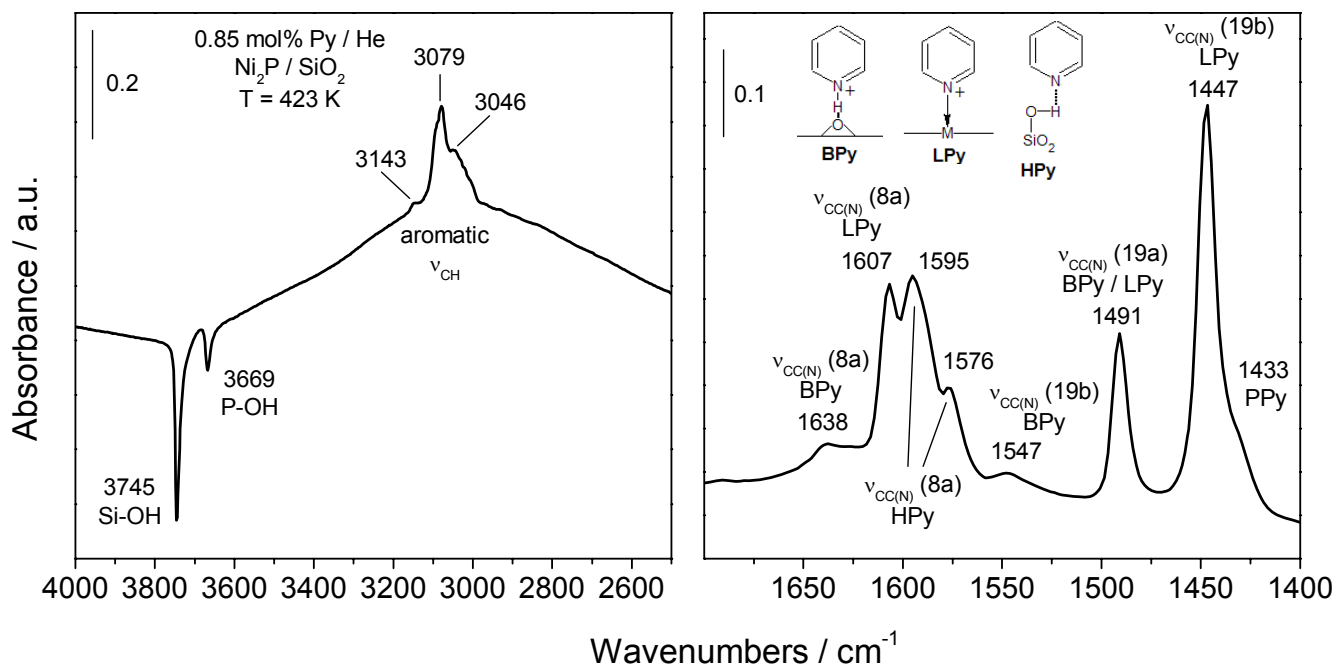


Figure 3.4. FTIR spectrum of 0.85 mol% pyridine in He flow adsorbed on Ni₂P/SiO₂ at 423 K

Figure 3.5 shows the FTIR spectrum of 0.85 mol% pyridine in H₂ carrier adsorbed on Ni₂P/SiO₂ at 423 K. The left panel shows the high wavenumber region of the spectrum and the right panel highlights the low wavenumber region. The spectra appear similar to those obtained for pyridine adsorbed on Ni₂P/SiO₂ in He flow. In the high wavenumber region, the two negative peaks at 3745 and 3669 cm⁻¹ corresponding to Si-OH and P-OH vibrations, respectively, are again observed. In the low wavenumber region, the peaks located at 1638 and 1547 cm⁻¹ are again observed and appear unchanged. However, there are several important differences. The peaks corresponding to aromatic v_{CH} modes of pyridine are shifted to slightly lower wavenumbers at 3138,

3076 and 3038 cm^{-1} . Two new weak features centered at 2957 and 2874 cm^{-1} are now visible and correspond to aliphatic ν_{CH} modes [51]. The intensities of the features located at 1491 and 1447 cm^{-1} are slightly attenuated. The intensity of the peak at 1607 cm^{-1} is much lower than the peak observed under He flow and appears as a shoulder of the peak at 1595 cm^{-1} . Under H_2 flow, a new unidentified peak with strong intensity is observed at 1481 cm^{-1} . The new feature overlaps with the peak at 1491 cm^{-1} but is clearly observed, even at low concentrations of pyridine in H_2 carrier. Moreover, the feature is never observed under He flow. This peak is assigned to a partially hydrogenated pyridine molecule, possibly 2,3,4,5-tetrahydropyridine, in view of the aliphatic ν_{CH} modes. A similar species was previously reported by the group of Prins [31].

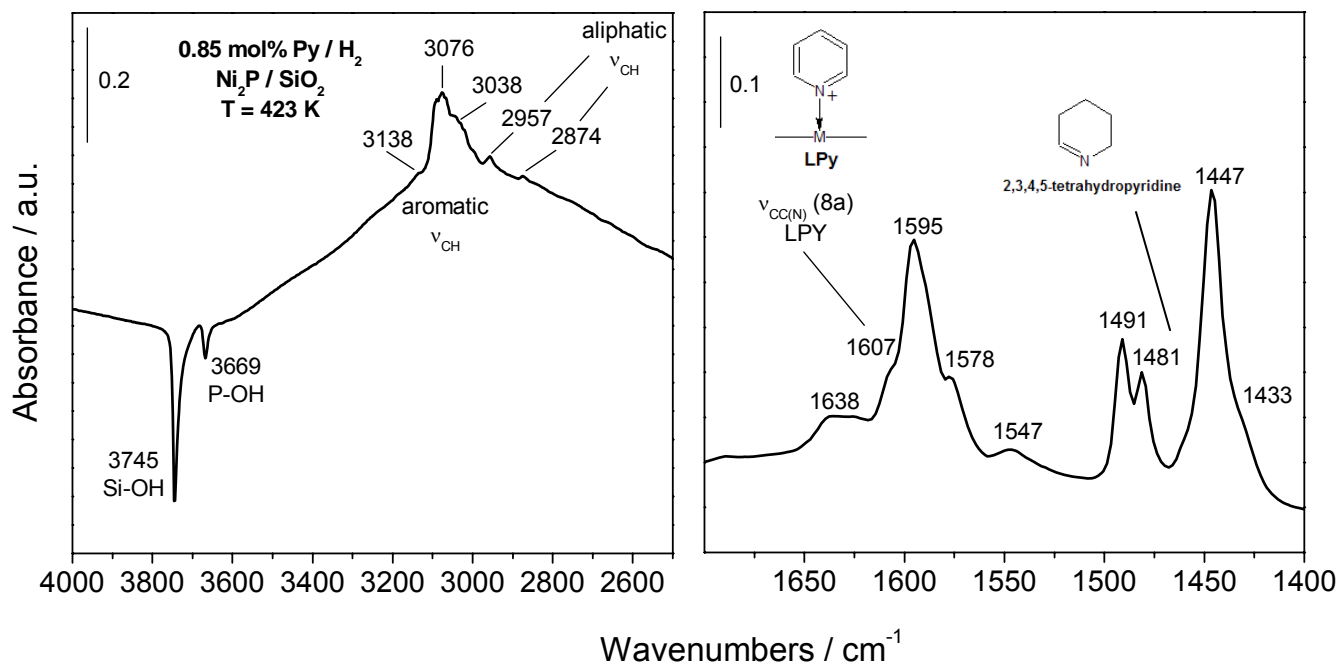


Figure 3.5. FTIR spectrum of 0.85 mol% pyridine in H_2 flow adsorbed on $\text{Ni}_2\text{P}/\text{SiO}_2$ at 423 K

In order to probe the identity of the peak at 1481 cm^{-1} , piperidine at a concentration of 0.85 mol% in He carrier was adsorbed on the $\text{Ni}_2\text{P}/\text{SiO}_2$ catalyst at 423 K, as shown in Figure 3.6. The left panel shows the high wavenumber region of the spectrum and the right panel shows the low wavenumber region. The spectrum for piperidine on $\text{Ni}_2\text{P}/\text{SiO}_2$ is substantially different from that of pyridine adsorption. In the high wavenumber region, two negative peaks are again observed at 3745 and 3669 cm^{-1} . A prominent shoulder on a rising background was also located at $\sim 3265\text{ cm}^{-1}$ and is assigned to a ν_{NH} stretching mode of piperidine [51]. As expected, no contributions due to aromatic ν_{CH} modes are observed but several strong peaks corresponding to aliphatic ν_{CH} vibrations are observed at 2943 , 2864 , 2806 and 2739 cm^{-1} . In the low wavenumber region there is a new broad feature centered at 1620 cm^{-1} . A previous study on 2-methylpiperidine adsorption on $\text{Ni}_2\text{P}/\text{SiO}_2$ assigned this band to the NH_2 scissoring mode arising from the protonation of the piperidine nitrogen atom and formation of an adsorbed piperidinium intermediate. The other major spectral features in the low wavenumber region included two strong, overlapping peaks located at 1474 and 1458 cm^{-1} . Analogous to the results obtained for 2-methylpiperidine adsorption, these overlapping bands correspond to $\nu_{\text{C-C}}$ and $\nu_{\text{C-N}}$ stretching modes [30]. Also, the peak at 1458 cm^{-1} has a prominent shoulder at $\sim 1450\text{ cm}^{-1}$ likely due to piperidine hydrogen-bonded (HPip) to the SiO_2 support. As can be seen from the piperidine adsorption spectrum, no peak centered at 1481 cm^{-1} was observed. Upon switching the carrier flow to H_2 , no significant changes in the spectrum were observed.

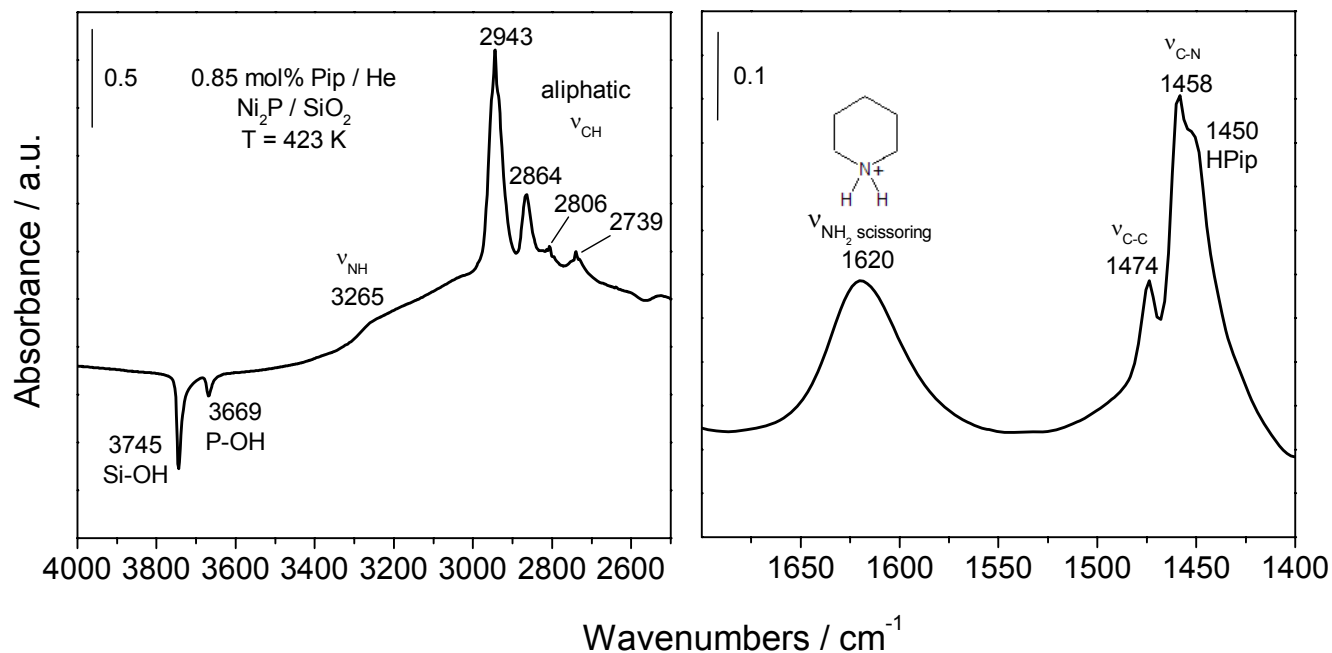


Figure 3.6. FTIR spectrum of 0.85 mol% piperidine in He flow adsorbed on $\text{Ni}_2\text{P}/\text{SiO}_2$ at 423 K

3.3.3. FTIR Spectroscopy Measurements

Figure 3.7 shows the FTIR spectra of pyridine adsorbed on the blank SiO_2 support under He flow after a brief degassing. The left and right panels show the high and low wavenumbers regions of the spectra. The main spectral features are located at 3748, 3738, 3090, 3078, 3044, 3021, 1593, 1575, 1445 and 1433 cm^{-1} . The absorbance peaks at 3748 and 3738 cm^{-1} appear as negative features and correspond to surface hydroxyl groups of SiO_2 . For all spectra, because of the background subtraction a decrease in the intensity of a negative peak with increasing temperature indicates growth of the peak. As a result, as the temperature is increased, the concentrations of the hydroxyl functionalities

are increasing even though the intensities of the peaks are decreasing. The opposite applies to positive features in the spectra. As the temperature is increased to 523 K the intensities of all features in the spectra decrease, and so do the corresponding concentrations.

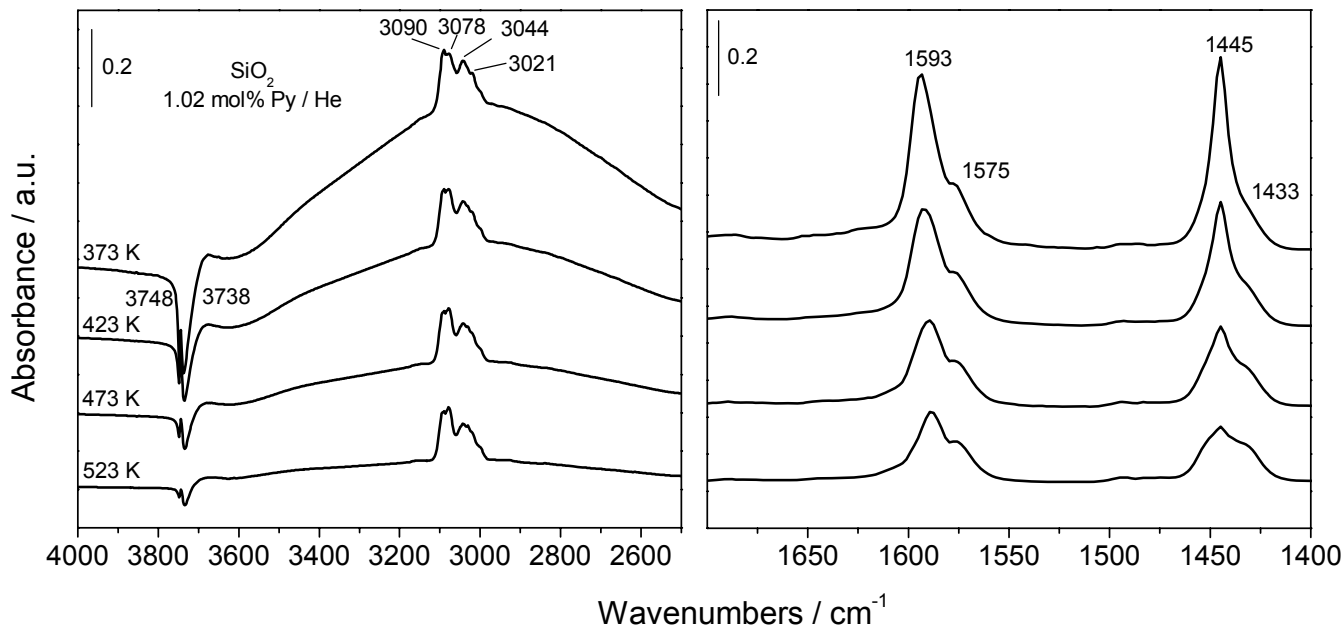


Figure 3.7. FTIR spectra of pyridine adsorbed on SiO₂ in He flow as a function of temperature

Figure 3.8 shows the FTIR spectra of pyridine adsorbed on Ni₂P/SiO₂ under He flow after degassing. The main spectral features are centered at 3745, 3669, 3143, 3079, 1638, 1607, 1595, 1576, 1547, 1491 and 1447 cm⁻¹. The spectra appear similar to pyridine adsorbed on blank SiO₂, but several new peaks are now present. The negative features corresponding to hydroxyl groups of SiO₂ now appear as a single band that is shifted to slightly lower wavenumbers at 3745 cm⁻¹. A second negative peak at 3669 cm⁻¹

¹ due to P-OH functionalities is again observed in the high wavenumber region. The peaks in the 3200 – 3000 cm^{-1} region are again present on a rising background and are shifted to slightly higher wavenumbers. In the low wavenumber region several new peaks are present at 1638, 1607 and 1547 cm^{-1} and a strong new feature at 1491 cm^{-1} . The peaks obtained on SiO_2 are shifted to higher wavenumbers at 1595, 1576 and 1447 cm^{-1} . The intensities of all features decrease as the temperature is increased up to 523 K.

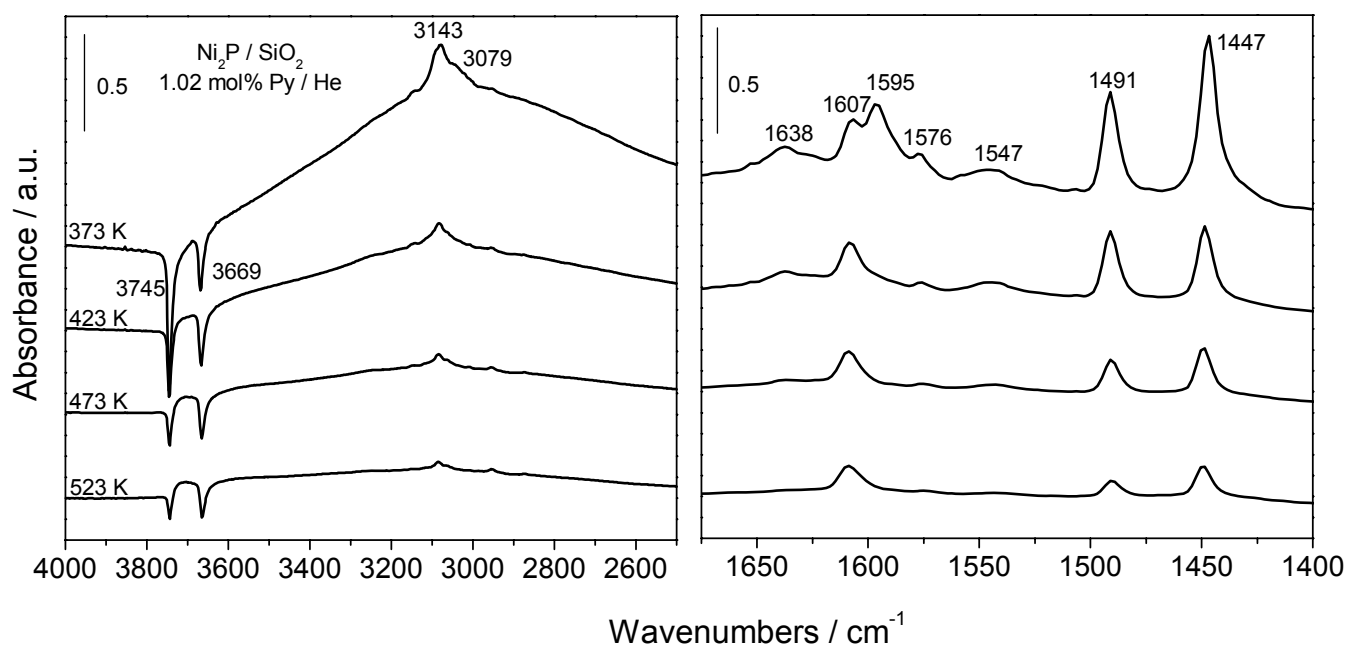


Figure 3.8. FTIR spectra of pyridine adsorbed on $\text{Ni}_2\text{P}/\text{SiO}_2$ in He flow as a function of temperature

Figure 3.9 shows the FTIR spectra of pyridine adsorbed on $\text{Ni}_2\text{P}/\text{SiO}_2$ under H_2 flow after degassing. The main spectral features are located at 3745, 3669, 3143, 3079, 2984, 2951, 2872, 1638, 1607, 1597, 1578, 1559, 1542, 1491 and 1447 cm^{-1} . The spectra are very similar to those obtained under He flow. In the high wavenumber region the

intensity of the negative peak at 3669 cm^{-1} is slightly attenuated and several new peaks appear at 2984 , 2951 and 2872 cm^{-1} . Again, the intensities of all peaks decrease with increasing temperature. At higher temperatures, a shoulder on the peak at 1491 cm^{-1} becomes visible at approximately 1481 cm^{-1} . This peak remains at 523 K , while the peak at 1491 cm^{-1} is greatly reduced in intensity.

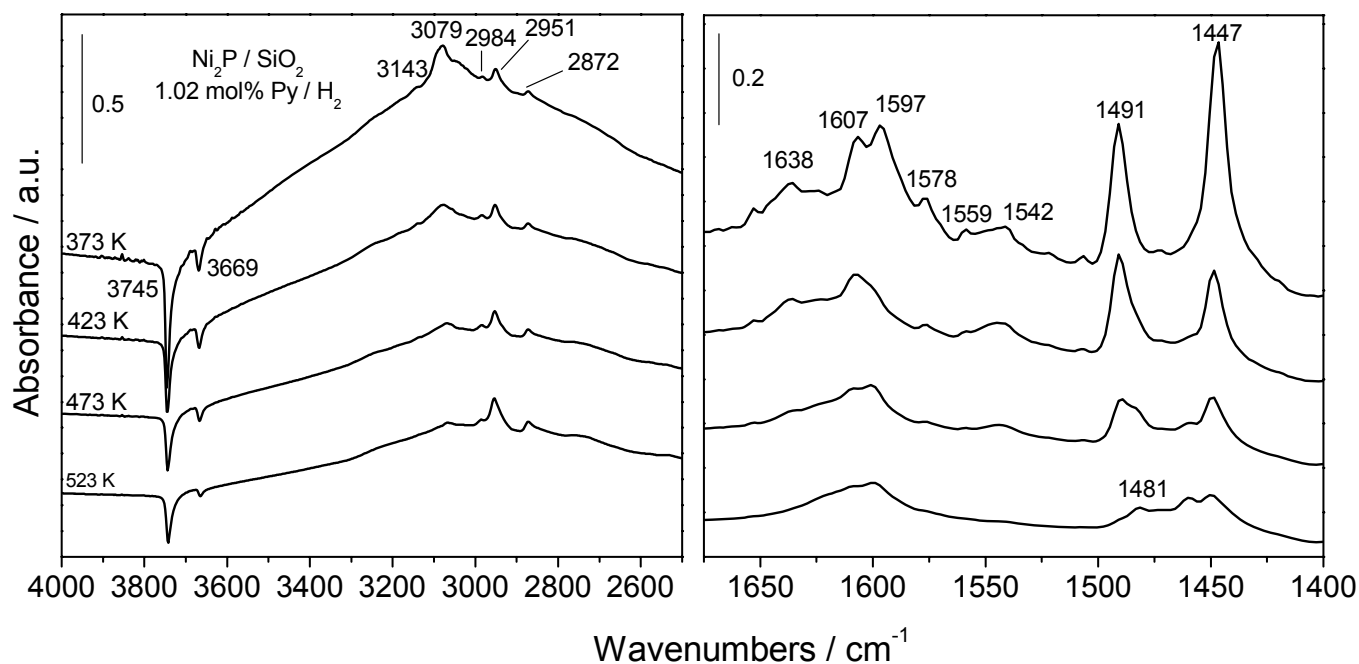


Figure 3.9. FTIR spectra of pyridine adsorbed on $\text{Ni}_2\text{P}/\text{SiO}_2$ in H_2 flow as a function of temperature

In situ transient kinetic experiments were conducted on the $\text{Ni}_2\text{P}/\text{SiO}_2$ catalyst at 423 K using several concentrations of pyridine. The kinetic experiments were performed in both He and H_2 flow in order to separately measure the net rates of adsorption and the rates of reaction. For all experiments, the evolution of the peak at 1491 cm^{-1} was tracked over time. This peak, representing pyridine on Brønsted and Lewis acid sites, was

chosen because it is well resolved from other spectral features, not present in the spectrum of gas-phase pyridine and has no contribution from pyridine physisorbed on the active phase or SiO₂ support. Figure 3.10 a) represents the time-resolved spectra for the adsorption of 0.85 mol% pyridine in He carrier on Ni₂P/SiO₂ at 423 K. As soon as pyridine was introduced, the intensity and area of the peak at 1491 cm⁻¹ increased rapidly and reached a steady value after ~ 200 s. Figure 3.10 b) represents the time-resolved spectra for the adsorption and reaction of 0.85 mol% pyridine in H₂ carrier. Again, the peak at 1491 cm⁻¹ grew rapidly although with lower intensity and area. Under continuous pyridine/H₂ flow, a second well-resolved peak at 1481 cm⁻¹ also developed with increasing time but with relatively lower intensity and area. At higher temperatures, this peak appeared as a shoulder (Figure 3.9) in the adsorption experiments performed in a H₂ atmosphere. The intensity of the feature at 1491 cm⁻¹ again reached a steady value after ~ 200 s while the intensity of the peak at 1481 cm⁻¹ reached a steady value in a shorter time of < 100 s. As will be discussed, the species giving rise to the feature at 1491 cm⁻¹ (pyridinium ion on Brønsted and Lewis acid centers) is not a reactive intermediate in the system. The species associated with the peak at 1481 cm⁻¹ may be an actual intermediate in the reaction.

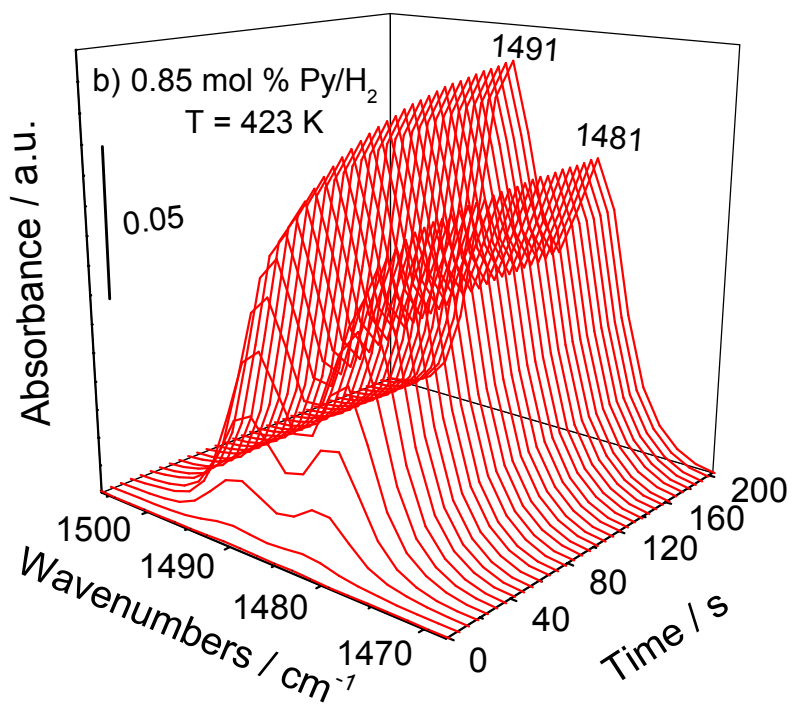
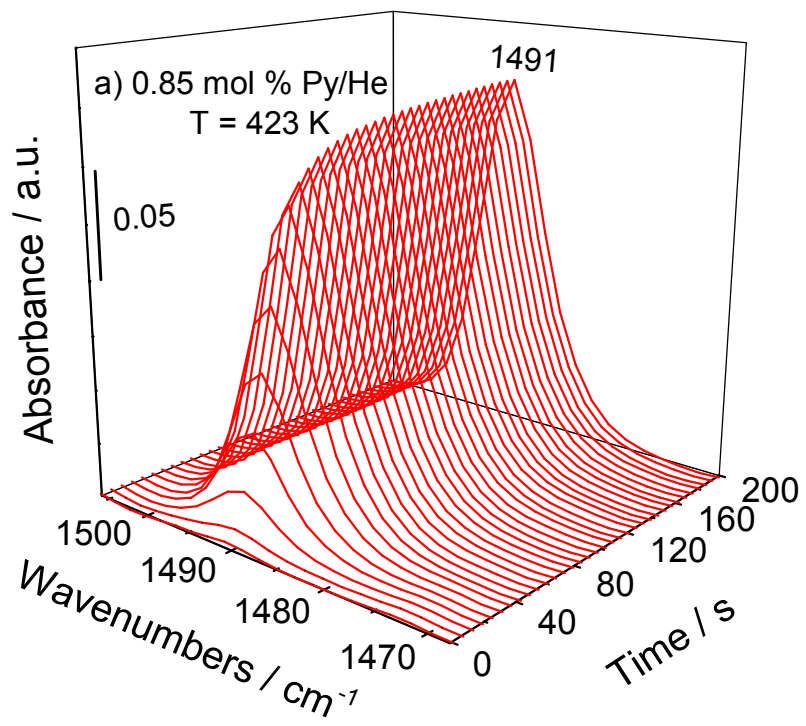
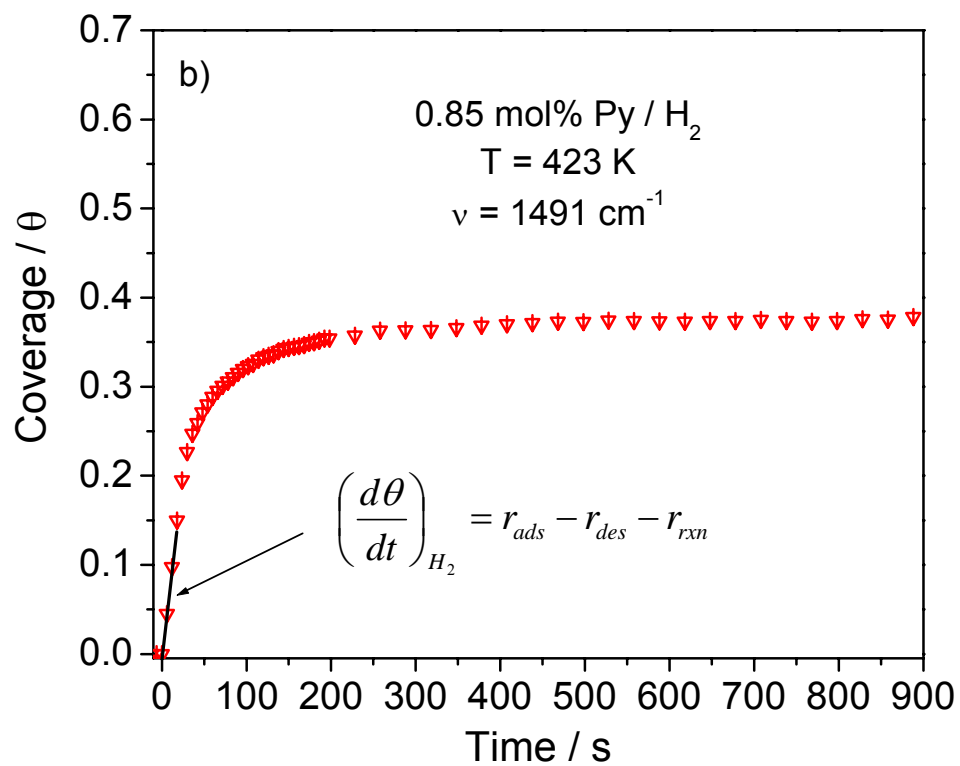
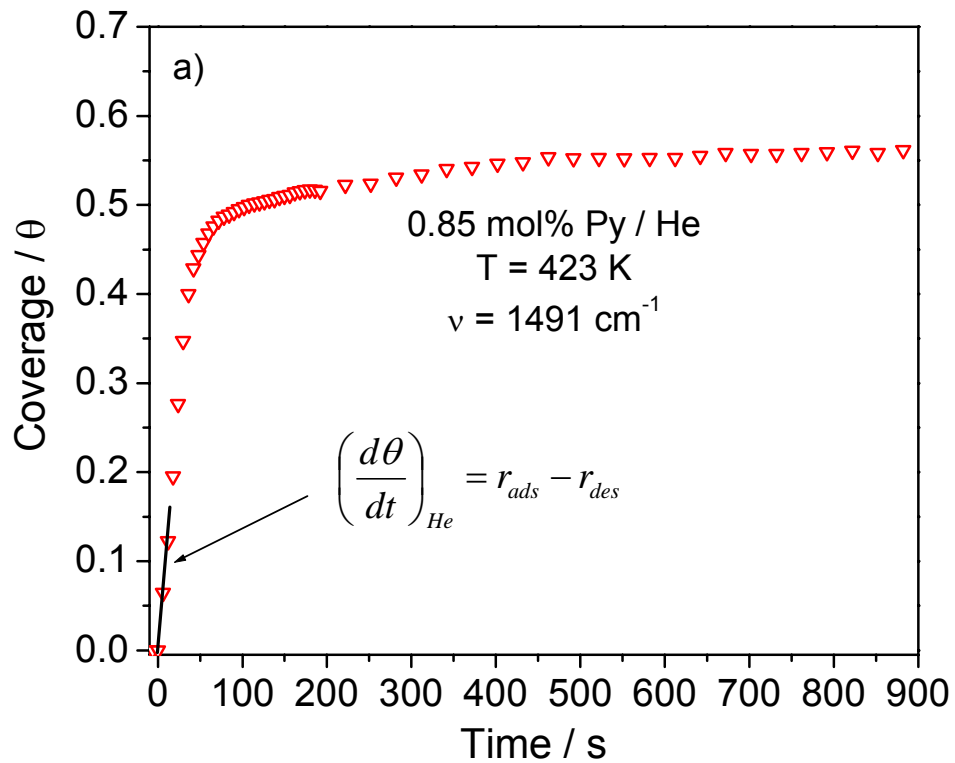


Figure 3.10. Time-resolved FTIR spectra of 0.85 mol% pyridine adsorbed on $\text{Ni}_2\text{P}/\text{SiO}_2$

a) He carrier at 423 K, b) H₂ carrier at 423 K

The peak centered at 1491 cm⁻¹ was fit with peak-fitting software (Origin 6.1) using a Gaussian curve. Furthermore, the overlapping peaks acquired under H₂ flow were deconvoluted using a multipeak fitting algorithm available with the software. In all cases, the positions of the peaks and their full widths at half maximum were kept constant while other fitting parameters were allowed to vary in the fitting algorithm. The areas of the peak located at 1491 cm⁻¹ were converted to fractional coverage as described previously. Figure 3.11 presents the evolution of pyridine coverage with respect to time for the addition of 0.85 mol% pyridine in He or H₂ carrier at 423 K. As can be seen, pyridine was introduced to the reactor at time zero and the coverages of pyridine quickly increased to a steady value in ~ 200 s under both carrier gases. As a note, coverage values are shown in 6 s increments in the transient region of the coverage curve (< 200 s) and at 30 s intervals thereafter. In He carrier (Figure 3.11 a)), the coverage of pyridine reached a steady-state value of 0.56. As expected, because of the occurrence of reaction, the steady-state coverage of pyridine in H₂ carrier (Figure 3.11 b)) was lower and reached a value of 0.38. At all concentrations used in the study, the steady-state coverage of pyridine on Ni₂P/SiO₂ was lower in reactive H₂ carrier than in inert He carrier gas because of reaction of pyridine.



**Figure 3.11. Example of transient kinetic analysis for pyridine adsorption on
Ni₂P/SiO₂**

a) He carrier at 423 K, b) H₂ carrier at 423 K

The transient coverage versus time curves were used to obtain net adsorption and reaction rates. Rates were determined by differentiation of the curves at each point and extrapolating the slopes ($d\theta/dt$) in the transient regions to time zero ($\theta \rightarrow 0$). The derivative is the change in coverage with time and represents a turnover frequency (s^{-1}). An example of this method is shown in Figure 3.11 a) which shows the evolution of pyridine coverage as a function of time for pyridine adsorption (0.85 mol%) in He carrier at 423 K. The slope of the coverage versus time curve is equal to the net rate of adsorption, that is, the rate of pyridine adsorption (r_{ads}) minus the rate of pyridine desorption (r_{des}). The rate of adsorption is proportional to the number of empty sites and the rate of desorption is proportional to the number of occupied sites. As a result, the rate of adsorption decreases with increasing coverage while the rate of desorption increases. At steady-state these rates are equilibrated and the apparent net rate of adsorption is zero. Figure 11b) shows the analogous method used for pyridine adsorption (0.85 mol%) in H₂ carrier at 423 K. The slope of the coverage versus time curve now represents the rate of pyridine adsorption (r_{ads}) minus the rate of pyridine desorption (r_{des}) minus the rate of pyridine reaction (r_{rxn}). The same procedure was followed for all pyridine feed concentrations.

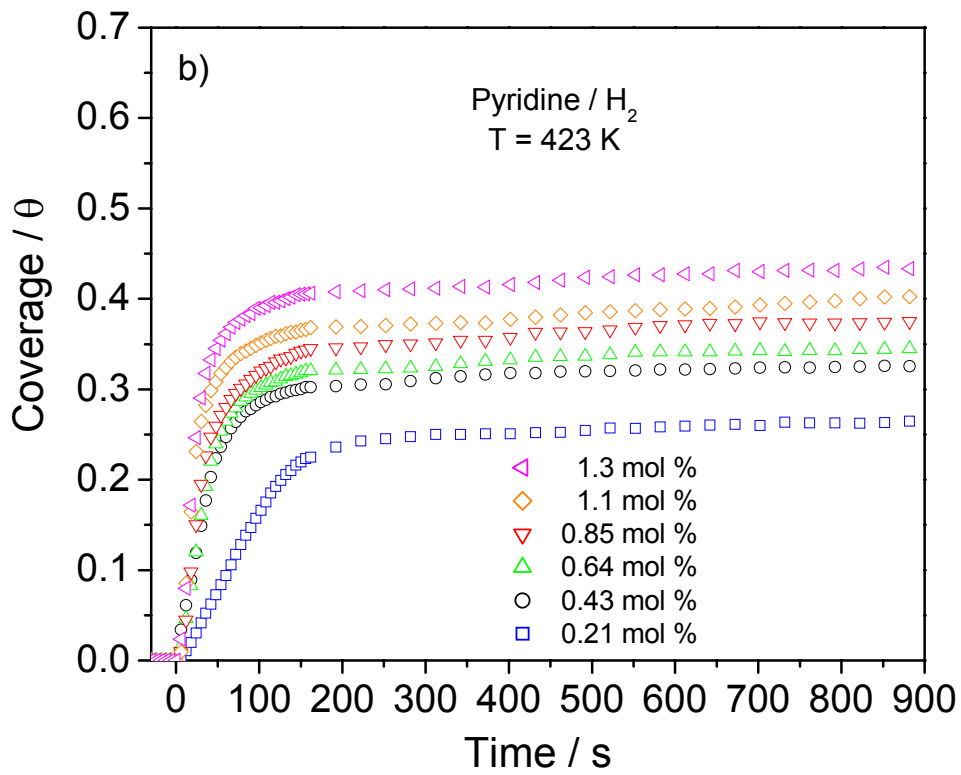
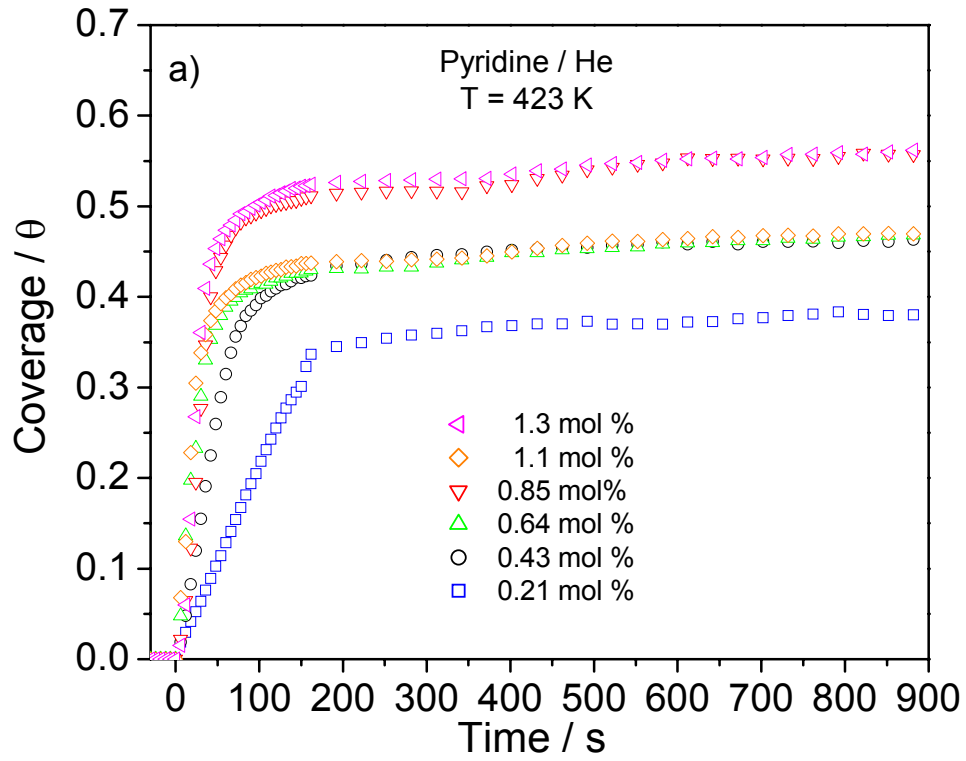


**Figure 3.12. Transient additions of pyridine at several concentrations over
Ni₂P/SiO₂**

a) He carrier at 423 K, b) H₂ carrier at 423 K

Figure 3.12 a) shows the adsorption of pyridine at several concentrations in He on the Ni₂P/SiO₂ catalyst at 423 K. At all concentrations, the coverages of adsorbed pyridine rapidly increased with the introduction of pyridine at time zero and reached steady-state values in ~ 200 s. The steady-state coverages were 0.38, 0.47 and 0.56 for pyridine concentrations of 0.21, 0.64 and 1.3 mol%, respectively. Figure 3.12 b) shows the adsorption of pyridine at several concentrations in H₂ carrier on the Ni₂P/SiO₂ catalyst at 423 K. At all concentrations, the coverages of adsorbed pyridine rapidly increased with the introduction of pyridine at time zero and reached steady-state values in ~ 200 s. The steady-state coverages were 0.26, 0.35 and 0.43 for pyridine concentrations of 0.21, 0.64 and 1.3 mol%, respectively.

Once the rates in He, $(d\theta/dt)_{\text{He}}$, and the rates in H₂, $(d\theta/dt)_{\text{H}_2}$, were obtained as described in Figure 3.11 for all the pyridine concentrations shown in Figure 3.12, the rate of reaction of pyridine was calculated by subtraction of the independently determined rates. That is, $(d\theta/dt)_{\text{He}} - (d\theta/dt)_{\text{H}_2} = r_{\text{rxn}}$. Figure 3.13 presents the results for the rates measured in He and H₂ and their differences, the turnover frequencies of the adsorbed pyridine species. As shown, the measured rates in both He and H₂ carriers increased linearly with increasing pyridine concentration and decreasing weight time. Moreover, the rates measured in H₂ carrier were lower at all concentrations and weight times, as discussed previously. As the pyridine concentration was increased the differences

between the rates measured independently in He and H₂ also increased, giving rise to a steadily increasing reaction rate of pyridine. The turnover frequency trend was linear with increasing pyridine concentration, indicating first-order reaction. However, over the range of concentrations studied the rates of pyridine reaction were low.

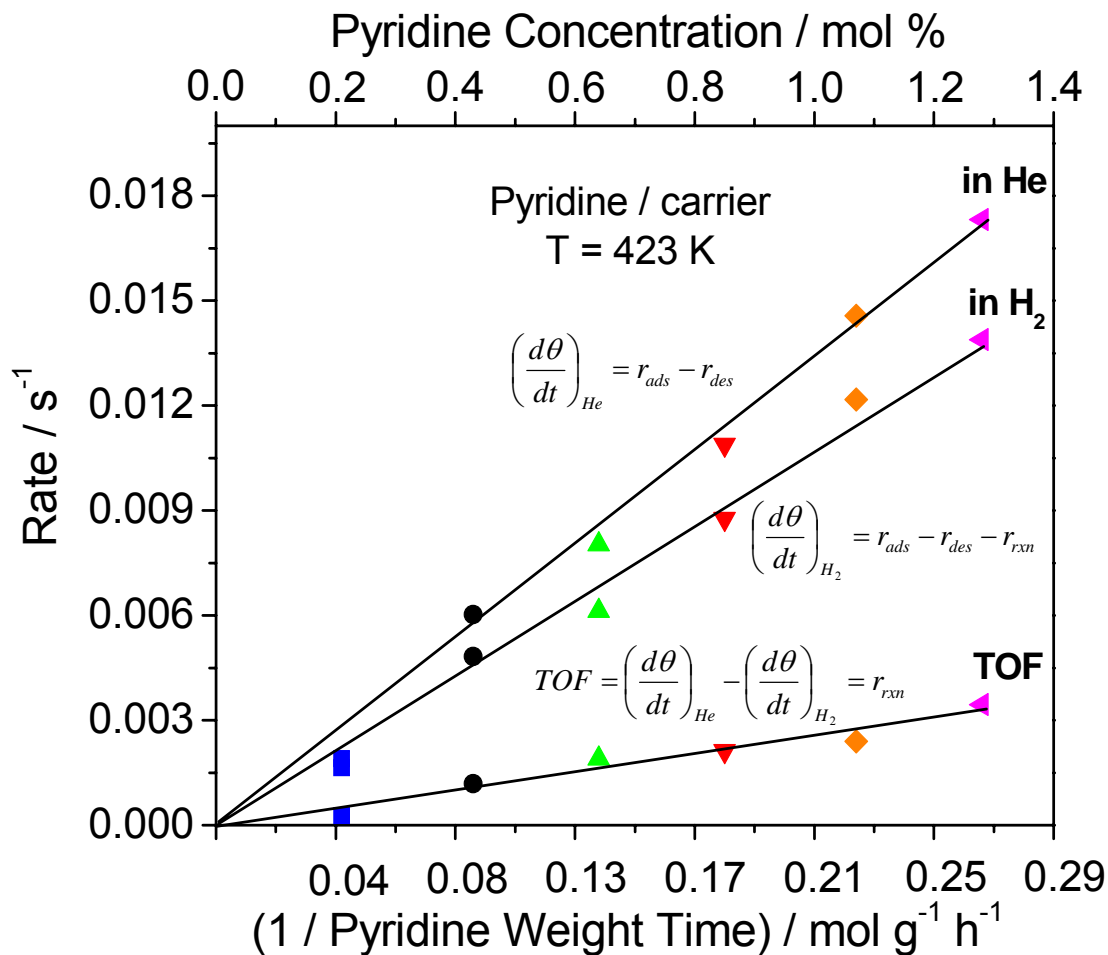


Figure 3.13. Transient kinetic results for pyridine reaction on Ni₂P/SiO₂ at 423 K

3.3.4. Steady-State Rate Measurements

In order to determine if the adsorbed pyridinium species is a true reaction intermediate, pyridine turnover frequencies were measured at several weight times (Table 3.2) under steady-state conditions at 423 K and atmospheric pressure. Determination of the kinetic role of an adsorbed intermediate to the overall catalyzed reaction requires comparison between rates measured under both transient and steady-state conditions. Table 3.4 presents the results of the reaction of pyridine over Ni₂P/SiO₂ under steady-state conditions. As expected, the pyridine conversion decreased with decreasing weight time (increasing flow rate). Additionally, the major product observed at all weight times was piperidine. At the highest weight time, a small amount of HDN products were observed. This indicates that further reaction of piperidine was relatively slow at 423 K and atmospheric pressure. Equation 6 was used to calculate pyridine turnover frequencies at each weight time. Figure 3.14 shows the pyridine turnover frequencies measured in the similar range of pyridine weight time used in the transient experiments. As can be seen, the overall turnover frequency of pyridine increased linearly with decreasing weight time. Although displaying the same trend, the rates measured under steady-state conditions were observed to be two orders of magnitude higher than those measured under transient conditions.

Table 3.4.

Steady-state pyridine reaction results at 423 K

Pyridine flow rate / $\mu\text{mol s}^{-1}$	Pyridine weight time / $\text{g}\cdot\text{h mol}^{-1}$	Conversion / %	Turnover frequency, TOF / s^{-1}	Piperidine selectivity / %
2.0	14	45	0.102	99
2.6	11	37	0.106	100
4.2	6.6	25	0.117	100
5.5	5.0	21	0.13	100

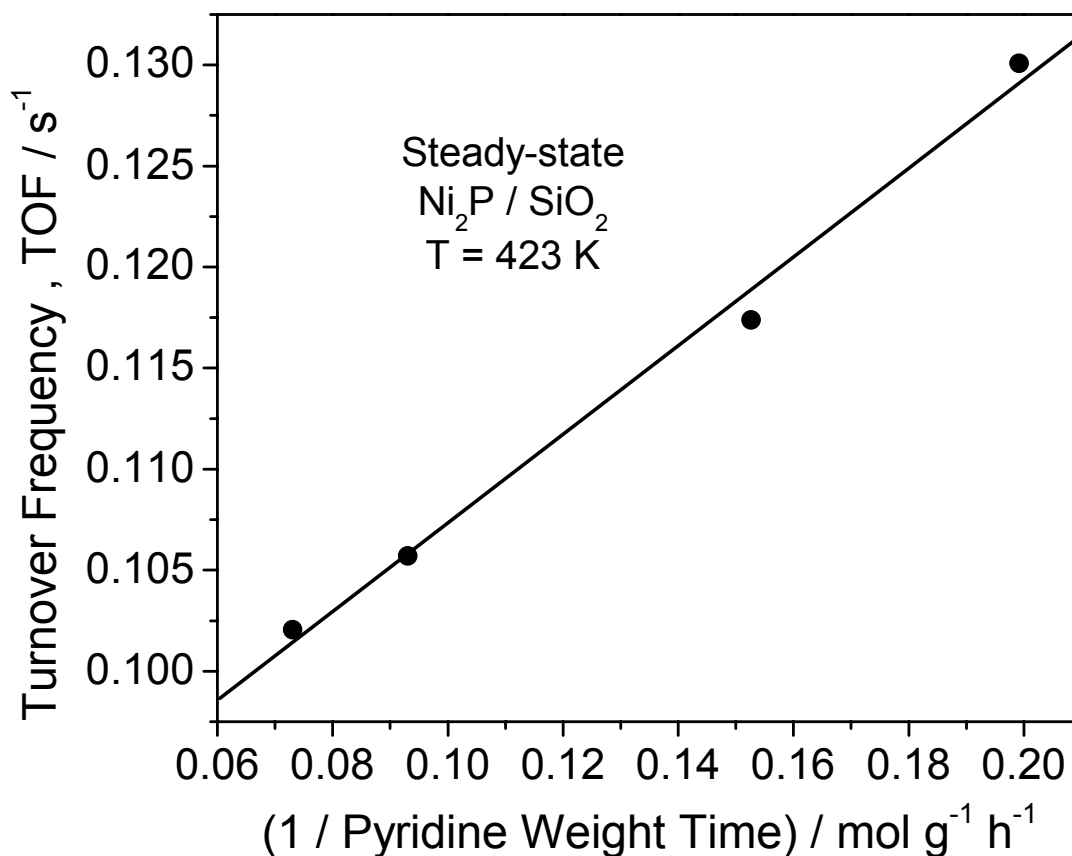


Figure 3.14. Steady-state kinetic results for pyridine reaction over $\text{Ni}_2\text{P}/\text{SiO}_2$ at 423 K and atmospheric pressure

It is concluded that the main species observed under reaction conditions, the pyridinium species on Brønsted and Lewis acid sites, is not the reactive intermediate in the reaction but a spectator that reacts at a much lower rate than the overall rate of reaction. An unidentified partially hydrogenated species with a characteristic $\nu_{\text{CC(N)}}$ band at 1481 cm^{-1} and aliphatic ν_{CH} bands at 2957 and 2874 cm^{-1} is a likely intermediate. The species was not observed under He flow but was formed upon adsorption of pyridine on Ni_2P in reactive H_2 . Hydrogenation of pyridine likely occurs on Lewis acid sites as reaction of pyridine and formation of the partially hydrogenated intermediate results in attenuation of the peaks located at 1607 , 1491 and 1447 cm^{-1} . This is in agreement with the work of Marzari and coworkers [52] who studied the HDN of pyridine at atmospheric pressure over several supported Mo oxides with varying Lewis and Brønsted acidities. They determined that the overall HDN activity was correlated with the concentration of *cus* Mo sites which are active for hydrogenation, and reaction of pyridine to piperidine was rate-limiting.

One possible explanation for the slow conversion of the pyridinium species and the formation of a partially hydrogenated surface intermediate is the mode of pyridine adsorption under the reaction conditions employed. Pyridine can adsorb to the catalyst surface via the nitrogen atom's electron pair (end-on mode) or through the π electrons of the aromatic ring (side-on mode) [14]. It has been proposed that ring hydrogenation occurs through side-on adsorption while C—N bond cleavage takes place through the end-on mode [53]. Al-Megren and coworkers [54,55] studied the HDN of pyridine over transition metal carbides, oxides, nitrides and sulfides over a wide temperature range and determined from product distributions and selectivities that the end-on mode is favorable

at low temperatures while the side-on adsorption mode is favorable at higher temperatures. From our results, it can be suggested that at the low reaction temperature (423 K) the observed pyridinium species corresponds to pyridine adsorbed in the end-on mode. As a result, further reaction of adsorbed pyridine in this mode is extremely slow and is only a spectator in the overall HDN reaction. Adkins and coworkers studied the hydrogenation of pyridine and 2,6-dimethylpyridine over Raney nickel and observed a higher hydrogenation rate for 2,6-dimethylpyridine. The observations were ascribed to a steric effect by which 2,6-dimethylpyridine was adsorbed to the catalyst surface via a surface π -complex. The unhindered pyridine molecule was assumed to adsorb through the sp^2 lone electron pair in the end-on mode. The side-on adsorption was proposed to be favorable for hydrogenation [56]. It is important to note that, under our experimental conditions, $P_{H_2} = 1$ atm and $T = 423$ K, the hydrogenation reaction of pyridine to piperidine is not limited by thermodynamics. The thermodynamic equilibrium equation [57] indicates that equilibrium lies well to the right:

$$\ln K = \frac{23470}{T} - 46.06 + 3 \ln \left(\frac{P_{H_2}}{P^o} \right) \quad (7)$$

where $K = [\text{piperidine}] / [\text{pyridine}]$, T [=] K and $P^o = 1$ atm. The value of K is 1.24×10^4 . Thus, the pyridine-piperidine equilibrium is completely on the piperidine side.

The true reaction intermediate likely arises via pyridine adsorbed in the side-on arrangement, as this mode is more favorable for hydrogenation of the aromatic ring. Analogous to the hydrogenation of aromatics on metals, it is generally believed that hydrogenation of nitrogen heterocycles proceeds with the ring parallel to the surface via formation of a surface π -adsorbed intermediate. Electrons in d-orbitals of the Ni atoms are available for π -back bonding into the empty antibonding π -molecular orbitals of

pyridine, thus destroying the aromaticity of the molecule and activating it for hydrogenation [58]. The appearance of a partially hydrogenated species on the Ni₂P surface instead of the fully saturated intermediate piperidine is understandable since hydrogenation reactions of aromatics are known to be slow at low temperatures and H₂ pressures [59]. Furthermore, accumulation of the partially hydrogenated intermediate on the catalyst surface can be explained by strong adsorption and the absence of H₂S in the feed. The partially saturated and fully saturated intermediates formed after hydrogenation are more strongly basic than the unsaturated reactant [60]. As a result, they are strongly held on the surface of the Ni₂P catalyst. The absence of H₂S in the feed, which is known to promote ring-opening by addition to the C=N bond [21] or by a classic organic mechanism [61], probably diminishes further reaction of the adsorbed intermediate. Unfortunately, the same analysis as done for the pyridinium ion cannot be carried out with this species because it is not observed in experiments conducted under He flow.

To summarize, an adsorbed pyridinium species was identified on the surface of Ni₂P/SiO₂ at reaction conditions. The species behaved as a reactive intermediate, as its concentration increased with increasing pyridine partial pressure and decreased with exposure to hydrogen. However, a study of the kinetics of its reaction using transient experiments showed that it reacted at a rate about 100 times slower than the steady-state reaction. This indicated that it was not a true reaction intermediate, but a spectator on the surface. The studies here demonstrate the danger of carrying out spectroscopic measurements of surface species without doing dynamic experiments to verify that they are capable of reacting at rates consistent with catalytic rates.

3.4. Conclusions

The steady-state and transient reactivity of pyridine over Ni₂P/SiO₂ was studied at 423 K and atmospheric pressure. FTIR experiments were used to identify a pyridinium intermediate with characteristic bands at 1607, 1491 and 1446 cm⁻¹ on the Ni₂P surface under He flow. Upon switching the carrier flow to H₂, a second band at 1481 cm⁻¹ was identified and assigned to a partially hydrogenated reaction intermediate. Transient kinetic experiments, conducted under both He and H₂ flow, were used to separately measure the net rate of adsorption and the rate of reaction of the species in order to determine the kinetic role of the pyridinium intermediate. Steady-state kinetic measurements were obtained at the same reaction conditions in order to compare the reaction rate of the pyridinium intermediate to the global reaction kinetics. However, the rates measured under steady-state conditions were two orders of magnitude higher than those obtained under transient conditions. It is concluded that the pyridinium species is a spectator in the HDN of pyridine and reacts at much lower rates than the overall reaction rate. Under the reaction conditions employed, pyridine is likely adsorbed to the catalyst surface through the nitrogen atom lone pair (end-on mode) through which hydrogenation is slow. The partially hydrogenated species observed under H₂ flow is a possible reaction intermediate in the HDN of pyridine.

References

- [1] H. Topsøe, B.S. Clausen, F.E. Massoth, *Hydrotreating Catalysis-Science and Technology*, Springer-Verlag, Berlin, 1996.
- [2] J.M. Thomas, W.J. Thomas, *Principles and Practice of Heterogeneous Catalysis*, VCH, New York, 1997.
- [3] C. Song, *Catal. Today* 86 (2003) 211.
- [4] J.R. Katzer, R. Sivasubramanian, *Catal. Rev. – Sci. Eng.* 20:2 (1979) 155.
- [5] P. Grange, *Catal. Rev. – Sci. Eng.* 21:1 (1980) 135.
- [6] F. van Looij, P. van der Laan, W.H.J. Stork, D.J. DiCamillo, J. Swain, *Appl. Catal., A* 170 (1998) 1.
- [7] S. Shin, H. Yang, K. Sakanishi, I. Mochida, D.A. Grudoski, J.H. Shinn, *Appl. Catal., A* 205 (2001) 101.
- [8] G.C. Laredo, E. Altamirano, J.A. De los Reyes, *Appl. Catal., A* 243 (2003) 207.
- [9] P. Zeuthen, K.G. Knudsen, D.D. Whitehurst, *Catal. Today* 65 (2001) 307.
- [10] U.T. Turaga, X. Ma, C. Song, *Catal. Today* 86 (2003) 265.
- [11] A. Logadóttir, P.G. Moses, B. Hinnemann, N.-Y. Topsøe, K.G. Knudsen, H. Topsøe, J.K. Nørskov, *Catal. Today* 111 (2006) 44.
- [12] N. Nelson, R.B. Levy, *J. Catal.* 58 (1979) 485.
- [13] G. Perot, *Catal. Today* 10 (1991) 447.
- [14] M.J. Ledoux, P.E. Puges, G. Maire, *J. Catal.* 76 (1982) 285.
- [15] J. Sonnemans, W.J. Neyens, P. Mars, *J. Catal.* 34 (1974) 230.
- [16] J. Sonnemans, P. Mars, *J. Catal.* 34 (1974) 215.
- [17] R. Prins, M. Jian, M. Flechsenhar, *Polyhedron* 16 (1997) 3235.

-
- [18] M. Jian, R. Prins, *J. Catal.* 179 (1998) 18.
- [19] I.I. Abu, K.J. Smith, *Catal. Today* 125 (2007) 248.
- [20] I.I. Abu, K.J. Smith, *Appl. Catal., A* 328 (2007) 58.
- [21] H. Wang, C. Liang, R. Prins, *J. Catal.* 251 (2007) 295.
- [22] M. Egorova, Y. Zhao, P. Kukula, R. Prins, *J. Catal.* 206 (2002) 263.
- [23] J.F. Cocchetto, C.N. Satterfield, *Ind. Eng. Chem. Process Des. Dev.* 15 (1976) 272.
- [24] J.F. Cocchetto, C.N. Satterfield, *Ind. Eng. Chem. Process Des. Dev.* 20 (1981) 49.
- [25] G.C. Hadjiloizou, J.B. Butt, J.S. Dranoff, *J. Catal.* 131 (1991) 545.
- [26] P. Clark, X. Wang, P. Deck, S.T. Oyama, *J. Catal.* 210 (2002) 116.
- [27] M. Cattenot, J.-L. Portefaix, J. Afonso, M. Breyse, M. Lacroix, G. Perot, *J. Catal.* 173 (1998) 366.
- [28] Y. Zhao, R. Prins, *J. Catal.* 222 (2004) 532.
- [29] Y. Zhao, P. Kukula, R. Prins, *J. Catal.* 221 (2004) 441.
- [30] S.T. Oyama, Y.-K. Lee, *J. Phys. Chem. B* 109 (2005) 2109.
- [31] R. Prins, Y. Zhao, N. Sivasankar, P. Kukula, *J. Catal.* 234 (2005) 509.
- [32] A. Platon, W.J. Thomson, *Ind. Eng. Chem. Res.* 42 (2003) 5988.
- [33] S. Damyanova, M.A. Centeno, L. Petrov, P. Grange, *Spectrochim. Acta, Part A* 57 (2001) 2495.
- [34] M.S. Rana, M.L. Huidobro, J. Ancheyta, M.T. Gómez, *Catal. Today* 107-108 (2005) 346.
- [35] F. Sánchez-Minero, J. Ramírez, A. Gutiérrez-Alejandre, C. Fernández-Vargas, P.

-
- Torres-Mancera, R. Cuevas-Garcia, *Catal. Today* 133-135 (2008) 267.
- [36] E.C. DeCanio, J.G. Weissman, *Colloids Surf., A* 105 (1995) 123.
- [37] T.I. Korányi, M. Dobrovolszky, T. Koltai, K. Matusek, Z. Paál, P. Tétényi, *Fuel Process. Technol.* 61 (1999) 55.
- [38] R.M. Navarro, P. Castaño, M.C. Álvarez-Galván, B. Pawelec, *Catal. Today* (2008) In press.
- [39] Y.-C. Park, E.-S. Oh, H.-K. Rhee, *Ind. Eng. Chem. Res.* 36 (1997) 5083.
- [40] Y.-K. Lee, S.T. Oyama, *J. Catal.* 239 (2006) 376.
- [41] S.T. Oyama, W. Li, *Top. Catal.* 8 (1999) 75.
- [42] X. Wang, P. Clark, S.T. Oyama, *J. Catal.* 208 (2002) 321.
- [43] S.T. Oyama, X. Wang, Y.-K. Lee, K. Bando, F.G. Requejo, *J. Catal.* 210 (2002) 207.
- [44] S.T. Oyama, X. Wang, Y.-K. Lee, W.-J. Chun, *J. Catal.* 221 (2004) 263.
- [45] C.L. Yaws, K.P. Narasimhan, C. Gabbula, *Yaws' Handbook of Antoine Coefficients for Vapor Pressure*, Knovel, 2005.
- [46] S. Rundqvist, *Acta Chem. Scand.* 16 (1962) 992.
- [47] *Powder Diffraction Data Files*, JCPDS International Center for Diffraction Data, Swathmore, PA, 1992.
- [48] M.I. Zaki, M.A. Hasan, F.A. Al-Sagheer, L. Pasupulety, *Colloids Surf., A* 190 (2001) 261.
- [49] A.P. Legrand, H. Hommel, A. Tuel, *Adv. Colloid Interface Sci.* 33 (1990) 91.
- [50] C. Morterra, G. Cerrato, *Langmuir* 6 (1990) 1810.
- [51] G. Socrates, *Infrared Characteristic Group Frequencies*, Wiley, New York, 1994.

-
- [52] J.A. Marzari, S. Rajagopal, R. Miranda, *J. Catal.* 156 (1995) 255.
- [53] C. Moreau, P Geneste, in: J.B. Moffat (ed.), *Theoretical Aspects of Heterogeneous Catalysis*, Van Nostrand Reinhold Catalysis Series, 1990, pg. 256.
- [54] H.A. Al-Megren, T. Xiao, S.L. Gonzalez-Cortes, S.H. Al-Knowaiter, M.L.H. Green, *J. Mol. Catal. A: Chem.* 225 (2005) 143.
- [55] H.A. Al-Megren, S.L. González-Cortés, T. Xiao, M.L.H. Green, *Appl. Catal., A* 329 (2007) 36.
- [56] H. Adkins, L.F. Kuick, M. Farlow, B. Wojcik, *J. Am. Chem. Soc.* 56 (1934) 2425.
- [57] W.V. Steele, R.D. Chirico, *Topical Report for the US Department of Energy*, IIT Research Institute, Bartlesville, Oklahoma, 1992.
- [58] T.C. Ho, *Catal. Rev. – Sci. Eng.*, 30(1) (1988) 117.
- [59] G.M. Loudon, *Organic chemistry*, 3rd Edition, Benjamin-Cummings, Redwood City, 1995, pg. 775.
- [60] M.-H. Yang, P. Grange, B. Delmon, *Appl. Catal., A* 154 (1997) L7-L15.
- [61] E. Furimsky, F.E. Massoth, *Catal. Rev. – Sci. Eng.* 47:3 (2005) 297.

Chapter 4

In Situ FTIR and XANES Studies of Thiophene Hydrodesulfurization on Ni₂P/MCM-41

4.1. Introduction

Recently, hydrodesulfurization (HDS), an industrial process used to remove sulfur from petroleum feedstocks has come to prominence because of world-wide legislation limiting the amount of sulfur in transportation fuels. Fourier transform infrared spectroscopy (FTIR) [1-5] and extended x-ray absorption fine-structure (EXAFS) [6-10] have been applied to the investigation of hydrotreating catalysts, but little work has been previously done on analysis of reaction mechanisms.

The catalyst used in this study is a novel material, Ni₂P/MCM-41. Transition metal phosphides are a new class of catalyst showing extremely high activity for HDS and hydrodenitrogenation reactions with better performance than commercial sulfide catalysts [11,12]. Among the phosphides, nickel phosphide has been found to be particularly active [13,14]. Previous in situ EXAFS studies of Ni₂P/SiO₂ showed the formation of stable clusters with surface Ni-S bonds during HDS [15,16]. In the case of Ni₂P/MCM-41, EXAFS has shown the formation of small Ni₂P clusters dispersed on the support, which expose primarily square-pyramidal sites [17].

Thiophene is often used as a model compound for the study of the mechanism and kinetics of HDS and is representative of typical refractory sulfur compounds in crude oil.

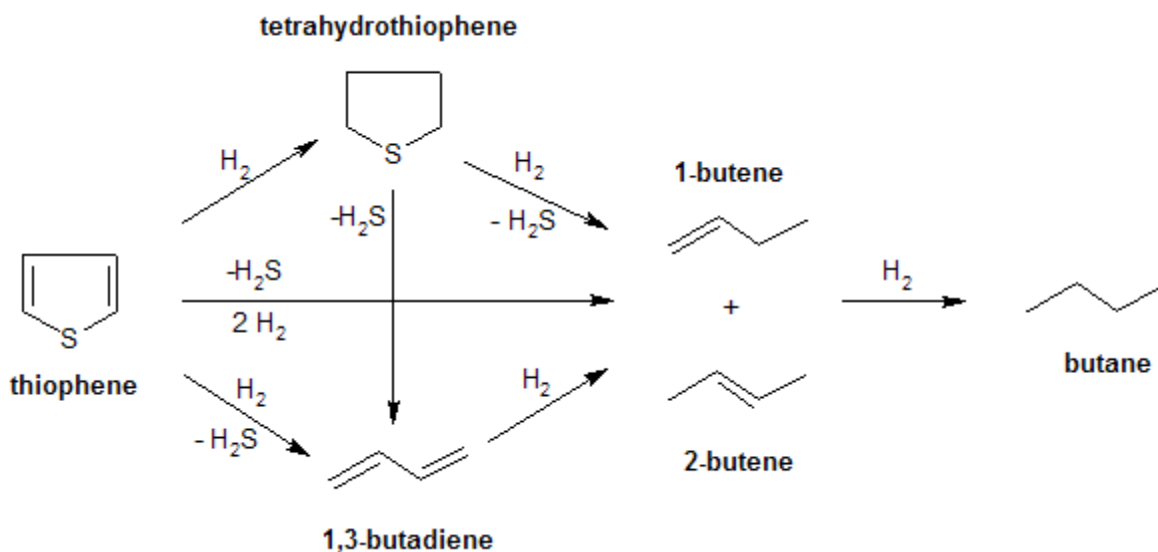
Examination of the bonding and reaction of thiophene on catalysts surfaces affords the opportunity to study the most important steps of HDS, namely hydrogenation, cleavage of C—S bonds and removal of sulfur as H₂S. However, the reaction mechanism for the HDS of thiophene remains a matter of great debate. From an extensive review of the literature, a global reaction network was proposed by Topsøe and workers as shown in Scheme 4.1 [18]. Similar to the HDS of larger S-containing compounds like 4,6-dimethyldibenzothiophene, both a direct C—S bond cleavage and a hydrogenation pathway with hydrogenation of one or both C=C bonds prior to C—S bond scission have been proposed [18-20].

Several studies on thiophene HDS have suggested that the major pathway is direct hydrogenolysis of C—S bonds to form 1,3-butadiene, which is subsequently hydrogenated to butenes and butane [21,22]. A concerted mechanism in which thiophene is directly desulfurized to butenes has also been proposed. The authors concluded that C—S bond cleavage and hydrogenation occurred on the same site and intermediates (diene) reacted faster than they desorbed [23]. However, direct cleavage of C—S bonds is difficult due to the stability of the heterocyclic aromatic ring. As a result, full or partial hydrogenation of the heterocyclic ring has been considered necessary before C—S bond cleavage [18,24].

Many other studies have advocated hydrogenation of the aromatic heterocyclic ring to form tetrahydrothiophene prior to C—S bond cleavage [18,25,26]. Tetrahydrothiophene can then be desulfurized by transfer of β -hydrogens to the sulfur atom with concomitant cleavage of C—S bond to yield 1,3-butadiene [27]. Butadiene is subsequently hydrogenated to butenes. Conversely, direct ring opening and removal of sulfur from tetrahydrothiophene by classic organic mechanisms (S_N2 and/or E2) may also be possible. Moser and coworkers have shown that butenes could also be formed by the decomposition of tetrahydrothiophene and not only via

hydrogenation of 1,3-butadiene. The authors proposed a ring opening mechanism of tetrahydrothiophene by β -hydrogen elimination to form a surface butene thiolate intermediate. Further reaction of the intermediate included rapid C—S bond hydrogenolysis to yield butenes or a slow second β -hydrogen elimination leading to 1,3-butadiene formation [28]. Under atmospheric pressure, however, tetrahydrothiophene is typically not observed as a reaction intermediate [29].

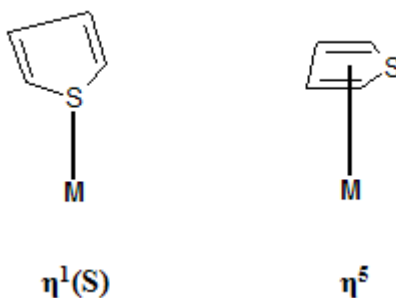
Partially hydrogenated thiophene molecules such as 2,3-dihydrothiophene (2,3-DHT) and 2,5-dihydrothiophene (2,5-DHT) have also been proposed as possible intermediates [24,30,31]. Several studies have observed the formation of these intermediates at low pressures during the HDS of thiophene. Hensen and coworkers [26] studied the HDS of thiophene over carbon-supported transition metal sulfides at atmospheric pressure and observed the formation of 2,3-DHT. The 2,3-DHT intermediate was found to undergo further reaction by desulfurization, isomerization to 2,5-DHT or rapid hydrogenation to tetrahydrothiophene. The authors concluded that the yield of the partially hydrogenated intermediates depended on the HDS activity of the catalyst – low activity catalysts gave rise to large amounts while catalysts with high HDS activities yielded very small amounts. Several theoretical studies have also shown that formation of dihydrothiophene intermediates is probable prior to C—S bond cleavage [32,33].



Scheme 4.1. Simplified thiophene HDS reaction network

As can be seen, several pathways for removal of sulfur from thiophene likely coexist. In addition, both surface reaction and hydrogenative removal of sulfur have been proposed to be rate-determining [34]. The governing reaction pathway and rate-controlling step depends on the catalyst, temperature and H_2 pressure [18,29]. The mode of thiophene adsorption has also been covered extensively in the literature and several modes have been proposed from studies of thiophene bonding in organometallic complexes [35,36]. Scheme 4.2 illustrates the generally accepted adsorption modes of thiophene to metal sites on the surface of hydrotreating catalysts – σ -bonded thiophene through the sulfur atom (upright, $\eta^1(S)$) and π -bonded thiophene (parallel, η^5) [37]. However, the mode of adsorption that activates thiophene towards further reaction is unclear [38]. Several studies have provided evidence of both σ - [39] and π -bound [40] thiophene as possible precursors. In addition, the mode of adsorption has been suggested to be coverage dependent. In several single crystal experiments the preferred mode was thought to be flatwise at low coverages while at higher coverages thiophene bonding is upright via a σ -bond between

the sulfur atom and a metal center [41,42]. Other single crystal work has shown that the mode of adsorption is coverage independent [43].



Scheme 4.2. Proposed thiophene bonding modes

Directly monitoring the surface coverage of an adsorbed surface species during adsorption and reaction is a powerful tool for elucidating kinetic and mechanistic information [44]. Such studies involve measuring the rates of adsorption and reaction under transient conditions and comparing the transient rates with the overall reaction rate measured under steady-state conditions. Agreement between the separately measured rates constitutes proof that the observed intermediate is a true reaction intermediate and is kinetically significant in the global mechanism. The present study will employ in situ FTIR of adsorption and reaction of thiophene over $\text{Ni}_2\text{P}/\text{MCM-41}$ to probe the bonding mode of thiophene and products formed during HDS at atmospheric pressure over a range of temperatures. Moreover, in situ, time-resolved analysis of XANES features (Ni K-edge) during adsorption and reaction of thiophene will be monitored to investigate the interaction of thiophene with the catalyst surface. Changes in the intensity of a pre-edge feature below the adsorption edge that correlates with the local coordination chemistry around the absorbing atom is followed [45]. A novel method to estimate the reaction rate of the adsorbed thiophene species under transient conditions using the above method is presented.

4.2. Experimental Section

4.2.1. Synthesis and Characterization

The support used in this study was siliceous MCM-41 and SiO₂ (Cabosil, EH-5 Grade). The mesoporous MCM-41 silica support was synthesized following a literature procedure [46]. The chemical used in the synthesis were colloidal silica (Fluka, HS-40), cetyltrimethylammonium bromide (CTMABr, Aldrich, 99%) and tetramethylammonium hydroxide (TMAOH, Aldrich, 25 wt% aqueous solution). The CTMABr and TMAOH were added to deionized water with stirring at 300 K until the solution became transparent, then the colloidal silica was added to the solution with stirring for 1 h and the resulting reaction gel was aged for 24 h at 323 K. The molar composition was 1.0 SiO₂ : 0.27 CTMABr : 0.19 TMAOH : 40 H₂O. After ageing, the mixture was reacted for 48 h at 393 K in a Teflon-lined stainless steel autoclave. The product was filtered, washed with distilled water, dried in air at 393 K, and finally calcined at 623 K for 8 h. The catalyst precursors were nickel nitrate hexahydrate, Ni(NO₃)₂·6H₂O (Alfa Aesar, 99%), and ammonium hydrogen phosphate, (NH₄)₂HPO₄ (Aldrich, 99%). Thiophene (Aldrich, 99%) was used in the study of hydrodesulfurization over the supported Ni₂P catalysts. All chemicals were used as received. The gases employed were He (Airgas, UPC grade), H₂ (Airgas, UPC grade), N₂ (Airgas, UPC grade) and CO (Airgas, Linde Research Grade, 99.97%). The gases were passed through two-stage gas purifiers (Alltech, model 4658) to remove moisture and oxygen. Additionally, 0.5% O₂/He (Airgas, UHP), which was used for passivation of reduced samples, was passed through a purifier to remove moisture.

The supported Ni₂P catalyst was prepared with excess phosphorus (Ni/P = 1/2) and a metal loading of 1.15 mmol Ni g⁻¹_{support} (12.2 wt.% Ni₂P/support). The synthesis of the

supported catalyst involved two steps. Briefly, in the first step, a supported nickel phosphate was prepared by incipient wetness impregnation of nickel and phosphorus precursors, followed by drying and calcination in static air. In the second step, the phosphate was reduced to phosphide in flowing H₂ by temperature-programmed reduction (TPR). The synthesis of MCM-41-supported Ni₂P is presented below as an example.

Prior to use, the MCM-41 was dried at 393 K for 3 h and calcined at 813 K for 7 h. The incipient wetness point of the MCM-41 was found to be 2.0 cm³ g⁻¹. In the first step, 2.13 g (16.1 mmol) of (NH₄)₂HPO₄ was dissolved in 5 cm³ of distilled water in a graduated cylinder to form a transparent colorless solution. Subsequently, 2.34 g (8.05 mmol) of Ni(NO₃)₂·6H₂O was added to yield a lightly-colored mixture with some precipitate. Several drops of concentrated HNO₃ were added to dissolve the precipitate and the solution was further diluted to a total volume of 14 cm³, resulting in a transparent green solution. The precursor solution was then impregnated on 7 g of MCM-41. After the impregnation, the powder was dried at 393 K for 6 h and calcined at 673 K for 4 h. The calcined material was ground with a mortar and pestle, pelletized with a press (Carver, Model C) and crushed and sieved to a particle diameter of 650-1180 μm (16/20 mesh). The supported nickel phosphate was reduced by TPR in a U-shaped quartz reactor heated by a furnace controlled by a temperature programmer (Omega Model CN 2000). The temperature was monitored by an embedded chromel-alumel thermocouple placed near the center of the reactor bed. The H₂ flow rate was set at 1000 cm³ (NTP) min⁻¹ per g of sample. A portion of the gas effluent was sampled through a leak valve into a mass spectrometer (Ametek/Dycor Model MA100) and the masses 2 (H₂), 4 (He), 18 (H₂O), 28 (N₂), 31 (P) and 34 (PH₃) were monitored. The mass signals and the reactor temperature were monitored in real-time by an online computer. After the temperature program, the sample was cooled to room

temperature in flowing He and passivated in a flow of 0.5 % O₂/He for 4 h to prevent rapid oxidation of the freshly reduced phosphide.

The supported Ni₂P catalyst and blank MCM-41 support was characterized by BET surface area measurements, CO chemisorption, powder X-ray diffractometry (XRD) and in situ Fourier transform infrared (FTIR) spectroscopy of adsorbed thiophene. A Micromeritics ASAP 2010 volumetric adsorption unit was used to measure the specific surface area of the samples from the linear portion of BET plots ($P/P_0 = 0.02 - 0.10$) at 77 K. Before the measurements, the samples were degassed for 8 h at 413 K. X-ray diffraction patterns of the catalyst samples and blank supports were acquired using a Scintag XDS-2000 powder diffractometer operated at 45 kV and 40 mA with Cu-K_α monochromatized radiation ($\lambda = 0.1542$ nm).

Irreversible CO uptake measurements were used to titrate the surface metal atoms and provide an estimate of the active sites on the catalysts. The CO chemisorption amounts were obtained by pulsing calibrated volumes of CO into a He carrier and measuring the decrease in peak areas caused by adsorption. The measurements were conducted using a standard flow system equipped with a computer-interfaced mass spectrometer. Before the measurements, 0.3 g of passivated sample was placed in a U-shaped quartz reactor and rereduced in flowing H₂ (300 cm³ (NTP) min⁻¹) at 803 K for 2 h. After the pretreatment, the sample was cooled to room temperature under He at a flow rate of 100 cm³ (NTP) min⁻¹. Metered pulses of CO (19.6 μmol) were passed over the sample to measure the total dynamic uptake.

4.2.2. In situ FTIR Measurements

Transmission infrared spectra of thiophene adsorbed on Ni₂P/MCM-41 and the blank support were collected with a combined in situ reactor-spectrometer system (Figure 4.1). Fourier

transform infrared (FTIR) spectra were collected with a Digilab Excalibur Series FTS 3000 spectrometer equipped with a liquid N₂-cooled mercury-cadmium-telluride detector. The low volume in situ reactor was operated at atmospheric pressure and equipped with water-cooled KBr windows, connections for inlet and outlet flows, and a thermocouple connected to a temperature controller to monitor and control the sample temperature. For all experiments, 32.5 mg of finely ground Ni₂P/MCM-41 or pure MCM-41 were pressed into self-supporting wafers with a diameter of 13 mm (24.5 mg cm⁻²). Wafers were mounted vertically in a quartz sample holder to keep the incident IR beam normal to the samples. Rods of CaF₂ (13 mm diameter) were placed on both sides of the samples to minimize interference by gas phase thiophene and reduce the dead volume of the in situ reactor. Studies of the effect of temperature were conducted on the MCM-41-supported Ni₂P sample and pure MCM-41 to determine the identity and stability of the adsorbed thiophene species and reaction products. For these experiments, absorbance spectra were collected in the range 4000 – 1000 cm⁻¹ at a resolution of 4 cm⁻¹ with 64 scans per spectrum. Before dosing thiophene, the supported Ni₂P or blank support sample was pretreated in H₂ for 2 h at 803 K at a flow rate of 130 cm³(NTP) min⁻¹. After pretreatment, the samples were cooled in flowing He or H₂ (200 cm³(NTP) min⁻¹) and background spectra were collected in the absence of thiophene at 723, 673, 593, 553, 513 and 393 K (450, 400, 320, 280, 240, 120 °C). The samples were dosed at atmospheric pressure and 393 K with 1.0 mol % thiophene in He or H₂ carrier at a total flow rate of 200 cm³ (NTP) min⁻¹ until saturation was achieved. Thiophene was delivered to the sample by passing carrier gas through a thiophene-filled bubbler immersed in a temperature-controlled water bath. The thiophene vapor pressure (3.69 kPa at 278 K) was obtained by using the Antoine equation:

$$\log P^{sat} = A - \frac{B}{T + C} \quad (1)$$

where P^{sat} is the vapor pressure in mmHg, T is the bubbler temperature in °C and the coefficients are 7.06944, 1296.79 and 225.437 for A , B and C , respectively [47]. The vapor-phase concentration was adjusted to 1.0 mol% by blending the main carrier flow containing thiophene with a dilution gas stream to a total flow rate of $200 \text{ cm}^3 \text{ (NTP) min}^{-1}$. Spectra were then acquired under 1.0 mol % thiophene/carrier flow and the samples were subsequently purged with carrier gas for 300 s to remove gaseous and weakly adsorbed thiophene. Degassed sample spectra were then collected to remove the spectral features due to gas-phase thiophene. Spectra are shown with subtraction of the background contribution to highlight the thiophene adsorbate peaks. Spectra were acquired at 393, 513, 553, 593, 673 and 723 K (120, 240, 280, 320, 400, and 450 °C) with a heating rate of 5 K min^{-1} (0.083 K s^{-1}). The reactor temperature was held constant at each temperature for 180 s to collect the corresponding spectrum under thiophene/carrier flow and degassed for an additional 300 s prior to collecting the degassed spectrum.

4.2.3. In situ XAS measurements

The in situ X-ray absorption spectroscopy (XAS) measurements were carried out at BL7C in the Photon Factory, Institute for Material Structure Science, High Energy Accelerator Organization (KEK-IMSS-PF) with a ring energy of 2.5 GeV and a current of 450 mA. The X-rays passed through a Si (111) double crystal monochromator and were focused onto the sample by sagittal focussing. The extended x-ray absorption fine structure (EXAFS) and X-ray absorption near-edge structure (XANES) data were collected in transmission mode using I_0 and I

ionization chambers filled with 100% N₂ and 15 % Ar in N₂, respectively. Reaction gases were supplied by a gas handling system [48].

A quantity of 47 mg of Ni₂P/MCM-41 was pressed into a wafer of 10 mm in diameter and placed in an in situ EXAFS cell equipped with c-BN windows [15,16]. The sample was reduced as for the synthesis of the catalysts by temperature programmed reduction to 803 K (530 °C) at 5 K min⁻¹, while following the reduction with XANES. Following reduction and EXAFS analysis of the sample, adsorption or reaction measurements were carried out with thiophene in He (0.13 mol%) or in H₂ (0.13 mol%) at atmospheric pressure and 453, 513, and 573 K (180, 240, 300 °C). The sample was rereduced at 803 K (530 °C) prior to each change in temperature or gas composition.

4.2.4. Activity Tests for Thiophene HDS

Catalytic activity measurements of the HDS of thiophene were carried out in the aforementioned FTIR reactor (Figure 4.1). For the measurements of steady-state turnover rates of thiophene over Ni₂P/MCM-41, the system was operated at atmospheric pressure with a gas-phase feed containing 0.13 mol % thiophene in H₂ carrier. For all experiments, 47 mg of finely ground Ni₂P/MCM-41 was pressed into a self-supporting wafer with a diameter of 13 mm (35.4 mg cm⁻²). Prior to the kinetic measurements, the Ni₂P/MCM-41 sample was pretreated at 803 K for 2 h under 130 cm³ (NTP) min⁻¹ of flowing H₂ at atmospheric pressure. After rereduction, the reactor was cooled to the reaction temperature. Gas-phase thiophene was introduced to the reactor by passing H₂ through a thiophene-filled bubbler immersed in a low temperature water bath. The Antoine equation was again used to obtain the thiophene vapor pressure (3.69 kPa at 278 K) and the concentration was adjusted to 0.13 mol% by blending the main carrier flow

containing thiophene with a dilution H₂ stream at a flow rate of 100 cm³ (NTP) min⁻¹. The reaction was allowed to stabilize for 6 h before sampling to ensure steady-state conditions. The reactor exit was directly connected to a 6-way sampling valve for on-line GC analysis of gaseous reactants and products. Steady-state conversions and product compositions were determined by on-line analysis with a gas chromatograph (Hewlett-Packard, 5890A) equipped with a 0.32 mm i.d. x 50 m dimethylsiloxane capillary column (CPSil-5CB, Chrompack, Inc.) and a flame ionization detector. Reactants and products were identified by matching retention times to standards injected separately. The reaction was conducted at several temperatures (453, 513 and 573 K) and several measurements were made at each condition to check the attainment of steady-state. A fresh sample wafer was used for each temperature to exclude effects of deactivation of the sample during the experiments. The results of several injections at each temperature were averaged and used to calculate the turnover frequency from the following equation:

$$\text{TOF} = \frac{\text{thiophene flow rate } (\mu\text{mol/s}) \cdot \text{steady-state conversion}}{\text{catalyst weight (g)} \cdot \text{chemisorption uptake } (\mu\text{mol/g})} \quad (2)$$

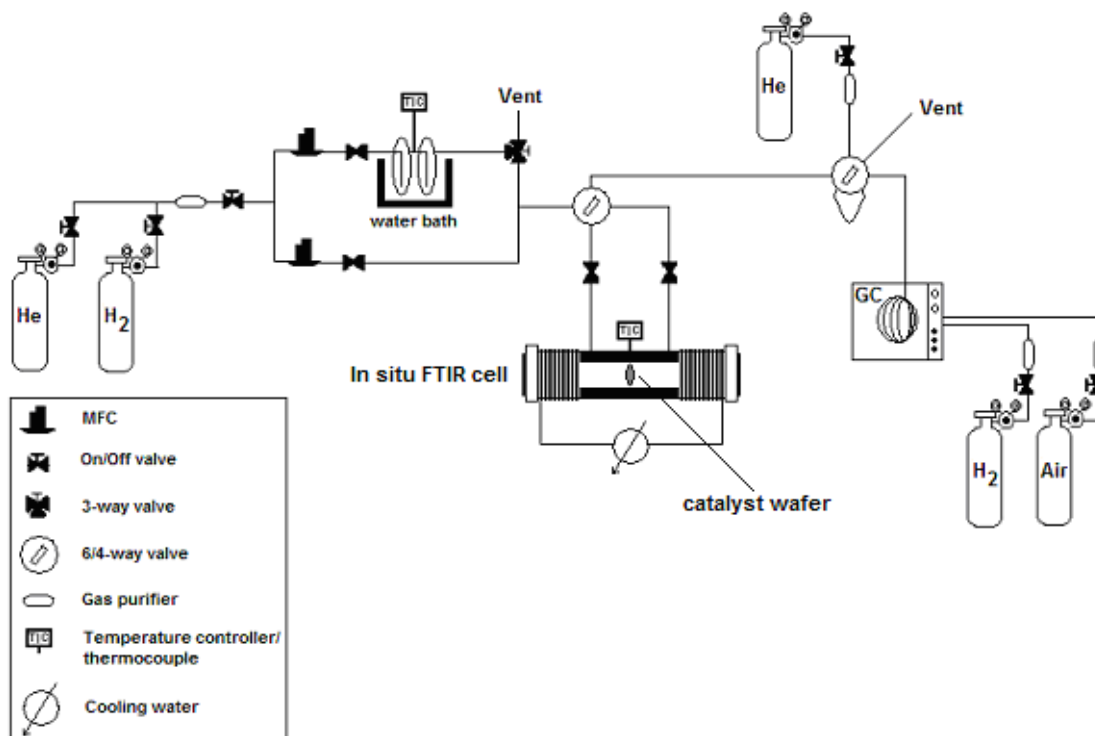


Figure 4.1. In situ FTIR reactor system

4.3. Results and Discussion

4.3.1. Catalyst Properties

The MCM-41-supported Ni₂P catalyst was prepared by the temperature-programmed reduction of supported nickel phosphate precursors. The precursor was prepared with four times the stoichiometric amount of phosphorous (Ni/P = 1/2) necessary to form Ni₂P. Previous work had shown that excess phosphorus was required to synthesize an active catalyst since some phosphorus is lost during the reduction of phosphate to phosphide. Samples prepared with

phosphorus quantities closer to stoichiometric proportions were found to form inactive phosphorus-deficient phases [49]. Figure 4.2 shows the water evolution during the temperature-programmed reduction of phosphate to phosphide for the supported samples. Masses P (31) and PH_3 (34) followed the same trend as the H_2O (18) signal and are not shown here. For the $\text{Ni}_2\text{P}/\text{MCM-41}$ catalyst sample a distinct reduction peak at 868 K is observed. A Ni_2P sample of identical loading supported on a lower surface area SiO_2 support is also shown in Figure 4.2 for comparison. The peak maximum of reduction temperature is shifted to higher temperature for the sample with higher support surface area and better dispersion. The higher reduction temperature for the MCM-41-supported Ni_2P catalyst indicates stronger interaction of Ni and phosphorus in smaller crystallites. This was shown previously and confirmed by elemental analysis of fresh $\text{Ni}_2\text{P}/\text{SiO}_2$ and $\text{Ni}_2\text{P}/\text{MCM-41}$. The MCM-41-supported sample retained more phosphorus even though a higher reduction temperature was utilized as compared to the SiO_2 -supported sample [50].

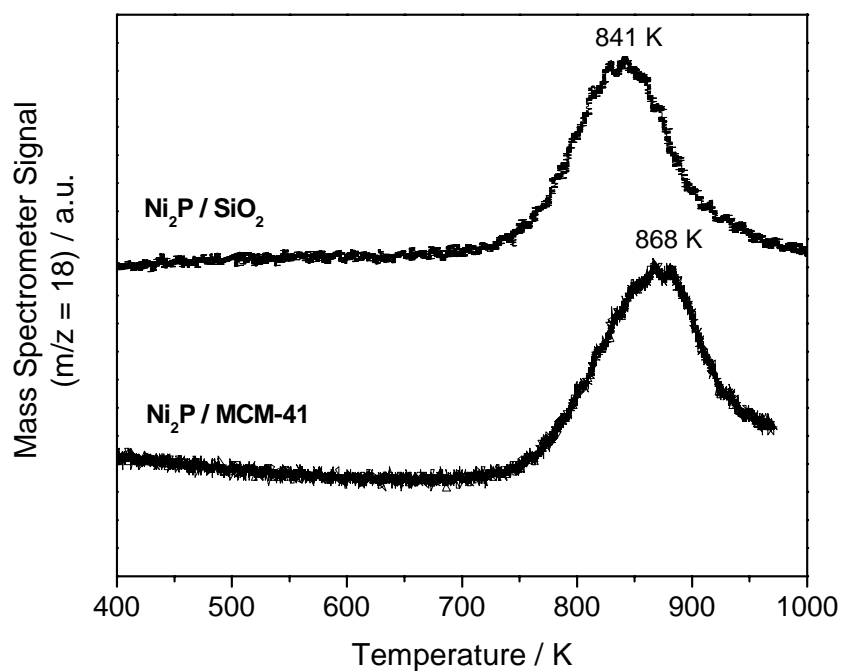


Figure 4.2. M/Z = 18 signal for TPR of the samples at $\beta = 2 \text{ K min}^{-1}$ ($.0333 \text{ K s}^{-1}$)

The reduction of the sample was also followed by Ni K-edge XANES, as shown in Figure 4.3. The arrows indicate the shifts in absorbance intensity during the course of reduction. The major feature is the white line peak at 8345.6 eV, which decreases in intensity with reduction. This is expected, as the white line is indicative of the density of unoccupied electronic states [51,52], which will be decreased by reduction. Other peaks after the white line at 8372.8, 8393.0, and 8426.9 eV, mark the onset of the EXAFS oscillations. The pre-edge feature at 8330.9 eV is associated with s to d transitions, and is sensitive to Ni coordination number changes.

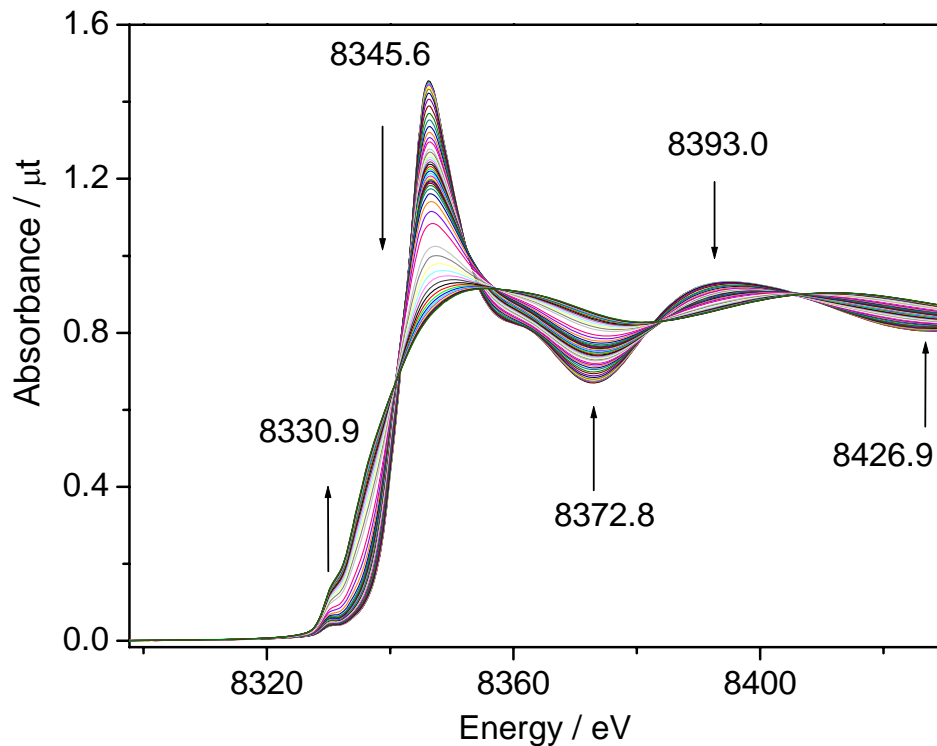


Figure 4.3. Changes in the Ni K-edge XANES region in the reduction of Ni₂P/MCM-1

The reduction of the sample was monitored by following the intensity of the absorbance at 8330.9 eV as shown in Figure 4.4. The absorbance signal starts increasing significantly after 120 min of reduction, which corresponds to a temperature of 750 K. This is in agreement with the TPR data of Figure 4.2, and indicates that the signal at 8330.9 eV can be used to follow the state of the Ni atoms in the sample. An increase in absorbance corresponds to a decrease in oxidation state as well as a decrease in coordination number (due to the removal of oxygen atoms).

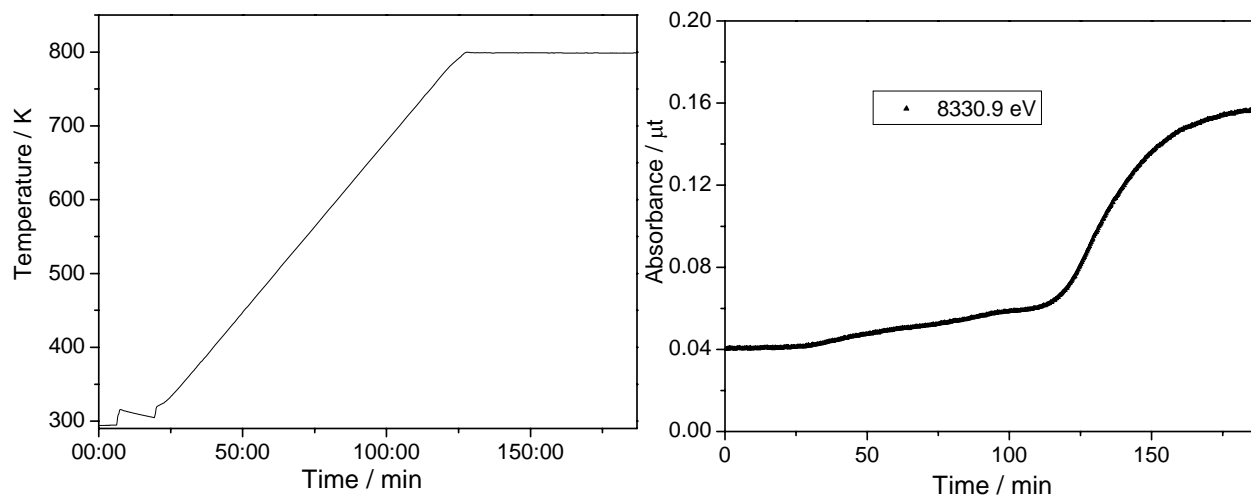


Figure 4.4. Reduction of Ni₂P/MCM-41 followed by XANES

The BET specific surface area and CO chemisorption uptake of the MCM-41-supported Ni₂P sample are listed in Table 4.1. The BET surface area was much lower than that of the fresh siliceous MCM-41 support. This could be due to filling of micro and/or mesopores upon incorporation of the active phase or because of sintering at the elevated temperatures used in the synthesis. Analysis of the sample was also carried out using extended x-ray absorption fine structure. Curve fitting analysis of the reduced catalyst using McKale parameters gave a Ni-P coordination number of 3.56 ($R = 2.246 \text{ \AA}$) and a Ni-Ni coordination of 2.39 ($R = 2.565 \text{ \AA}$). The low Ni-Ni coordination number is consistent with the dispersion of the sample (16 %) measured by chemisorption.

Table 4.1.**Physical properties of Ni₂P/MCM-41**

Sample	BET surface area / m ² g ⁻¹	CO uptake / μmol g ⁻¹	Metal dispersion / %	Particle size / nm
Ni ₂ P/MCM-41	487 (1076) ^a	188	16	6

^a BET surface area of pure siliceous support

Figure 4.5 shows the powder XRD pattern of the reduced MCM-41-supported Ni₂P catalyst after passivation. The top panel shows the diffraction pattern of a reference Ni₂P/SiO₂ sample for comparison. Both patterns exhibit a broad peak at $2\theta \sim 22^\circ$ due to the amorphous SiO₂ support and the existence of some amorphous domains in MCM-41 upon impregnation of the active phase. At higher angles the XRD pattern for Ni₂P/SiO₂ confirms the formation of the Ni₂P phase with peaks at $2\theta \sim 41^\circ, 45^\circ, 48^\circ$ and 55° . The phase corresponds to hexagonal Ni₂P which adopts the Fe₂P structure with space group $P_{\bar{6}2m}$ [53]. The pattern of a reference Ni₂P from the powder diffraction file (PDF 3-953) is also presented in the bottom panel [54]. For the Ni₂P/MCM-41 sample no peaks attributable to the Ni₂P phase are observed due to the high surface area of the support. This verifies the formation of very small Ni₂P crystallites and high dispersion of the active phase.

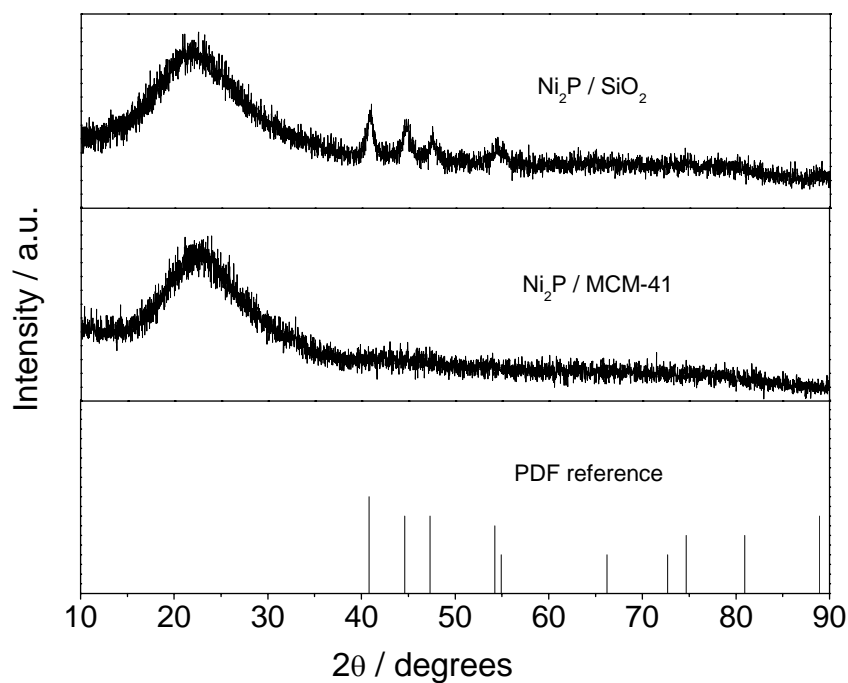


Figure 4.5. XRD patterns of supported Ni₂P catalysts

Figure 4.6 shows the powder XRD patterns at low angles of the calcined MCM-41 support and the freshly prepared Ni₂P/MCM-41 catalyst. The MCM-41 support exhibits an intense line at $2\theta \sim 2.5^\circ$ and three weak diffraction lines at $2\theta \sim 4.1^\circ$, 4.6° and 6.1° from the (100), (110), (200) and (210) planes, respectively, characteristic of hexagonal MCM-41 [55]. Impregnation of Ni₂P on MCM-41 leads to a decrease in intensity and broadening of the (100) reflection and disappearance of the higher order reflections. This suggests partial destruction of the hexagonal pore arrangement and indicates that the local structure of impregnated MCM-41 is less uniform than pure siliceous MCM-41. However, the retention of some of the MCM-41 peaks indicates that the framework structure does not deteriorate seriously during the synthesis.

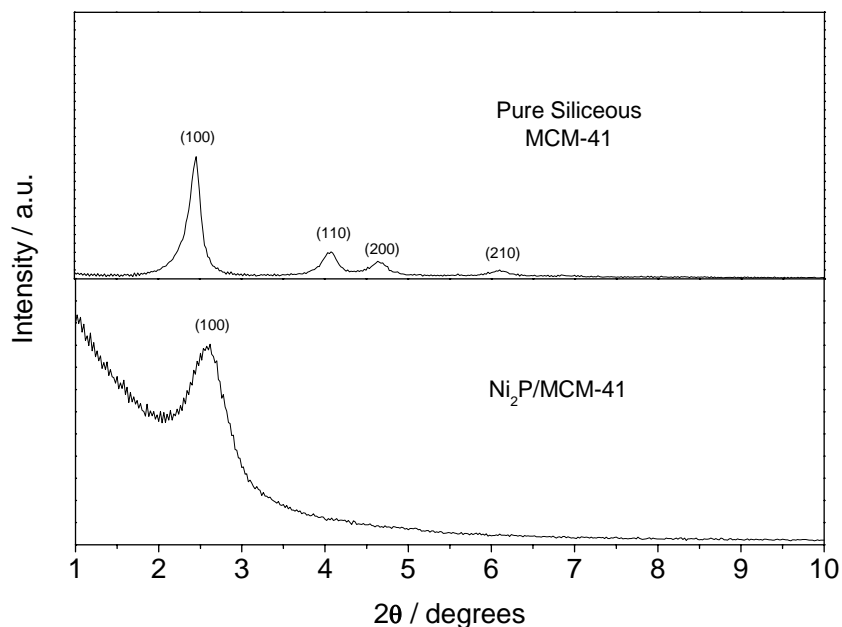


Figure 4.6. Low-angle XRD patterns of MCM-41 and Ni₂P/MCM-41

4.3.2. Infrared Measurements

Figure 4.7 shows the FTIR spectra of the pure MCM-41 support under 1 mol% thiophene/He flow. The left and right panels show the ν_{C-H} region ($3200 - 2800 \text{ cm}^{-1}$) and low wavenumber region, respectively. The spectra under 1 mol% thiophene/H₂ flow are not shown as they exhibit identical absorbance features. In the ν_{C-H} region several small peaks were located at $3134, 3125, 3109, 3098, 3090$ and 3082 cm^{-1} . With increasing temperature, no changes in the intensities of the peaks were observed. No discernible peaks were detected in the $3000 - 2800 \text{ cm}^{-1}$ range of the spectrum. In the low wavenumber region the main spectral features were located at $1622, 1584, 1574, 1491, 1454, 1420, 1410$ and 1400 cm^{-1} . The intensities of the peaks at $1622, 1491$ and 1454 cm^{-1} were observed to increase slightly from 393 to 553 K and decrease

monotonically up to 723 K. The intensities of all other feature were invariant with increasing adsorption temperature. After degassing in He flow for 300 s only peaks at 1622, 1491 and 1454 cm^{-1} remained at 393 K (spectra not shown).

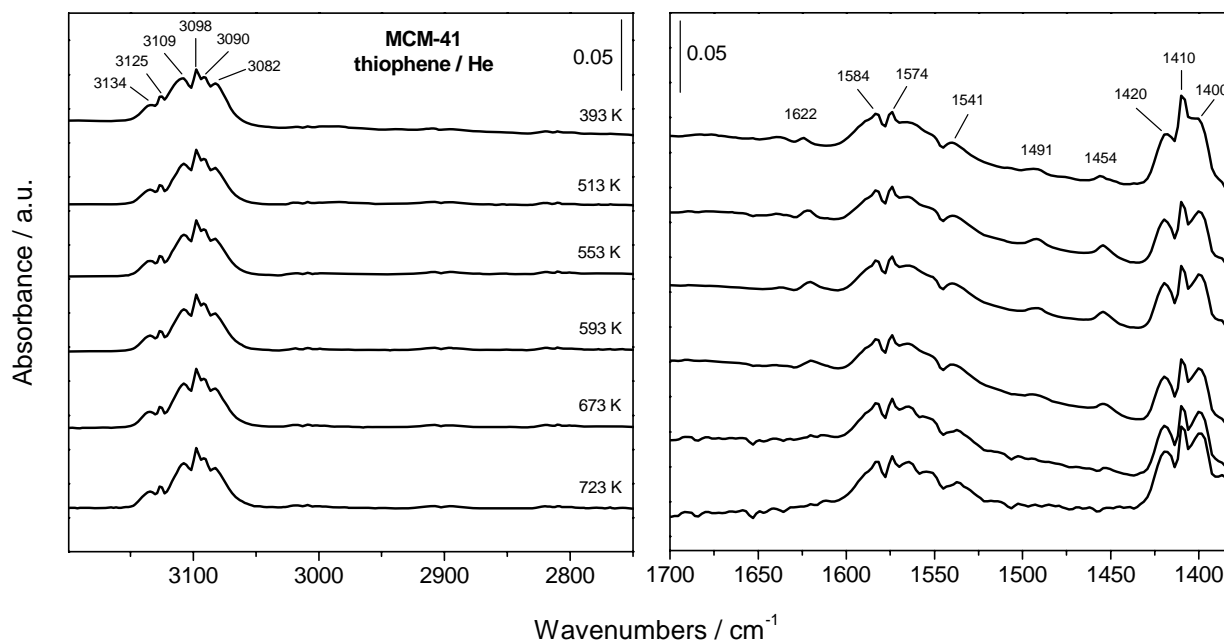


Figure 4.7. FTIR spectra of thiophene adsorbed on MCM-41 in thiophene/He flow as a function of temperature

Figure 4.8 shows the FTIR spectra after background subtraction of thiophene adsorbed on $\text{Ni}_2\text{P}/\text{MCM-41}$ in 1 mol% thiophene/He flow at high wavenumbers with the right panel highlighting the $\nu_{\text{C-H}}$ region of the spectra. Two absorbance peaks at 3742 and 3665 cm^{-1} appear as negative features and correspond to surface hydroxyl groups of siliceous MCM-41 and P-OH functionalities associated with the active phase, respectively [56]. For all spectra, because of the background subtraction a decrease in intensity of a negative peak with increasing temperature indicates growth of the peak. The opposite applies to positive features in the spectra. In the $\nu_{\text{C-H}}$

region ($3200 - 2800 \text{ cm}^{-1}$) there are several small features on a rising background found at 3134 , 3125 , 3107 , 3098 , 3090 and 3082 cm^{-1} . In addition, several broad, weak absorbance bands are clearly observed below 3000 cm^{-1} . The features in the $3200 - 3000 \text{ cm}^{-1}$ are assigned to aromatic $\nu_{\text{C-H}}$ absorbances while the weak features in the $3000 - 2800 \text{ cm}^{-1}$ region are attributed to aliphatic $\nu_{\text{C-H}}$ modes [57]. With increasing temperature, the hydroxyl band at 3742 cm^{-1} increases in negative intensity while the negative band at 3665 cm^{-1} decreases in intensity and actually becomes a positive feature above 593 K . The positive peaks between $3134 - 3082 \text{ cm}^{-1}$ remain relatively unchanged up to 723 K . The intensities of the broad features below 3000 cm^{-1} increase slightly from 393 to 553 K but diminish rapidly at higher temperatures.

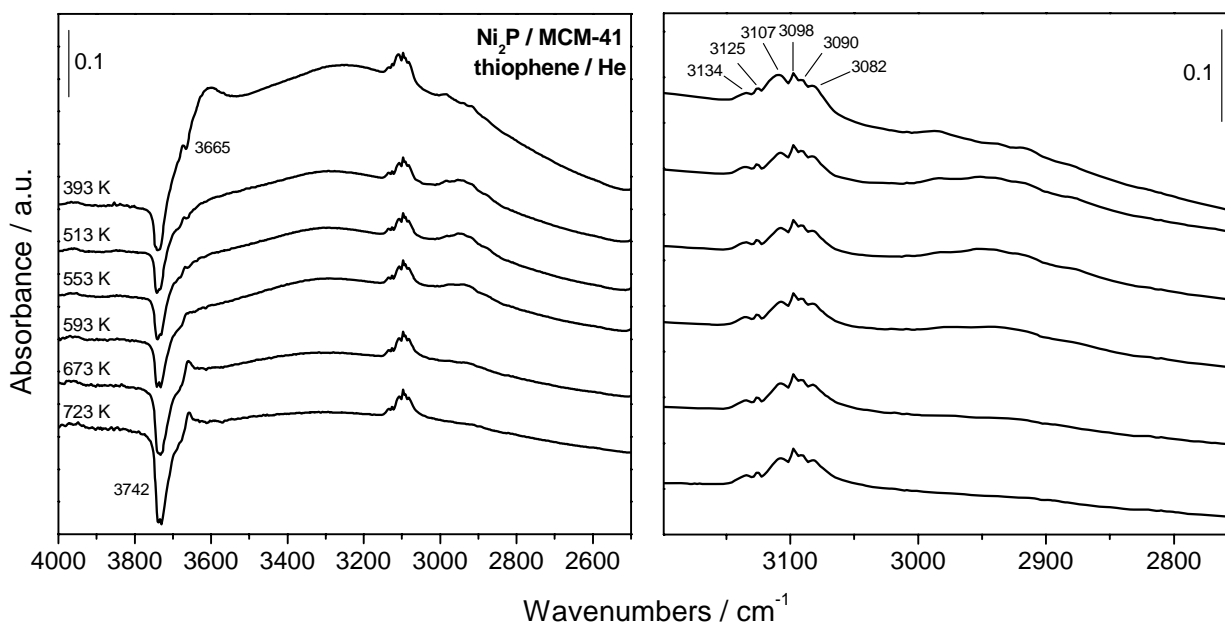


Figure 4.8. FTIR spectra of thiophene adsorbed on $\text{Ni}_2\text{P}/\text{MCM-41}$ in thiophene/He flow as a function of temperature (high wavenumber region)

Figure 4.9 shows the FTIR spectra in the low wavenumber region corresponding to Figure 4.8 of thiophene adsorbed on Ni₂P/MCM-41 in 1 mol% thiophene/He flow. The right panel highlights the $\nu_{(C=C)_{sym}}$ region of the spectra. The main spectral features were located at 1611, 1584, 1574, 1541, 1491 and 1450 cm⁻¹. In the 1450 – 1380 cm⁻¹ range, additional bands are located at 1420, 1410 and 1400 cm⁻¹. Identification of absorbance features in the 1700 – 1450 cm⁻¹ region was difficult due to poor signal-to-noise ratio. However, features at 1653, 1636, 1560 and 1506 cm⁻¹ were clearly observed at 393 K. Upon highlighting the $\nu_{(C=C)_{sym}}$ region a weak peak at 1437 cm⁻¹ was also observed at 393 K. The features at 1437, 1420, 1410 and 1400 cm⁻¹ have been assigned to the symmetric stretching modes of the C=C bonds of thiophene (mode ν_3) [58,59]. It is recognized that the $\nu_{(C=C)_{sym}}$ absorbances of thiophene are sensitive to the bonding mode of thiophene adsorbed on the catalyst surface [60,61]. Analogous to the adsorption of thiophene on pure Al₂O₃ by Bussell and coworkers, the feature at 1420 cm⁻¹ can be assigned to thiophene coordinated through its sulfur atom to coordinative unsaturated Si⁴⁺ sites created by dehydroxylation of the MCM-41 support. The absorbance peak at 1410 cm⁻¹ is tentatively assigned to physically adsorbed thiophene on the catalyst surface because this feature is also present in the thiophene gas-phase spectrum. The band at 1400 cm⁻¹ has been assigned to thiophene hydrogen-bonded through its sulfur atom to surface hydroxyl groups on the support (C₄H₄S...HO-Si) [62]. An increase in temperature led to a rapid decrease in the intensity of peaks located at 1653, 1636, 1560, 1506 and 1437 cm⁻¹. The intensities of the spectral features centered at 1611, 1491 and 1450 cm⁻¹ were observed to increase slightly upon heating to 593 K and decrease at higher temperatures. All other peaks were maintained up to 723 K.

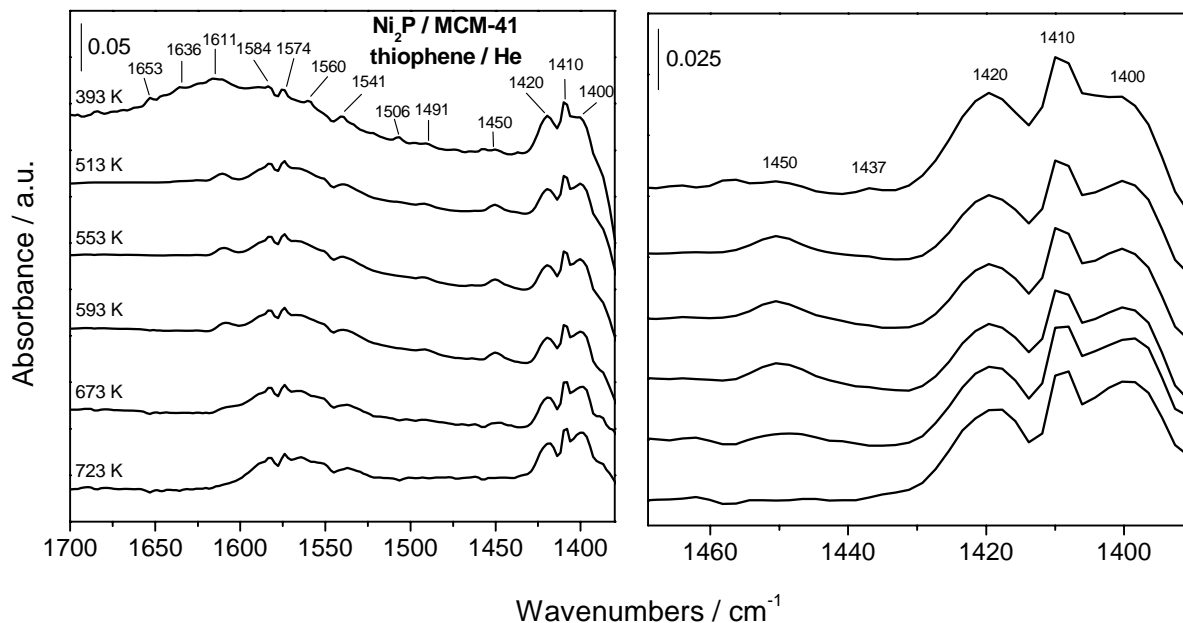


Figure 4.9. FTIR spectra of thiophene adsorbed on Ni₂P/MCM-41 in thiophene/He flow as a function of temperature (low wavenumber region)

The data in Figures 4.7-4.9 show great similarity between the pure MCM-41 and the Ni₂P/MCM-41 and indicate that thiophene is adsorbed extensively on the MCM-41 support except at the lowest temperature for the Ni₂P/MCM-41. The mode of bonding of the thiophene is molecular.

The behavior of the adsorbed species was studied by abruptly removing thiophene from the feed and switching to pure He. Figure 4.10 illustrates changes in the FTIR spectra at high (left panel) and low (right panel) wavenumbers for thiophene adsorbed on Ni₂P/MCM-41 following 300 s of degassing in He. Few changes in the spectra at high wavenumbers were observed upon removal of thiophene from the gas-phase feed. No changes in peak positions were discerned but peaks due to aromatic ν_{C-H} modes located between 3135 – 3080 cm^{-1} were undetectable even at 393 K. This indicates that molecularly adsorbed thiophene is weakly held

on the catalyst surface. In addition, some decomposition of thiophene is likely as several broad, weak features below 3000 cm^{-1} due to aliphatic $\nu_{\text{C-H}}$ modes were retained after degassing up to 593 K. These thiophene decomposition products have been shown to be strongly bonded to the surfaces of sulfided Mo/Al₂O₃ and Rh/Al₂O₃ catalysts [61]. In the low wavenumber region, peaks at 1653, 1611, 1560, 1541, 1506, 1491, 1450, 1437, 1420 and 1410 cm^{-1} were retained after degassing at 393 K. At 513 K, only peaks at 1611, 1491, 1450 and 1410 cm^{-1} were detected and these features persisted up to 593 K. The weak feature at 1437 cm^{-1} was also retained and appeared as a shoulder on the peak at 1450 cm^{-1} .

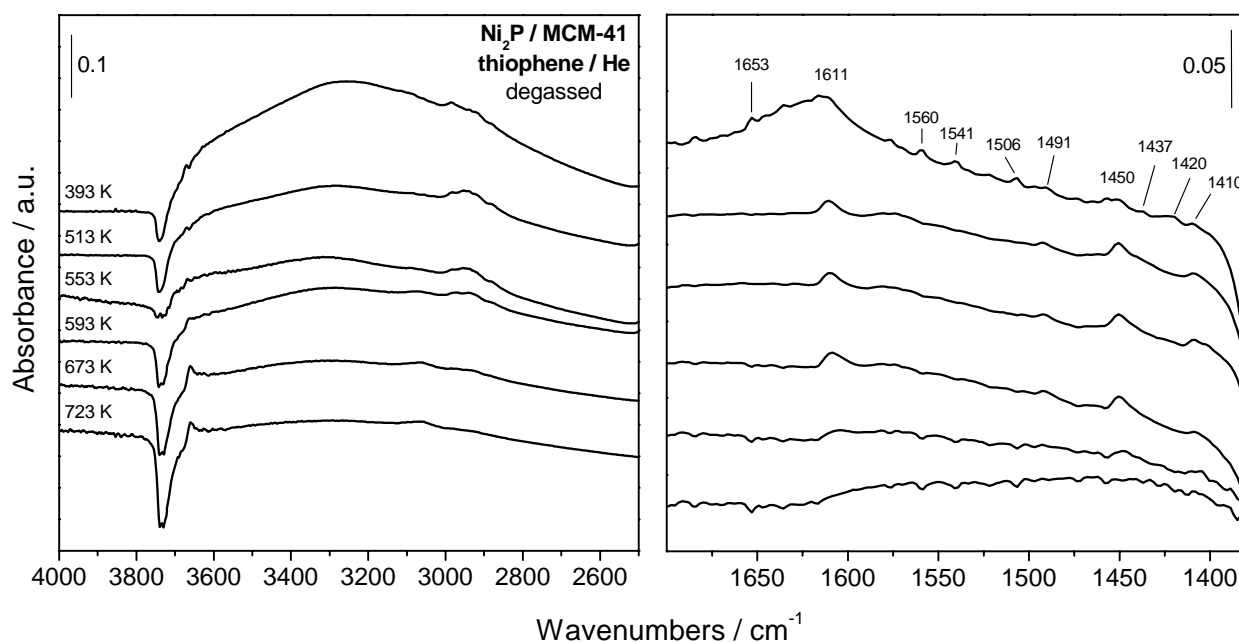


Figure 4.10. FTIR spectra of thiophene adsorbed on Ni₂P/MCM-41 after 300 s degassing in He flow as a function of temperature

Our spectroscopic results suggest that thiophene adsorbs molecularly on the catalyst surface at lower temperatures. The absorbance bands at 1437 and 1420 cm^{-1} can be reasonably

assigned to thiophene coordinated via its sulfur atom ($\eta^1(\text{S})$ mode, Scheme 2) to coordinative unsaturated (cus) Ni sites of the active phase and cus Si^{4+} of the MCM-41 support, respectively. Bussell and coworkers [58,61] studied thiophene adsorption on sulfided $\text{Mo}/\gamma\text{-Al}_2\text{O}_3$, $\text{Rh}/\gamma\text{-Al}_2\text{O}_3$ and $\gamma\text{-Al}_2\text{O}_3$ using FTIR and temperature-programmed desorption. Absorbance features at 1431 and 1420 cm^{-1} were observed and assigned to $\eta^1(\text{S})$ bonded thiophene to Mo cus and Al cus, respectively. Similar conclusions were made for thiophene adsorbed on $\text{Mo}_2\text{N}/\gamma\text{-Al}_2\text{O}_3$ by Li and coworkers [63]. For thiophene adsorption on MCM-41 (Figure 4.7), the feature at 1420 cm^{-1} is observed at all temperatures while the feature at 1437 cm^{-1} is not present. For the $\text{Ni}_2\text{P}/\text{MCM-41}$ sample, a new low intensity feature at 1437 cm^{-1} is clearly observed. Upon degassing, the peak at 1437 cm^{-1} is retained up to 513 K while the band at 1420 cm^{-1} is rapidly diminished. The low intensity of the peak at 1437 cm^{-1} due to $\eta^1(\text{S})$ bonded thiophene on Ni cus sites is likely due to the relatively high adsorption temperature and, as discussed briefly, some decomposition of thiophene on the catalyst surface.

Figure 4.11 shows the FTIR spectra at high wavenumbers of thiophene adsorbed on $\text{Ni}_2\text{P}/\text{MCM-41}$ in 1 mol% thiophene/ H_2 flow with the right panel highlighting the $\nu_{\text{C-H}}$ region of the spectra. Two negative peaks at 3740 and 3667 cm^{-1} due to hydroxyl groups were again observed. Similar to the spectra obtained in He carrier the feature at 3740 cm^{-1} was retained up to 723 K while the intensity of the feature at 3667 cm^{-1} decreased with increasing temperature. The weak features due to aromatic ν_{CH} modes at 3136, 3125, 3107, 3098, 3090 and 3080 cm^{-1} were again observed. The other major spectral features included three new bands with high intensity centered at 2953, 2918 and 2876 cm^{-1} . An increase in temperature from 393 to 553 K led to an increase in intensity of the peaks at 2953, 2918 and 2876 cm^{-1} . These are again assigned to aliphatic ν_{CH} modes of absorption. These features were observed in the 3000 – 2800

cm⁻¹ range under He flow (Figures 4.8 and 4.10), although much weaker in intensity. In He flow, the appearance of aliphatic ν_{CH} modes is likely attributable to some decomposition of thiophene on the catalyst surface and formation of adsorbed C₄ hydrocarbons. Such decomposition under inert conditions has been observed upon adsorption of thiophene on Ni single crystals, even at low temperatures (150 K) [64,65]. Above 553 K the intensity of these peaks were observed to decrease with increasing temperature up to 723 K. An increase in temperature from 393 K to 513 K led to a slight decrease in intensity of the features at 3136, 3125, 3107, 3098, 3090 and 3080 cm⁻¹. Above 513 K the intensities of these peaks were invariant with increasing temperature.

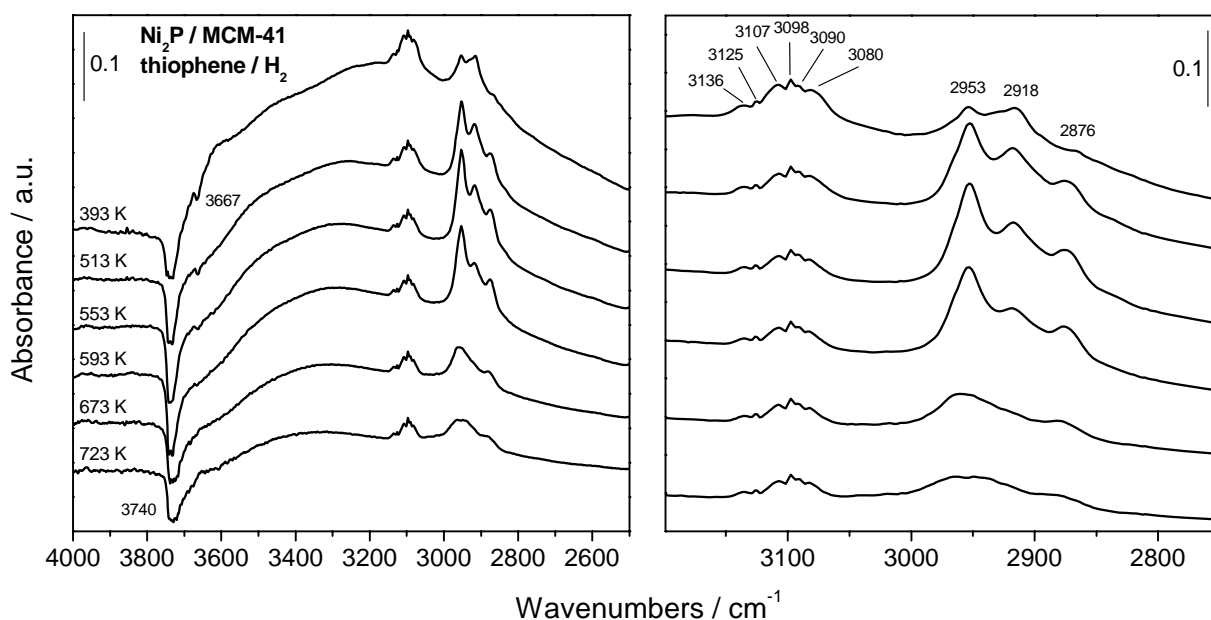


Figure 4.11. FTIR spectra of thiophene adsorbed on Ni₂P/MCM-41 in thiophene/H₂ flow as a function of temperature (high wavenumber region)

Figure 4.12 shows the FTIR spectra of thiophene adsorbed on Ni₂P/MCM-41 in 1 mol% thiophene/H₂ flow in the low wavenumber region of the spectra. The right panel highlights the

$\nu_{(C=C)_{sym}}$ region of the spectra. The main spectral features were located at 1638, 1601, 1491, 1449, 1420, 1410 and 1400 cm^{-1} . The peaks are very similar to those obtained under He flow but the features at 1491 and 1449 cm^{-1} are much more intense. Additional smaller peaks centered at 1653, 1638, 1626, 1584, 1576, 1558, 1551, 1541, 1506 and 1464 cm^{-1} were observed in the 1700 – 1460 cm^{-1} range. Upon highlighting the $\nu_{(C=C)_{sym}}$ region of the spectra a small peak at 1437 cm^{-1} is again observed. An increase of temperature led to a decrease in the intensity of peaks located at 1653, 1638, 1626, 1601, 1506, 1491 and 1449 cm^{-1} while all other peaks were retained up to 723 K. The peak at 1464 cm^{-1} , which appears as a shoulder on the feature at 1449 cm^{-1} , was observed to grow in intensity with heating from 393 to 553 K. At higher temperature the intensity of the feature diminished rapidly.

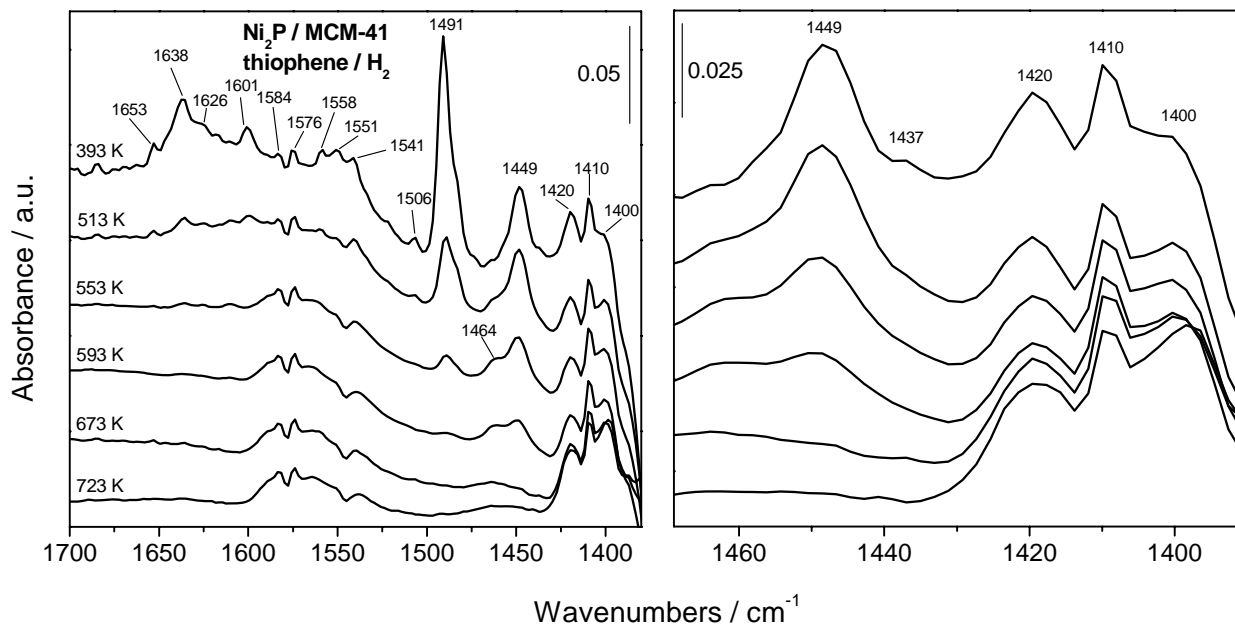


Figure 4.12. FTIR spectra of thiophene adsorbed on Ni₂P/MCM-41 in thiophene/H₂ flow as a function of temperature (low wavenumber region)

The behavior of the adsorbed species was again studied by abruptly removing thiophene from the feed and switching to pure H₂. Figure 4.13 illustrates changes in the FTIR spectra at high (left panel) and low (right panel) wavenumbers for thiophene adsorbed on Ni₂P/MCM-41 following 300 s of degassing in H₂. Once again, peaks located between 3136 – 3080 were diminished in intensity and undetectable above 393 K. The three strong peaks at 2953, 2918 and 2876 cm⁻¹ were retained following degassing although with slightly reduced intensity. In the low wavenumber region peaks at 1653, 1638, 1626, 1601, 1506, 1491, 1464 and 1449 cm⁻¹ were retained after degassing in H₂ at 393 K. The intensities of the two strong peaks at 1491 and 1449 cm⁻¹ were maintained, but diminished rapidly with heating. The feature at 1464 cm⁻¹ was again observed to increase with heating up to 553 K and diminish at higher temperatures. In addition, a new peak at 1549 cm⁻¹ was observed.

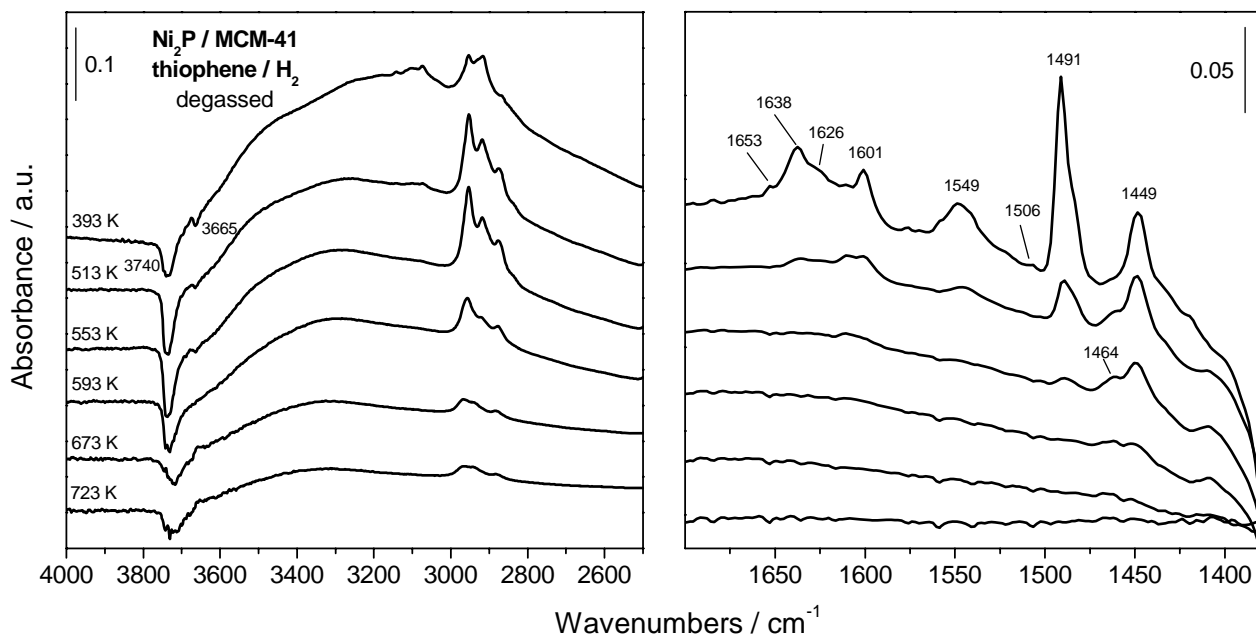
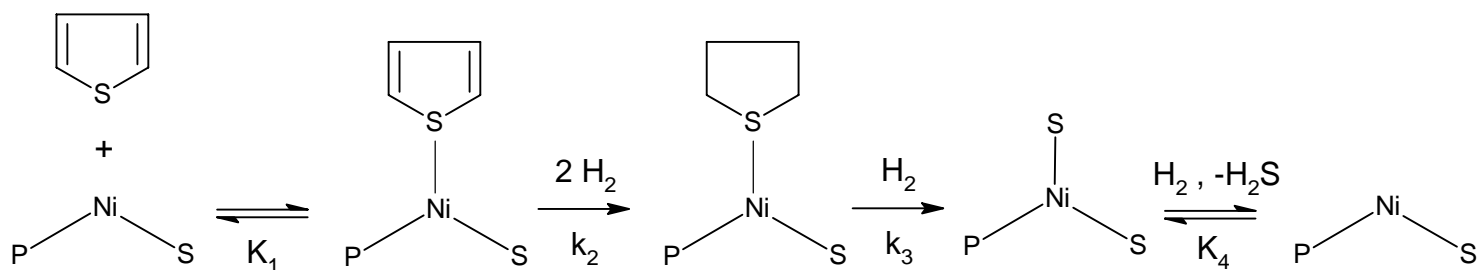


Figure 4.13. FTIR spectra of thiophene adsorbed on Ni₂P/MCM-41 after 300 s degassing in H₂ flow as a function of temperature

As shown in Scheme 4.1 the products of thiophene HDS are typically 1,3-butadiene, 1-butene, 2-butene (cis- and trans-) and butane. In order to interpret the resulting spectra during thiophene reaction, Li and coworkers [63] employed in situ FTIR and adsorption of these HDS products over $\text{Mo}_2\text{N}/\gamma\text{-Al}_2\text{O}_3$. For the desulfurized products of thiophene reaction over the $\text{Ni}_2\text{P}/\text{MCM-41}$ sample, a similar interpretation can be applied. Over a reduced $\text{Mo}_2\text{N}/\gamma\text{-Al}_2\text{O}_3$ catalyst, the three butene products exhibited nearly identical absorbance peaks at 3010, 2965, 2922, 2860, 1619, 1612, 1452, 1408 and 1381 cm^{-1} . The observed surface species were attributed to π - and σ -bonded butenes [66,67]. Adsorption of 1,3-butadiene gave absorbance peaks located at 3010, 3005, 2920, 2850, 1616, 1565, 1490, 1457, 1417 and 1378 cm^{-1} . These features were assigned to π -adsorbed butadiene and σ -bonded and dehydrogenated butadiene species on the catalyst surface [66]. For reaction of thiophene over $\text{Ni}_2\text{P}/\text{MCM-41}$, the strong IR bands in the aliphatic $\nu_{\text{C-H}}$ region ($3000 - 2800\text{ cm}^{-1}$) and the intense peaks centered at 1549, 1491 and 1449 cm^{-1} can be assigned to vibrations of CH_2 and CH_3 groups of adsorbed C_4 hydrocarbons [68]. Analogous to the thiophene reaction on the nitride catalyst, the intense peak at 1491 cm^{-1} can be assigned to a significant amount of surface adsorbed 1,3-butadiene. The band at 1491 cm^{-1} is likely due to di- π -adsorbed 1,3-butadiene ($\nu_{\text{C=C}}$ mode) while the band at 1549 cm^{-1} can be tentatively assigned to a singularly π -bonded 1,3-butadiene species ($\nu_{\text{C=C}}$ mode) [66]. The feature at 1449 cm^{-1} is likely due to both π - and σ -bonded butenes. However, for 1-butene, Li and coworkers [66] gave evidence that this band is likely attributable to the presence of a σ -allyl butene species ($\delta(\text{CH}_3)_{\text{as}}/\delta(\text{CH}_2)_{\text{as}}$) via isomerization.

Overall, the FTIR results are consistent with a reaction sequence for thiophene HDS shown in Scheme 4.3. Thiophene is adsorbed and forms an $\eta^1(\text{S})$ bonded complex with nickel. This is hydrogenated to form the tetrahydrothiophene species with aliphatic ν_{CH} peaks at 2953,

2918 and 2876 cm^{-1} which increased in intensity from 393 to 553 K and decreased and higher temperatures. Analogously, the feature at 1464 cm^{-1} (Figures 4.12 and 4.13) exhibits a similar temperature dependence and can be reasonably assigned to asymmetric CH_2 scissoring (mode ν_{21}) of tetrahydrothiophene [69]. The tetrahydrothiophene increased in concentration as temperature was increased from 393 to 553 K because it is formed as a result of two sequential processes of different temperature dependence. At high temperature, the cleavage of C-S bonds to form the surface sulfur species, accelerates relative to the hydrogenation step, and the concentration of the tetrahydrothiophene surface species diminishes. Other species observed, like molecularly adsorbed thiophene and the hydrocarbons probably reside on the support.



Scheme 4.3. Simplified surface HDS mechanism showing adsorbed tetrahydrothiophene and deposited sulfur

The scheme above assumes that thiophene hydrogenation (step 2) and tetrahydrothiophene desulfurization (step 3) are kinetically significant, and that thiophene adsorption and sulfur hydrogenation are equilibrated. This gives rise to the following rate expression:

$$r = \frac{k_2 K_1 (H_2)^2 (\text{thiophene})}{[1 + (k_2/k_3) K_1 (H_2)^2 (\text{thiophene})]} \quad (3)$$

$$r = k'(H_2)^{2\alpha}(\text{thiophene})^\alpha \quad k' = (k_2K_1)^{2\alpha}k_3^{-\beta} \quad (4)$$

Rate expressions in which the reaction order in H₂ was twice the order in thiophene have been proposed previously, especially for catalyst with high hydrogenation activity. Hensen and coworkers [70] measured the kinetics of thiophene HDS at 623 K in the presence of 1 kPa H₂S over several C-supported transition metal sulfides. The authors determined that the reaction order in H₂ was approximately twice the order in thiophene for sulfided Ru/C, Rh/C and Pd/C. The latter expression (Equation 4) gives rise to the following expression for the apparent activation energy, $E_{app} = \alpha(E_2 + \Delta H_1) - \beta E_3$.

4.3.3. XANES Measurements

Figure 4.14 shows XANES measurements of the Ni₂P/MCM-41 sample exposed to thiophene/H₂ mixtures (time zero) at different temperatures. The absorbance at 8330.9 eV shows a rapid decrease in intensity to steady values that are indicative of the interaction of thiophene with the catalyst. The spike at time zero is an artifact due to the switch in gas streams. As stated earlier, a decrease in absorbance is indicative of an increase in the oxidation state and coordination of the Ni centers. The greater drop in absorbance with temperature indicates that the coverage in sulfur species at the surface is higher at higher temperatures.

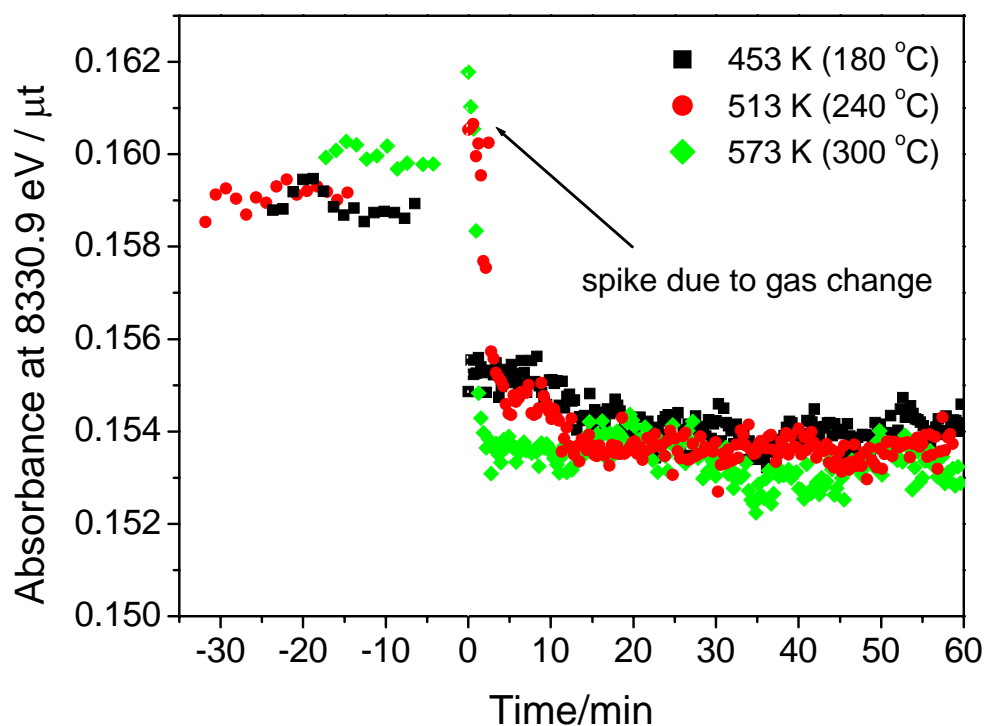


Figure 14.4. XANES measurements of the Ni₂P/MCM-41 sample exposed to thiophene/H₂ (0.13 mol%)

Figure 4.15 compares the initial decline in absorbance at 8330.9 eV due to thiophene adsorption in H₂ and He carriers. The absorbance values are slightly different in the two carrier gases because of the absorbance characteristics of both gases. It is possible to roughly estimate the percentage decline in the initial stages of the absorbance by taking slopes ($d\mu/dt$) as indicated in the figures. Since the absorbance is related to the thiophene coverage, the slopes are indicative of the rates of thiophene adsorption ($d\theta/dt$).

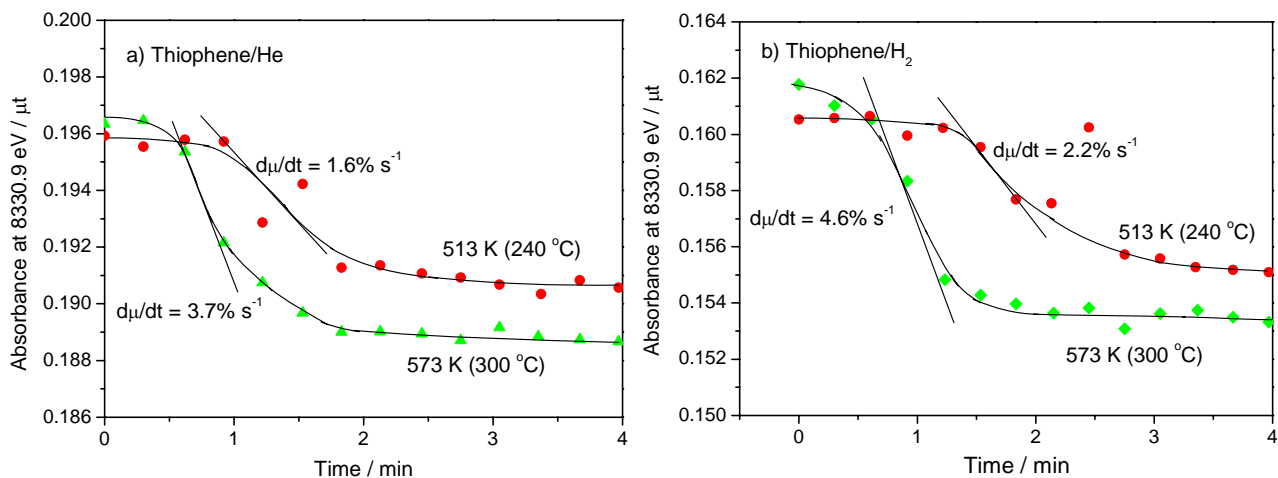


Figure 4.15. Decline in absorbance at 8330.9 eV for thiophene adsorption.

a) Thiophene/He = 0.13 mol% b) Thiophene/H₂ = 0.13 mol%

For the thiophene in He curve, the change in coverage with time gives the net rate of adsorption.

$$\left(\frac{d\theta}{dt}\right)_{He} = r_{ads} - r_{des} \quad (5)$$

For the thiophene in H₂ curve, the change in coverage also includes the rate of reaction.

$$\left(\frac{d\theta}{dt}\right)_{H_2} = r_{ads} - r_{des} - r_{rxn} \quad (6)$$

The difference in both quantities can be used to give the rate of reaction.

$$\left(\frac{d\theta}{dt}\right)_{He} - \left(\frac{d\theta}{dt}\right)_{H_2} = r_{rxn} \quad (7)$$

A limitation in this analysis is that the absorbance, μ , has not been related quantitatively to the coverage, θ . However, assuming linearity, and estimating an approximate correspondence between the percentage values, allows a very rough order-of-magnitude determination. Thus, at 513 K (240 °C) the reaction rate can be calculated to be:

$$\left(\frac{d\theta}{dt}\right)_{He} - \left(\frac{d\theta}{dt}\right)_{H_2} = -1.6 - (-2.2) \% s^{-1} = 0.6 \% s^{-1} = 0.006 s^{-1} \quad (8)$$

At 573 K (300 °C) the reaction rate can be calculated to be:

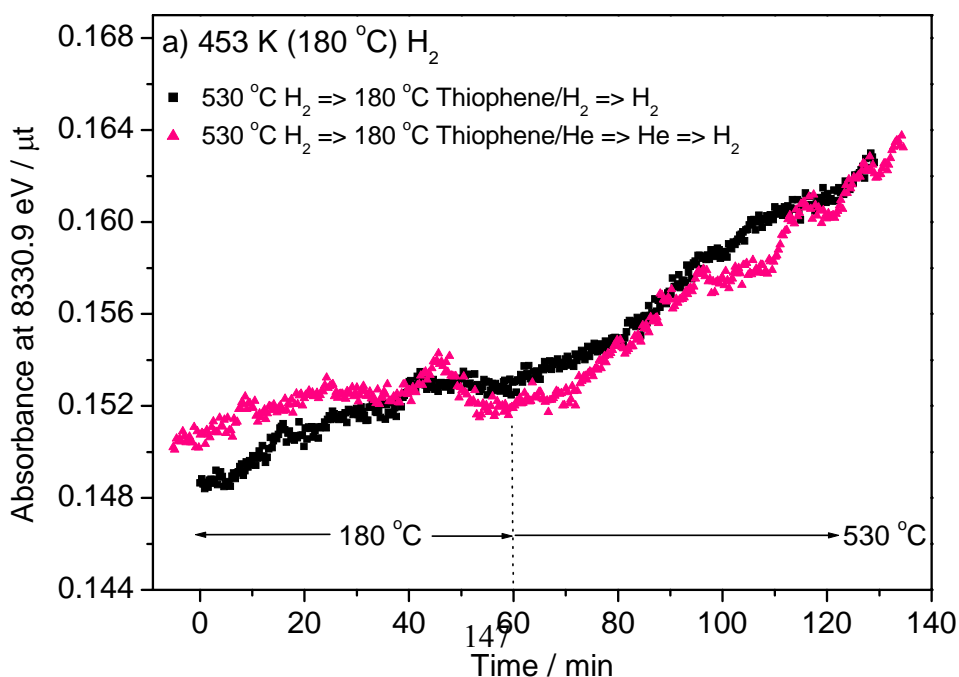
$$\left(\frac{d\theta}{dt}\right)_{He} - \left(\frac{d\theta}{dt}\right)_{H_2} = -3.7 - (-4.6) \% s^{-1} = 0.9 \% s^{-1} = 0.009 s^{-1} \quad (9)$$

These calculated values are close to the measured turnover frequencies of $0.0071 s^{-1}$ at 513 K (240 °C) and $0.0082 s^{-1}$ at 573 K (300 °C).

In previous work [14,49] it was suggested that the active phase of Ni₂P consisted of a phosphosulfide. It was therefore of interest to check the nature of the sulfur species on the surface of Ni₂P/MCM-41.

Figure 4.16 shows XANES traces obtained in isothermal and temperature-programmed experiments with adsorbed thiophene on samples that have been reduced at 530 °C before each change in condition. The increase in absorbance indicates a decline in Ni-S coordination. The

left part of Figure 4.16 a) shows the signals when flows of thiophene in H₂ at 180 °C are changed to pure H₂. In the isothermal region at 180 °C the absorbance increases and reaches a plateau, indicating that adsorbed thiophene (the tetrahydrothiophene intermediate) has desorbed. When the temperature is now ramped to 530 °C the absorbance increases again. This is indicative of the removal of further sulfur, and this is interpreted as removal of the phosphosulfide sulfur. Similar results are presented in Figure 4.16 b) where the left part of the figure shows the signals when flows of thiophene in H₂ and He at 240 °C are changed to pure H₂. In the isothermal portion at 240 °C the signals reach a plateau as the adsorbed thiophene (tetrahydrothiophene) is desorbed. When the temperature is then ramped to 530 °C the absorbance increases in the same manner for all samples. Again, the interpretation is that this corresponds to the removal of the phosphosulfide sulfur. The experiments are repeated in Figure 4.16 c) where the left part of the figure shows the signals in flows of thiophene in H₂ and He at 300 °C which are changed to pure H₂. In the isothermal region at 300 °C the signals reach a plateau as the adsorbed thiophene (tetrahydrothiophene) is desorbed. When the temperature is ramped to 530 °C the absorbance increases as the phosphosulfide sulfur is removed.



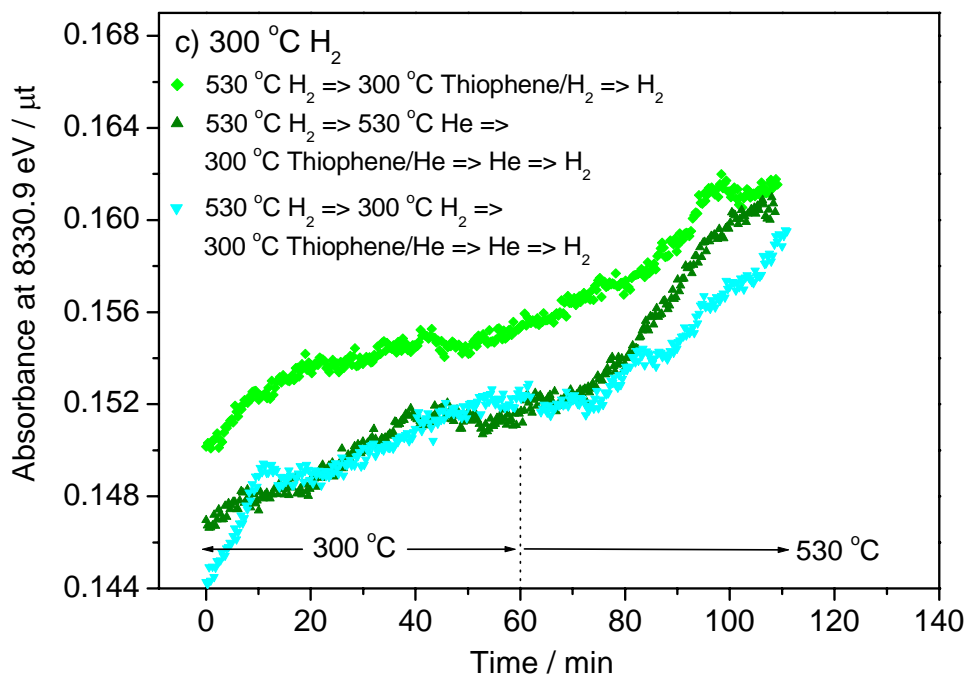
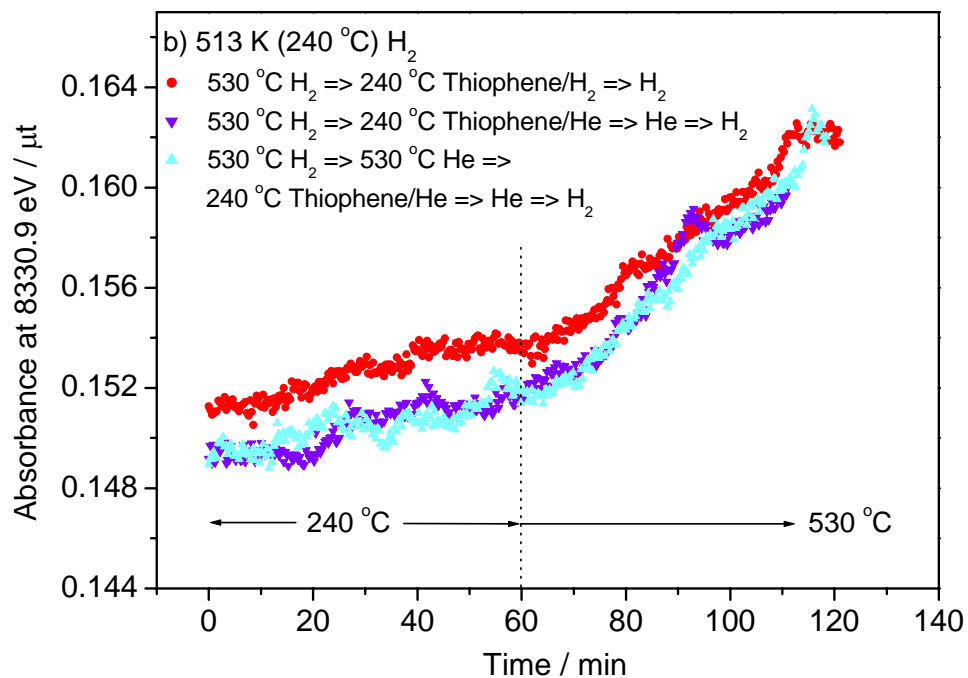


Figure 4.16. XANES measurements of adsorbed thiophene undergoing TPR in H₂

a) Reaction at 453 K (180 °C) b) Reaction at 513 K (240 °C) c) Reaction at 573 K (300 °C)

The conclusion of this work is that there are two types of sulfur that are observable by XANES. One type is associated with an adsorbed sulfur-containing species, which is suggested to be tetrahydrothiophene, from the observation of aliphatic C-H stretches and C-C stretches in the FTIR spectrum. The other type is a phosphosulfide sulfur that is strongly held on the surface of the Ni₂P catalyst. Dynamic experiments show that the adsorbed species is a reactive intermediate because it reacts at the same rate as the steady-state rate.

4.3.4. Steady-State HDS Activity

Table 4.2 summarizes the thiophene HDS results for the Ni₂P/MCM-41 sample as a function of temperature at atmospheric pressure. The activity tests were conducted with the same amount of catalyst charged to the reactor (0.047 g) as for the transient XANES measurements. Additionally, all experiments were conducted at the same weight hourly space velocity (WHSV = 22.2 h⁻¹). The conversion of thiophene was observed to increase with increasing temperature, as expected. The selectivity for HDS products was 100% at all reaction temperatures. The observed HDS products were C₄ hydrocarbons (butenes and butane). Table 4.2 also presents the turnover frequencies for the Ni₂P/MCM-41 catalyst in the HDS of thiophene as a function of temperature at atmospheric pressure. Using the measured thiophene conversions, the TOFs for thiophene reaction were calculated with Equation 2 based on the CO uptake value for the MCM-41-supported Ni₂P catalyst (Table 4.1). The measured TOFs for thiophene HDS at 513 and 573 K are in good agreement with the values obtained in the XANES measurements.

Table 4.2.
Steady-state thiophene HDS results

Sample	Temperature / K	Conversion / %	TOF / s ⁻¹
Ni ₂ P / MCM-41	573	80	0.0082
	513	69	0.0071
	453	57	0.0058

Figure 4.17 presents the Arrhenius plot for the HDS of thiophene as a function of temperature over the Ni₂P/MCM-41 catalyst. The apparent activation energy for the HDS of thiophene was obtained from the slope of the Arrhenius plot:

$$\ln(TOF) = \ln A - \left(\frac{E_a}{RT} \right) \quad (10)$$

where A is the apparent frequency factor, E_a is the apparent activation energy (kJ mol⁻¹), R is the gas constant (8.3144 J mol⁻¹ K⁻¹) and T is temperature (K). The calculated apparent activation energy for thiophene HDS over Ni₂P/MCM-41 was 6.24 kJ mol⁻¹. The linearity of the experimental results indicates that the reaction mechanism does not change over the temperature range studied.

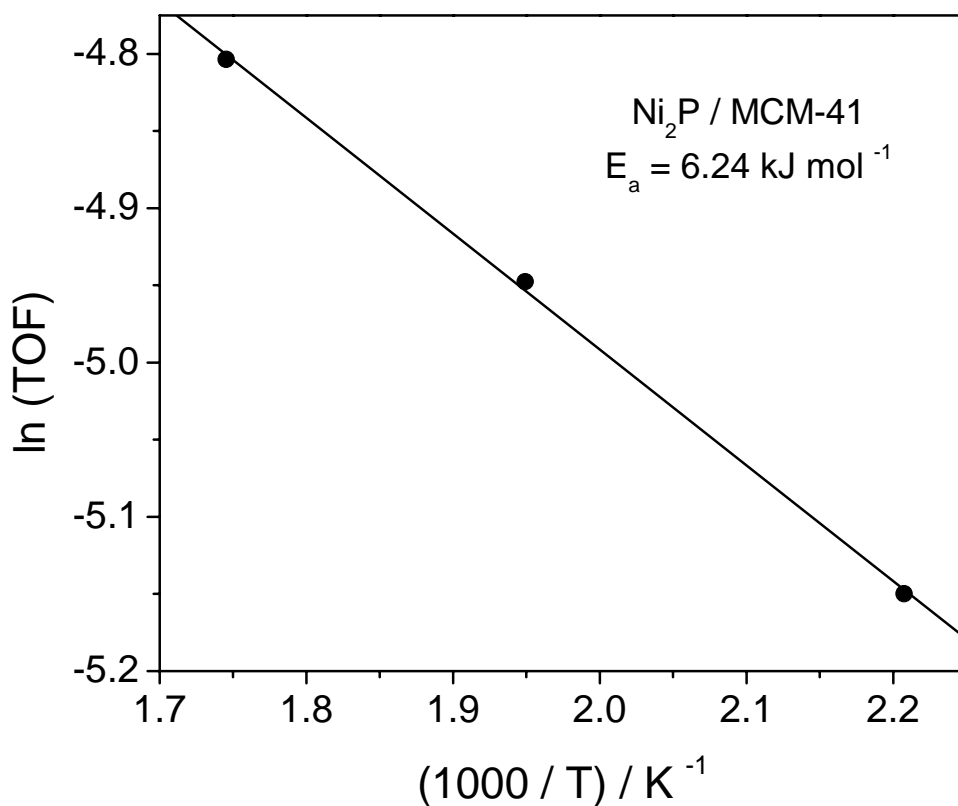


Figure 4.17. Arrhenius plot of thiophene HDS over Ni₂P/MCM-41

Absence of internal diffusion limitations was checked using the Weisz-Prater criterion [71]. It was confirmed that at the highest temperature used (573 K, 300 °C) the quantity R^2r/C_sD_e had a value of 0.31, where R is the thickness of the catalyst wafer (0.030 cm), r is the volumetric rate ($1.8 \times 10^{-6} \text{ mol cm}^{-3} \text{ s}^{-1}$), C_s is the thiophene concentration ($5.3 \times 10^{-8} \text{ mol cm}^{-3}$) and D_e is the diffusivity of thiophene ($0.10 \text{ cm}^2 \text{ s}^{-1}$). The value satisfied the criterion, $R^2r/C_sD_e < 1$, suggesting no internal diffusion limitations or concentration gradient within the catalyst wafer. The low apparent activation energy is due to the presence of two consecutive steps (Scheme 3) which gives rise the apparent activation energy noted before $E_{\text{app}} = \alpha(E_2 + \Delta H_1) - \beta E_3$.

4.4. Conclusions

The hydrodesulfurization (HDS) of thiophene was studied on Ni₂P/MCM-41 using in situ Fourier transform infrared (FTIR) spectroscopy and near-edge x-ray absorption fine-structure (XANES). The FTIR measurements showed the appearance of an adsorbed hydrogenated species, presumed to be tetrahydrothiophene, when thiophene and hydrogen were passed over the catalyst. The intensity of the FTIR peaks rose with temperature and then declined, indicating that the steps for formation and reaction of the species had different temperature dependencies. In situ XANES measurements confirmed the presence of the intermediate through the monitoring of a signal that responded to the formation of Ni-S bonds. Dynamic experiments with XANES in which the adsorbed intermediate was desorbed in He and H₂ allowed the estimation of its rate of reaction at two temperatures. These rates corresponded closely to the overall turnover frequency of reaction, and indicated that the adsorbed intermediate was a true reaction intermediate. Additional XANES experiments showed that the surface of the Ni₂P/MCM-41 was likely a phosphosulfide, in agreement with past determinations.

References

- [1] K.P. Zhdanova, M.A. Lur'e, I.Z. Kurets, E. Kh. Kim, F.K. Shmidt, *Kinet. Catal.* 41 (2000) 892.
- [2] Y. Kanda, T. Aizawa, T. Kobayashi, Y. Uemichi, S. Namba, M. Sugioka, *Appl. Catal., B* 77 (2007) 117.
- [3] W. Wu, Z. Wu, Z. Feng, P. Ying, C. Li, *Phys. Chem. Chem. Phys.* 6 (2004) 5596.
- [4] M.A. Larrubia, A. Gutiérrez-Alejandre, J. Ramirez, G. Busca, *Appl. Catal., A* 224 (2002) 167.
- [5] Z. Wu, Y. Chu, S. Yang, Z. Wei, C. Li, Q. Xin, *J. Catal.* 194 (2000) 23.
- [6] V. Schwartz, M. Sun, R. Prins, *J. Phys. Chem. B* 106 (2002) 2597.
- [7] M. Taniguchi, D. Imamura, H. Ishige, Y. Ishii, T. Murata, M. Hidai, T. Tatsumi, *J. Catal.* 187 (1999) 139.
- [8] N. Frizi, P. Blanchard, E. Payen, P. Baranek, M. Rebeilleau, C. Dupuy, J.P. Dath, *Catal. Today* 130 (2008) 272.
- [9] Y. Yoshimura, M. Toba, T. Matsui, M. Harada, Y. Ichihashi, K.K. Bando, H. Yasuda, H. Ishihara, Y. Morita, T. Kameoka, *Appl. Catal., A* 322 (2007) 152.
- [10] R. Cattaneo, T. Weber, T. Shido, R. Prins, *J. Catal.* 191 (2000) 225.
- [11] C. Stinner, R. Prins, T. Weber, *J. Catal.* 191 (2000) 438.
- [12] D. C. Phillips, S. J. Sawhill, R. Self, M. E., Bussell, *J. Catal.* 207 (2002) 266.
- [13] S. T. Oyama, *J. Catal.* 216 (2003) 343.
- [14] S. T. Oyama, X. Wang, Y.-K. Lee, W.-J. Chun, *J. Catal.* 221 (2004) 263.

-
- [15] T. Kawai, S. Sato, W. J. Chun, K. Asakura, K. K. Bando, T. Matsui, Y. Yoshimura, T. Kubota, Y. Okamoto, Y. K. Lee, S. T. Oyama, *Chem. Lett.* 32 (2003) 956.
- [16] T. Kawai, S. Sato, W. J. Chun, K. Asakura, K. K. Bando, T. Matsui, Y. Yoshimura, T. Kubota, Y. Okamoto, Y. K. Lee, S. T. Oyama, *Physica Scripta* (2004) T115.
- [17] S. T. Oyama, Y.-K. Lee, *J. Catal.*, 258 (2008) 393.
- [18] H. Topsøe, B.S. Clausen, F.E. Massoth, *Hydrotreating Catalysis-Science and Technology*, Springer-Verlag, Berlin, 1996.
- [19] M.J. Girgis, B.C. Gates, *Ind. Eng. Chem. Res.* 30 (1991) 2021.
- [20] R. Shafi, G.J. Hutchings, *Catal. Today* 59 (2000) 423.
- [21] A.E. Hargreaves, J.R.H. Ross, *J. Catal.* 56 (1979) 363.
- [22] K.F. McCarthy, G.L. Schrader, *J. Catal.* 103 (1987) 261.
- [23] A.N. Startsev, V.A. Burmistrov Y. Yermakov, *Appl. Catal.* 45 (1988) 191.
- [24] E.J. Markel, G.L. Schrader, N.N. Sauer, R.J. Angelici, *J. Catal.* 116 (1989) 11.
- [25] J. Kraus, M. Zdrzil, *React. Kinet. Catal. Lett.* 6 (1977) 475.
- [26] E.J.M. Hensen, M.J. Vissenberg, V.H.J. de Beer, J.A.R. van Veen, R.A. van Santen, *J. Catal.* 163 (1996) 429.
- [27] S. Kolboe, *Can. J. Chem.* 47 (1969) 352.
- [28] W.R. Moser, G.A. Rossetti Jr., J.T. Gleaves, J.R. Ebner, *J. Catal.* 127 (1991) 190.
- [29] A. Borgna, E.J.M. Hensen, L. Coulier, M.H.J.M. de Croon, J.C. Schouten, J.A.R. van Veen, J.W. Niemantsverdriet, *Catal. Lett.* 90 (2003) 117.
- [30] B.T. Carvill, M.J. Thompson, *Appl. Catal.* 75 (1991) 249.
- [31] R.J.C. Osbaldiston, E.J. Markel, *J. Mol. Catal.* 91 (1994) 91.

-
- [32] C. Rong, X. Qin, *J. Mol. Catal.* 64 (1991) 321.
- [33] P.G. Moses, B. Hinnemann, H. Topsøe, J.K. Nørskov, *J. Catal.* 248 (2007) 188.
- [34] M. Neurock, R.A. van Santen, *J. Am. Chem. Soc.* 116 (1994) 4427.
- [35] R.J. Angelici, *Polyhedron* 16 (1997) 3073.
- [36] R.J. Angelici, *Bull. Soc. Chim. Belg.* 104 (1995) 265.
- [37] P.C.H. Mitchell, D.A. Green, E. Payen, J. Tomkinson, S.F. Parker, *Phys. Chem. Chem. Phys.* 1 (1999) 3357.
- [38] C. Bianchini, J.A. Casares, R. Osman, D.I. Pattison, M. Peruzzini, R.N. Perutz, F. Zanobini, *Organometallics* 16 (1997) 4611.
- [39] L. Dong, S.B. Duckett, K.F. Ohman, W.D. Jones, *J. Am. Chem. Soc.* 114 (1992) 151.
- [40] S. Luo, T.B. Rauchfuss, Z. Gan, *J. Am. Chem. Soc.* 115 (1993) 4943.
- [41] R. Prins, V.H.J. de Beer, G.A. Somorjai, *Catal. Rev.-Sci. Eng.* 31 (1989) 1.
- [42] B.C. Wiegand, C.M. Friend, *Chem. Rev.* 92 (1992) 491.
- [43] D.R. Huntley, D.R. Mullins, M.P. Wingeier, *J. Phys. Chem.* 100 (1996) 19620.
- [44] S.T. Oyama, W. Li, *Top. Catal.* 8 (1999) 75.
- [45] M. Fernández-García, *Catal. Rev. – Sci. Eng.* 44 (2002) 59.
- [46] C.-F. Cheng, D.H. Park, J. Klinowski, *J. Chem. Soc., Faraday Trans.*, 93(1) (1997) 193.
- [47] C.L. Yaws, K.P. Narasimhan, C. Gabbula, *Yaws' Handbook of Antoine Coefficients for Vapor Pressure*, Knovel, 2005.
- [48] K. K. Bando, T. Saito, K. Sato, T. Tanaka, F. Dumeignil, M. Imamura, N. Matsubayashi, H. Shimada, *Top. Catal.* 18 (2002) 59.
- [49] S.T. Oyama, X. Wang, Y.-K. Lee, K. Bando, F. Requejo, *J. Catal.* 210 (2002) 207.

-
- [50] S.T. Oyama, Y.-K. Lee, *J. Catal.* 258 (2008) 393.
- [51] F. W. Lytle, *J. Catal.* 43 (1976) 376.
- [52] F. W. Lytle, P. S. P. Wei, R. B. Gregor, G. H. Via, J. H. Sinfelt, *J. Chem. Phys.* 70 (1979) 4849.
- [53] S. Rundqvist, *Acta Chem. Scand.* 16 (1962) 992.
- [54] Powder Diffraction Data Files, JCPDS International Center for Diffraction Data, Swathmore, PA, 1992.
- [55] C.T. Kresge, M.E. Leonowicz, W.J. Roth, J.C. Vartuli, J.S. Beck, *Nature* 359 (1992) 710.
- [56] S.T. Oyama, Y.-K. Lee, *J. Phys. Chem. B* 109 (2005) 2109.
- [57] K.A. Layman, M.E. Bussell, *J. Phys. Chem. B* 108 (2004) 15791.
- [58] T.L. Tarbuck, K.R. McCrea, J.W. Logan, J.L. Heiser, M.E. Bussell, *J. Phys. Chem. B* 102 (1998) 7845.
- [59] A.A. El-Azhary, R.H. Hilal, *Spectrochim. Acta* 53 (1997) 1365.
- [60] P. Mills, S. Korlann, M.E. Bussell, M.A. Reynolds, M.V. Ovchinnikov, R.J. Angelici, C. Stinner, T. Weber, R. Prins, *J. Phys. Chem. A* 105 (2001) 4418.
- [61] P. Mills, D.C. Phillips, B.P. Woodruff, R. Main, M.E. Bussell, *J. Phys. Chem. B* 104 (2000) 3237.
- [62] W.W.C. Quigley, H.D. Yamamoto, P.A. Aegerter, G.J. Simpson, M.E. Bussell, *Langmuir* 12 (1996) 1500.
- [63] Z. Wu, C. Li, Z. Wei, P. Ying, Q. Xin, *J. Phys. Chem. B* 106 (2002) 979.
- [64] J.A. Rodriguez, J. Dvorak, A.T. Capitano, A.M. Gabelnick, J.L. Gland, *Surf. Sci.* 429 (1999) L462.

-
- [65] N.A. Khan, H.H. Hwu, J.G. Chen, *J. Catal.* 205 (2002) 259.
- [66] Z. Wu, Z. Hao, P. Ying, Z. Wei, C. Li, Q. Xin, *J. Phys. Chem. B* 104 (2000) 12275.
- [67] Z. Wu, C. Li, P. Ying, Z. Wei, Q. Xin, *J. Phys. Chem. B* 105 (2001) 9183.
- [68] M. Trombetta, G. Busca, S. Rossini, V. Piccoli, U. Cornaro, *J. Catal.* 168 (1997) 334.
- [69] T.M. El-Gogary, *Spectrochim. Acta, Part A* 57 (2001) 1405.
- [70] E.J.M. Hensen, H.J.A. Brans, G.M.H.J. Lardinois, V.H.J. de Beer, J.A.R. van Veen, R.A. van Santen, *J. Catal.* 192 (2000) 98.
- [71] P.B. Weisz, C.D. Prater, *Adv. Catal. Relat. Subj.* 6 (1954) 143.

Chapter 5

Conclusions

The diminishing quality of oil feedstocks coupled with increasingly more stringent environmental regulations limiting the content of sulfur in transportation fuels have given rise to a need for improved hydroprocessing technology. A number of major improvements in hydrodesulfurization (HDS) and hydrodenitrogenation (HDN) catalysts and processes have been reported in recent years. A new class of hydroprocessing catalysts, the transition metal phosphides, have emerged as a promising group of high-activity, stable catalysts. The phosphides have physical properties resembling ceramics, so are strong and hard, yet retain electronic and magnetic properties similar to metals. Their crystal structures are based on trigonal prisms, yet they do not form layered structures like the sulfides. They display excellent performance in HDS and HDN, with the most active phosphide, Ni₂P, having activity surpassing that of promoted sulfides on the basis of sites titrated by chemisorption (CO for the phosphides, O₂ for the sulfides). In the HDS of difficult heteroaromatics like 4,6-dimethyldibenzothiophene Ni₂P operates by the hydrogenation pathway, while in the HDN of substituted nitrogen compounds like 2-methylpiperidine it carries out nucleophilic substitution. The active sites for hydrogenation in Ni₂P have a square pyramidal geometry, while those for direct hydrodesulfurization have a tetrahedral geometry. Overall, Ni₂P, is a promising catalyst for deep HDS in the presence of nitrogen and aromatic compounds.

A kinetic study of pyridine hydrodenitrogenation (HDN) was conducted on a 12.2 wt% silica-supported nickel phosphide ($\text{Ni}_2\text{P}/\text{SiO}_2$) catalyst at 423 K and atmospheric pressure. In situ Fourier transform infrared spectroscopy (FTIR) measurements of pyridine adsorbed on Ni_2P revealed the formation of a pyridinium surface intermediate. The concentration of the pyridinium intermediate increased with pyridine partial pressure and decreased in the presence of hydrogen, suggesting that it was a reaction intermediate. However, transient and steady-state kinetic measurements showed that the rate of reaction of the intermediate did not correspond to the overall reaction rate, and it is concluded that the pyridinium intermediate is not directly involved in the HDN reaction of pyridine over Ni_2P . The studies demonstrate that mere observation of an adsorbed surface species at reaction conditions is not sufficient to prove that it is a reaction intermediate.

The hydrodesulfurization (HDS) of thiophene was studied over $\text{Ni}_2\text{P}/\text{MCM-41}$ by in situ Fourier transform infrared (FTIR) spectroscopy and x-ray absorption near edge structure (XANES) measurements at atmospheric pressure and 393-723 K (120 – 450 °C). FTIR showed the presence of adsorbed molecular thiophene principally on the MCM-41 support. In the presence of hydrogen new peaks in the aliphatic C-H stretching region (2953, 2918 and 2876 cm^{-1}) and the CH_2 scissoring region (1464 cm^{-1}) appeared and grew with temperature up to 553 K (280 °C). These were assigned to a tetrahydrothiophene surface intermediate. XANES measurements also showed growth of a signal (8330.9 eV) attributed to Ni-S interactions of the adsorbed tetrahydrothiophene between 353 – 573 K (180-300 °C). Transient XANES measurements showed that the tetrahydrothiophene species responded dynamically at the same rate as the steady-state

rate, indicating that it was an intermediate in the reaction. The results indicate that the HDS of thiophene goes through a hydrogenated intermediate, consistent with the high hydrogenation activity of nickel phosphide.